

# In-structure shock assessment and mitigation of structures

Zhou, Hongyuan

2012

Zhou, H. Y. (2012). In-structure shock assessment and mitigation of structures. Doctoral thesis, Nanyang Technological University, Singapore.

<https://hdl.handle.net/10356/49983>

<https://doi.org/10.32657/10356/49983>



**IN-STRUCTURE SHOCK ASSESSMENT AND  
MITIGATION OF STRUCTURES**

**HONGYUAN ZHOU**

**SCHOOL OF**

**CIVIL AND ENVIRONMENTAL ENGINEERING**

**2012**

# **IN-STRUCTURE SHOCK ASSESSMENT AND MITIGATION OF STRUCTURES**

**HONGYUAN ZHOU**

School of Civil and Environmental Engineering

A thesis submitted to the Nanyang Technological University

in partial fulfillment of the requirement for

the degree of Doctor of Philosophy

**2012**

## **ACKNOWLEDGEMENTS**

I would like to express my sincerest gratitude to my supervisors, Prof. Ma Guowei, Prof. Zhao Zhiye and Mr. Lim Chee Hiong, for their profound vision, research philosophy, invaluable guidance, and encouragement in conducting this research work. I will never forget Prof. Ma's enthusiasm in research. From him, I not only learn how to do research, but also gain ability to deal with real engineering problems. His way of doing things influences me deeply. Prof. Zhao is very nice and kind. He teaches me an ever-holding rule in engineering, even the most beautiful formula is untrustable until it is validated and confirmed by other means: numerical simulation or experiment. From Mr. Lim, I learn invaluable things in life.

I also would like to appreciate the generous help by Prof. Masuhiro Beppu, National Defence Academy, Japan, who carried out the small scale test for me to validate my theoretical prediction. Prof. Yu Tongxi, Hongkong University of Science and Technology, teaches me not only knowledge on impact dynamics and metal foams, but also guided me in research through inspiring discussions.

The research scholarship offered by Nanyang Technological University is gratefully acknowledged.

Finally, I must acknowledge the long-lasting understanding, patience, encouragement and support provided by my wife, Wang Xiaojuan, without her, my life in Singapore would be dull and hard, and the completion of this thesis would not be possible. In my hard time, my father and friends always give me warm and powerful support. I am in memory of my mother.

# TABLE OF CONTENTS

## ACKNOWLEDGEMENTS

TABLE OF CONTENTS .....	i
-------------------------	---

ABSTRACT .....	vi
----------------	----

LIST OF TABLES .....	vii
----------------------	-----

LIST OF FIGURES .....	viii
-----------------------	------

LIST OF SYMBOLS .....	xiii
-----------------------	------

1 INTRODUCTION .....	1
----------------------	---

1.1 Background .....	1
----------------------	---

1.2 Objectives and scope .....	2
--------------------------------	---

1.3 Thesis organization .....	3
-------------------------------	---

2 LITERATURE REVIEW .....	5
---------------------------	---

2.1 Subsurface explosion induced shock load .....	5
---	---

2.2 Response and failure of underground structures .....	6
--	---

2.2.1 Numerical simulation .....	6
----------------------------------	---

2.2.2 Experimental study .....	9
--------------------------------	---

2.2.3 Theoretical analysis .....	10
----------------------------------	----

2.3 In-structure shock of underground structures .....	12
--	----

2.3.1 In-structure shock prediction in major design codes .....	12
---	----

2.3.2	Research on in-structure shock of underground structures .....	16
2.4	In-structure shock mitigation of underground structures .....	17
2.5	Cellular solids and structures .....	18
2.5.1	Compression of cellular solids.....	19
2.5.2	Plateau stress and densification strain.....	20
2.6	Dynamic behaviors of cellular materials.....	21
2.6.1	Different crushing modes.....	21
2.6.2	Material models for dynamic crushing with applications.....	22
2.6.3	Gradient foam .....	27
3	IN-STRUCTURE SHOCK OF UNDERGROUND STRUCTURES: THEORETICAL ASSESSMENT .....	29
3.1	Dynamic soil-structure interaction .....	29
3.2	Factors affecting the dynamic soil-structure interaction .....	35
3.3	Underground explosion induced shock load and beam model for the structure . .....	40
3.3.1	Underground explosion induced shock load.....	40
3.3.2	Euler beam model .....	43
3.4	Response analysis.....	45
3.4.1	Case I: $\xi_n \geq 1$ .....	46
3.4.2	Case II: $\xi_n < 1$ .....	48
3.4.3	Post-blast phase.....	49

3.5	A case study of response analysis using beam model .....	50
3.6	In-structure shock and response spectrum .....	58
3.7	Summary .....	65
4	IN-STRUCTURE SHOCK ASSESSMENT OF UNDERGROUND STRUCTURES WITH CONSIDERATION OF RIGID BODY MOTION .....	67
4.1	Methodology .....	67
4.2	Rigid body motion of the whole structure.....	69
4.3	Structural element response to shock load .....	71
4.3.1	Kirchhoff plate model .....	71
4.3.2	Case I: $\zeta_{mn} \geq 1$ .....	73
4.3.3	Case II: $\zeta_{mn} < 1$ .....	75
4.3.4	Gross response in the blast duration .....	76
4.4	A case study and discussions .....	79
4.5	Summary .....	87
5	DOUBLE-LAYER FLOOR TO MITIGATE IN-STRUCTURE SHOCK OF UNDERGROUND STRUCTURES: A CONCEPTUAL DESIGN .....	88
5.1	Introduction .....	88
5.2	Rigid body motion of the whole structure: post-blast phase.....	88
5.3	Vibration of the isolation slab .....	89
5.3.1	Phase I: loading phase.....	92
5.3.2	Phase II: post-loading phase .....	93

5.3.3	Shock of equipment attached to the isolation slab.....	95
5.4	A case study and discussions .....	96
5.5	Summary .....	106
6	IN-STRUCTURE SHOCK OF UNDERGROUND STRUCTURES: EXPERIMENTAL INVESTIGATION .....	108
6.1	Introduction .....	108
6.2	Structural response prediction under pulse of non-zero rise time.....	110
6.3	Experiment set-up .....	110
6.4	Determination of the standoff distance and plate dimensions.....	114
6.5	Results and discussion.....	116
6.6	Summary .....	126
6.7	Acknowledgment .....	127
7	METAL FOAM CLADDING SUBJECTED TO A LOCALIZED BLAST: A THEORETICAL APPROACH.....	128
7.1	Introduction .....	128
7.2	Determination of the bulge.....	130
7.2.1	Deformation profile of the face sheet .....	130
7.2.2	Determination of the bulge extent.....	133
7.2.3	Determination of the bulge depth .....	136
7.3	Discussions with a case study .....	143
7.4	Analysis of density gradient metal foam for blast mitigation .....	153



7.4.1	Formulation of continuous metal foam subjected to a blast load .....	154
7.4.2	Case study and discussions of gradient foam under high velocity crushing .....	162
7.5	Summary .....	173
8	CONCLUSIONS AND FUTURE WORK.....	174
8.1	Conclusions .....	174
8.2	Future work .....	177
	REFERENCES .....	179
	APPENDIX A: THE RESPONSE DERIVATION OF A STRUCTURAL MEMBER SUBJECTED TO A SOIL-TRANSMITTED BLAST WITH NON-ZERO RISE TIME .....	189
A.1	Introduction .....	189
A.2	Phase I: $0 < t < \lambda T_d$ .....	190
A.3	Phase II: $\lambda T_d < t < T_d$ .....	194
	APPENDIX B: PUBLICATIONS .....	198
	Journal papers .....	198
	Proceedings papers.....	199

## ABSTRACT

This thesis deals with soil-structure interaction effect and structural response analysis, in-structure shock assessment, and shock wave mitigation when a structure is subjected to a blast load.

Dynamic media-structure interaction is analytically discussed in the background of an underground structure subjected to a soil-transmitted dynamic load, in which an interfacial damping is incorporated to represent the dynamic soil-structure interaction. The effects of the interaction are analyzed and the aspects affecting the interaction are discussed. With this soil-structure interaction, in-structure shock of a typical underground structure subjected to a soil-transmitted blast load induced by a subsurface detonation is analyzed with a simplified beam model and a rigid-body-motion included plate model, respectively. With acceleration time history of the derived structural member as excitation, shock response spectra are established to assess the in-structure shock level of the equipment attached to the buried structure. To mitigate the in-structure shock, a new design of underground structures is proposed by adding an isolation slab inside the structure. The excitation mechanism for the equipment within the structure is altered and the vertical shock level is effectively reduced. In addition, in-structure shock induced by a soil blast with non-zero rise time is also analyzed. A small scale test is designed and conducted to validate the prediction. Tests results indicate that the predictions are favorably comparable with the experiment.

When subjected to a close range spherical airburst, the response of a blast mitigation cladding with metal foam core is determined by energy method. Shock theory and rigid-perfectly-plastic-locking model is adopted to obtain the response of metal foam under high velocity crushing. This prediction has practical significance since it delineates the situation of a cladding subjected to a close range detonation event with realistic boundary. Further, density gradient metal foam as core of a blast mitigation cladding is theoretically investigated with shock theory and rigid-perfectly-plastic-locking model.

## LIST OF TABLES

	<b>Page</b>
Table 3.1      Properties of typical soils in Singapore	52
Table 3.2      Interfacial damping ratios of structure in typical soil	53
Table 3.3      Equipment shock resistance	64
Table 7.1      Total energy input per unit area: the gradient foam ( $\beta=0.8$ ) and homogeneous foam ( $L=7$ cm; $T_d=0.5$ ms; $\rho/\rho_s=12.33\%$ )	171

## LIST OF FIGURES

		<b>Page</b>
Fig. 1.1	Underground structure subjected to blast loads	2
Fig. 2.1	A rectangular underground structure subjected to a subsurface detonation	13
Fig. 2.2	Reduction factor for in-structure acceleration and velocity	14
Fig. 2.3	Open-cell and close-cell metal foams	18
Fig. 2.4	Shock fronts under various impact velocities (Lopatnikov et al. 2003)	23
Fig. 3.1	A structure in soil subjected to a soil-transmitted dynamic load and its analytical model	31
Fig. 3.2	Interfacial damping ratios of a system consisting of certain concrete plate and surrounding wet sandy clay	36
Fig. 3.3	The effect of $a/h$ on the interfacial damping ratio	37
Fig. 3.4	The relationship: (a) the maximum deformation (b) the maximum velocity and (c) the maximum acceleration of the plate center versus the soil-to-structure acoustic impedance ratio, $h$ is the plate thickness and $T_d$ is the blast duration	38
Fig. 3.5	Underground structure subjected to blast load and simplified analysis model	44
Fig. 3.6	Ground shocks in three soils (1: dry sand; 2, Kallang soil; 3: Bukit Timah soil)	51

Fig. 3.7	Time histories of displacement, velocity and acceleration at mid-span of the structural member	54
Fig. 3.8	Mid-span response comparison under different blast durations, Kallang soil	56
Fig. 3.9	Maximum displacement, velocity and acceleration at mid-span of the structural member	57
Fig. 3.10	Schematic illustration of shock response spectra	60
Fig. 3.11	Shock response spectra of equipment under in-structure shock with Kallang soil	61
Fig. 3.12	Influence of various factors on the shock response spectra	62
Fig. 4.1	Free body diagram of the underground structure (assumed rigid)	70
Fig. 4.2	Underground structure subjected to subsurface detonations	80
Fig. 4.3	Time histories of upper and lower bounds of (a) deformation; (b) gross velocity; and (c) gross acceleration at the structural element center, Kallang soil	81
Fig. 4.4	Upper and lower bounds of (a) maximum deformation; (b) gross velocity; and (c) gross acceleration at the structural element center versus scaled distance, Kallang soil	82
Fig. 4.5	Upper and lower bounds of (a) maximum deformation; (b) gross velocity; and (c) gross acceleration at the structural element center versus scaled distance, Kallang soil (dimension in movement direction = 300 m, for validation of the solution)	85
Fig. 4.6	Maximum (a) deformation; (b) gross velocity; and (c) gross acceleration of structural element center versus scaled distance: different soils	86
Fig. 4.7	Shock response spectra of devices subjected to in-structure	87

shock, Kallang soil

Fig. 5.1	Illustration of the newly designed underground structure and the equivalent system of the isolation slab with attached equipment	90
Fig. 5.2	The rigid body motion responses of the whole structure	98
Fig. 5.3	Rigid body motion velocities: with and without soil-structure separation	99
Fig. 5.4	The relative deflection and absolute acceleration time histories at the isolation slab center	100
Fig. 5.5	The maximum acceleration of the isolation slab center with respect to slab natural frequency	101
Fig. 5.6	Comparison of shock response spectra at isolation slab center and edges: dry sand	102
Fig. 5.7	Comparison of shock response spectra for equipment near isolation slab edges: structure in different soils	103
Fig. 5.8	Shock response spectra comparison: structure with and without isolation slab in three typical soils	104
Fig. 5.9	Illustration of the installation of the isolation slab (not to dimension, for illustration purpose only)	107
Fig. 6.1	The idealized profile of a soil-transmitted blast	109
Fig. 6.2	The designed test set-up (not to scale)	112
Fig. 6.3	The small scale test set-up	113
Fig. 6.4	Predicted response time histories at the mid-span	117
Fig. 6.5	Comparison of the predicted acceleration time histories with test results	119
Fig. 6.6	Comparison of the predicted and tested strain time history at the	122

	plate center	
Fig. 6.7	Comparison of the structural response with and without pulse rise time	123
Fig. 6.8	Response spectra comparison of soil blast with and without blast rise time	126
Fig. 7.1	Determination of the bulge extent	131
Fig. 7.2	Pre-defined deformation profiles of thin plates	132
Fig. 7.3	Energy dissipation by the foam dynamic enhancement with respect to time (1-D crushing is assumed)	139
Fig. 7.4	Relation between the specific energy of aluminum foam and its relative density	144
Fig. 7.5	Relation between the non-dimensional bugle extent and peak load	146
Fig. 7.6	Relation between the bugle depth and: (a) peak load; (b) blast duration	148
Fig. 7.7	Relation between the bugle depth and face sheet yield strength	149
Fig. 7.8	Relation between the bugle depth and: (a) face sheet density; (b) face sheet thickness	150
Fig. 7.9	Relation between the bugle depth and foam relative density	151
Fig. 7.10	Relation between $\beta$ and the initial peak velocity	152
Fig. 7.11	Relation between the bugle depth and $\beta$	152
Fig. 7.12	Foam core with density gradient: (a) high relative density, high plateau stress, small densification strain; (b) moderate relative	155

	density, moderate plateau stress, moderate densification strain; (c) low relative density, low plateau stress, large densification strain	
Fig. 7.13	Idealization of the stress-strain relation of metal foam (relative density less than 0.3)	157
Fig. 7.14	A blast mitigation cladding with metal foam core and a face sheet	159
Fig. 7.15	Free body diagram of the system consisting of the face sheet and densified foam (within the blast duration)	161
Fig. 7.16	Time histories of (a) displacement; (b) velocity of the shock front	164
Fig. 7.17	Time histories of (a) displacement; (b) velocity of the system consisting of the face sheet and densified foam	165
Fig. 7.18	Time histories of energy absorption ( $E_{\text{ref}}$ is the total energy absorption when the homogeneous foam core is fully densified quasi-statically)	166
Fig. 7.19	Time histories of energy absorption rate ( $E_{\text{ref}}$ is the total energy absorption when the homogeneous foam core is fully densified quasi-statically)	168
Fig. 7.20	The relationships between (a) total energy input per unit area; (b) total energy input reduction per unit area and $\beta$ ( $E_0$ is the energy input per unit area for $\beta=0$ )	169
Fig. 7.21	The relationship between total energy input reduction per unit area and peak load ( $E_h$ is the energy input per unit area of the corresponding homogeneous foam for each load)	171



## LIST OF SYMBOLS

### Symbols used in Chapter 3

$A$	cross-sectional area of the beam
$c_s$	acoustic velocity of the surrounding soil
$D$	flexural rigidity of plate
$E$	Young's modulus
$EI$	flexural rigidity of the beam
$f$	coupling factor of the explosion energy to soil
$h$	thickness of the plate
$l$	length of the beam
$r$	attenuation coefficient of blast wave in soil
$P_0$	free-field peak pressure
$q_n(t)$	$n$ th mode general coordinate of the beam
$R$	distance from center of explosion to structure
$t$	time
$t_a$	travel time of shock wave from detonation to structure

$T_d$	blast time duration
$t_1$	start time of free vibration of the beam
$w$	displacement of the beam or plate
$W$	TNT equivalent charge weight
$W_n(x)$	$n$ th mode shape of the beam
$W_{mn}(x,y)$	$m,n$ th mode shape of the plate
$x$	coordinate along the beam
$\alpha$	reduction factor
$\beta$	a factor equal to 160 in imperial unit system
$\sigma_f(t)$	free-field pressure time history
$\sigma_{sy}$	soil yield strength
$\rho, \rho_s$	mass density of the structure and soil
$\omega$	natural frequency
$\zeta$	interfacial damping ratio
$\nu$	Poisson's ratio of the structure material
$\eta_{mn}$	$m,n$ th generalized coordinate of the plate

## Symbols used in Chapter 4

$A$	area of the structural element closest to the subsurface detonation
$a, b$	in-plane dimension
$c_s$	acoustic velocity of the surrounding soil
$D$	flexural rigidity of the structural element
$E$	Young's modulus of the structure material
$f$	coupling factor of the explosion energy to soil
$h$	thickness of the structural element
$h_e$	effective thickness of the whole structure
$M$	mass of the whole structure
$P_0$	free-field peak pressure
$R$	distance from center of explosion to structure
$r$	attenuation coefficient of blast wave in soil
$T_d$	blast duration
$t$	time starting at the arrival of the blast wave
$t_a$	travel time of shock wave from detonation to structure
$U(t)$	rigid body motion displacement of the whole structure

$W$	TNT equivalent charge weight
$w(x,y,t)$	gross displacement time history of the structural element
$W_{mn}(x,y)$	$m, nth$ mode shape of the structure element
$w_{mn}(x,y,t)$	$m, nth$ mode contribution to pure deflection of the structural element
$x, y$	in-plane coordinate with origin at a corner
$\alpha$	reduction factor
$\beta$	a factor equal to 160 in imperial unit system
$\eta_{mn}(t)$	$m, nth$ mode general coordinate
$\sigma_f$	free-field pressure time history
$\rho, \rho_s$	mass density of the structure and soil
$\zeta_{mn}$	$m, nth$ mode interfacial damping ratio
$\nu$	Poisson's ratio of the structure material
$\tau_0$	characteristic response time of the whole structure
$\omega_{mn}$	$m, nth$ mode natural frequency of the structural element

## **Symbols used in Chapter 5**

$A$	area of the blast load on a structural member
$c_s$	acoustic velocity of soil

$E$	Young's modulus of concrete
$f$	coupling factor of the explosion energy to soil
$h$	thickness of floor and walls of the structure
$h_s$	thickness of the isolation slab
$L_1, L_2, L_3$	length, width and height of the structure
$k_s$	stiffness of the isolation slab
$K_L$	load factor
$K_M$	mass factor
$n$	attenuation coefficient of stress wave in soil
$m_s$	mass of the isolation slab
$M$	mass of the whole underground structure
$P_0$	free-field peak pressure
$R$	distance from explosion center to the structure
$t$	time starting at the arrival of the blast load
$t_1$	time starting after the blast load
$T_d$	blast duration
$u(t)$	relative displacement between the isolation slab and whole structure
$U(t)$	rigid body motion displacement of the whole structure
$W$	TNT equivalent charge weight
$x_s$	absolute displacement of the isolation slab

$\alpha$	reduction factor
$\beta$	a factor equal to 160 in imperial unit system
$\rho$	mass density of concrete
$\rho_s$	mass density of soil
$\tau_0$	characteristic response time
$\omega$	circular natural frequency of equivalent SDOF system representing isolation slab
$\varsigma$	damping ratio of equivalent SDOF system representing isolation slab
$\nu$	Poisson's ratio of the structure material

### **Symbols used in Chapter 6**

$M_{\max}$	maximum bending moment
$\lambda$	dimensionless number ranging from 0 to 1
$\sigma_m$	maximum stress in bending
$\sigma_y$	yield strength

Other symbols used in this chapter are the same as those in chapter 3.

### **Symbols used in Chapter 7**

$b, c$	characteristic size of the round loading area and the bulge
$E$	specific energy (energy per unit area) absorbed by foam core
$E_f, E_{\text{str}}$	total energy dissipated by the foam/ face sheet during crushing

$E_k$	kinetic energy of the face sheet
$h_b$	thickness of the face sheet
$l$	shock front location
$L$	thickness of the foam core
$\Delta m$	mass per unit area of the densified foam
$p_c$	peak load on face sheet
$P_0$	peak load on the face sheet
$P(t)$	load time history on the face sheet
$r$	coordinate starting from the point nearest to the detonation in face sheet
$R$	standoff distance between the explosion and face sheet
$T_d$	blast duration
$W_0$	depth of the bulge
$W_s$	energy absorption per unit volume quasi-statically
$u$	displacement of the face sheet
$v$	crushing velocity
$V_0$	initial velocity at the bulge center

$x$	coordinate from the initial location of the interface between the face sheet and foam core
$\beta$	gradient of foam density/ coefficient for estimating the foam dynamic enhancement
$\rho_0, \rho_L$	foam density at the impact end and stationary end
$\rho_b$	density of the face sheet material
$\rho_s$	density of the base material from which the foam is made
$\rho^*$	density of the crushed foam
$\sigma_D$	densification stress of the foam
$\sigma_{Dd}$	average dynamic enhancement
$\sigma_{pl}$	plateau stress of the foam
$\sigma_{str}$	resistance contribution from face sheet stretching
$\sigma_{yd}, \sigma_{ys}$	dynamic and quasi-static yield strength of face sheet
$\sigma_y$	yield strength of the base material from which the foam is made
$\varepsilon_D$	densification strain of the foam
$\lambda, C_1$	material constants of the foam
$\eta$	extent of the bulge



# 1 INTRODUCTION

## 1.1 Background

When an engineering structure is subjected to a dynamic load, generally two situations are of particular interest. One frequently encountered scenario is that the structure experiences damage if the loading intensity exceeds certain value. The other situation is under a specific loading intensity, the structure itself is slightly damaged or even not damaged, but the sub-structure attached is damaged due to the severe vibration or shock. This severe vibration is termed in-structure shock. The former situation is related to the limit state analysis and was intensively studied. For the latter issue, on the contrary, sufficient attention has not been paid. With the development of technology, equipment and devices are increasingly vulnerable to strong vibration due to their increasing complexity and sensitivity.

Underground protective structures are built to protect personnel and equipment from attacks, which are generally monolithic boxes made of reinforced concrete walls and slabs, indicated in Fig. 1.1. The response of underground structures subjected to dynamic loading has long been a topic of interest in protective engineering. When an underground detonation occurs, a shock wave is generated which propagates in all directions in soil and attenuates rapidly with the increase of the distance from the charge center. At a certain standoff distance, the underground structure itself may survive the blast, but the instruments and equipment contained within the structure may sustain damage due to the in-structure shock induced by the soil-transmitted load. Indeed, some of the equipment is delicate and vulnerable to such kind of shock load. Therefore it is necessary to evaluate in-structure shock when designing an underground structure.

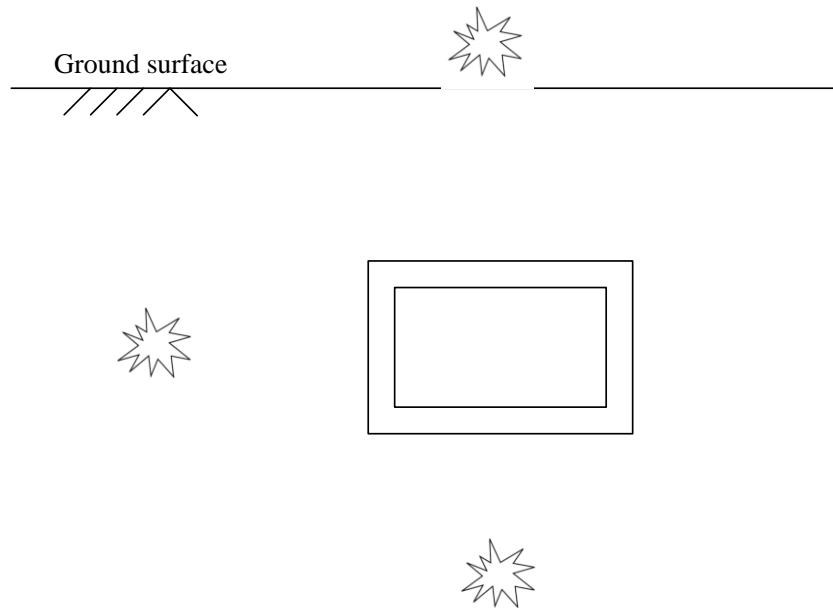


Fig. 1.1 Underground structure subjected to blast loads

Under compression, a cellular solid undergoes large strain with an almost constant stress level, which makes it a perfect energy absorber. When a structure is subjected to an air blast, the cellular solids may be used as core of a sacrificial cladding. A considerable amount of energy can be absorbed by the cellular material; in addition, the load transmitted to the protected structure is kept below certain value.

## 1.2 Objectives and scope

The objectives of the study are:

- to evaluate the in-structure shock of an underground structure subjected to a soil-transmitted blast load;
- to propose a method to mitigate the in-structure shock of underground structures subjected to soil-transmitted blast load;
- to experimentally validate the theoretical in-structure shock prediction;
- to investigate the possible application of metal foam for blast mitigation.

The in-structure shock of underground structures subjected to soil-transmitted blast loads will be theoretically predicted by a simplified beam model first, where dynamic soil-structure interaction is incorporated. Further, the in-structure shock prediction will be refined by a plate model with rigid body motion taken into consideration. A new design will be proposed to mitigate vertical in-structure shock level within an underground structure by adding an isolation slab near the floor. To validate the theoretical prediction in the study, a small scale test will be designed and performed. Lastly, possible applications of metal foam cladding for blast mitigation will be investigated.

### **1.3 Thesis organization**

The thesis consists of eight chapters. The first chapter briefs the background, objectives and scope of the study and thesis organization.

The second chapter reviews the behavior of underground structures subjected to dynamic loads, in the aspects of strength and serviceability. The in-structure shock prediction in major designed codes, as well as relevant research work, is reviewed. Further, the research on metal foam properties, especially the behavior under high velocity crushing and the application in blast mitigation, is covered.

In Chapter 3, the dynamic soil-structure interaction is briefly introduced and the aspects influencing the interaction are discussed. Subsequently, with soil-structure interaction incorporated, the in-structure shock of underground structures is investigated using an idealized beam model.

Chapter 4 refines the in-structure shock assessment by incorporating the rigid body motion of the whole structure.

Chapter 5 proposes a simple and economical design to alleviate vertical in-structure shock level within an underground structure subjected to a subsurface detonation.

In Chapter 6, the in-structure shock of underground structures is examined with the rise time of soil-transmitted blast load taken into consideration. To validate the analytical prediction, a small scale test is designed and conducted.

Chapter 7 examines the possible application of metal foam for blast mitigation and the behavior of gradient foam subjected to a blast load is studied.

Chapter 8 concludes the PhD thesis and outlines the future work.

In overall, Chapter 3 through Chapter 6 focus on “In-structure shock assessment and mitigation of underground structures”. Chapter 3 first studies the soil-structure interaction and establishes the methodology to assess in-structure shock of underground structures with a relatively simple modified beam model. However, the modified beam model is only applicable to relatively narrow structural members (or structural members supported by two opposite edges and other two edges free). To make the proposed in-structure shock assessment model more useful for rectangular elements with arbitrary dimension ratios, a plate model is adopted in Chapter 4 to predict the shock with similar methodology; in addition, to make the prediction more accurate, rigid body motion is also incorporated. Besides assessing in-structure shock, the mitigation of such shocks are also of particular importance. Therefore in addition to the traditional shock alleviation methods for underground structures, Chapter 5 proposes a new structural design, in which an isolation slab is attached slightly above the floor to mitigate the vertical in-structure shock. With all these chapters as theoretical investigations, a small scaled test is conducted in Chapter 6 to examine and validate whether the in-structure shock predictions for underground structures are reasonable.

Chapter 7 is another topic of the thesis, more or less independent. First, the bugle extent and depth of a metal foam cladding subjected to a relatively close air-blast is studied with energy method. Then crushing of a cladding with density gradient foam core subjected to an air-blast is investigated. Both work in this chapter is theoretical.

## **2 LITERATURE REVIEW**

### **2.1 Subsurface explosion induced shock load**

A subsurface detonation generates a soil-transmitted blast load, whose intensity is determined by several aspects including the soil properties, charge weight of the explosive, standoff distance from detonation as well as the coupling between the explosion energy and the soil. Influences of these parameters to the ground shock are well documented (TM-5-855-1 1986; ASCE manual-42 1985). For ground shock prediction, several methods (e.g. Westine 1978; TM-5-855-1 1986; Henrych 1979) are frequently applied.

Recently, Lu (2005) summarized the effect of the various input variables on the ground shock parameters and established a suitable dataset, where the data were obtained from a given program, to represent the nature of the phenomenon. Artificial neural network (ANN) technique was employed to identify the system pattern and serve as a function for predicting the ground shock. It was proved that the usage of ANN was successful since the trained neural network can predict the unseen test data consistently and accurately.

However, the ground shock prediction in TM-5-855-1, based on experimental data, is not dimensionally consistent. Leong *et al.* (2007) re-examined the formulas on peak stresses of ground shock induced by subsurface detonations and introduced dimensionless parameters into the formulation, which provides a better understanding of the relationship between the peak pressure and scaled distance.

## **2.2 Response and failure of underground structures**

To study the underground structure responses to subsurface explosions by experiment is costly. In addition, it is almost impossible to carry out parametric studies to identify the critical parameters by experiments. Therefore researchers have increasingly resorted to numerical simulations for the detailed investigation of the underground structures under dynamic loads.

### **2.2.1 Numerical simulation**

Numerical method is widely used to analyze problems with complex geometrical configuration and nonlinear material properties. Finite element method (FEM), finite difference method (FDM), and smoothed particle hydrodynamics (SPH) are the most popular and classic schemes for explosion simulation. In addition, commercial software such as LS-DYNA, ABAQUS, ADINA and AUTODYN, developed in recent decades, enable scientists and engineers to tackle the problem in a convenient way.

The reason why dynamic analysis of underground structures appears difficult is the soil-structure interaction is complex. Stevens and Krauthammer (1987) combined FDM and FEM to analyze the soil-structure interaction. Wave propagation in continuous media (soil) with nonlinear constitutive properties was modeled with FDM while the buried structure was modeled with FEM. The best feature of FDM and FEM were employed to their corresponding parts; material and geometrical nonlinearities were also included. Chen and Krauthammer (1989) employed a similar combined approach of FDM and FEM to study the soil-structure interaction of fully buried, partially buried and above-ground structures. The interface condition was implemented into ADINA to carry out the calculations. Stevens and Krauthammer (1991), Stevens *et al.* (1991) used the similar method to study the buried RC arch responses under blast load. It is found that the combined recipe is efficient and economic.

Wright and Smilowitz (1986) established an uncoupling approximation for the dynamic analysis of structures embedded in hysteretic media. The wave propagation was extended to nonlinear media and one-dimensional soil-structure interaction was analyzed using FDM.

Vardoulakis et al. (1987) evaluated the vibration level in underground mined space using boundary element method (BEM). The displacements, velocities and accelerations at exposed free surfaces subjected to ground surface dynamic disturbance were obtained.

Krauthammer and Chen (1986), Chen and Krauthammer (1992) evaluated the dynamic response of rectangular cylindrical reinforced concrete structures (lifelines) subjected to earthquake. Over the entire domain FEM was employed while the substructure and soil-structure interaction was taken into consideration.

Stamos and Beskos (1995) analyzed the dynamic behavior of large 3-D underground structure with BEM. This method is used to model both structure and soil, which are assumed to behave as linear elastic and visco-elastic in the soil-structure interaction, respectively. The structural behavior under several dynamic loads, including transient and harmonic load, were discussed.

Baylot (2000) analyzed effects of soil flow changes for a high explosive detonation very close to a buried structure, in which FEM was employed. The analysis concluded that if the scaled distance is very small, the soil flow near the structure changes significantly due to structure motion and neglecting these changes in flow causes under-prediction of load and structural response.

With the development of the computational method, new techniques were incorporated to achieve greater accuracy. Wang *et al.* (2004) combined smooth particle hydrodynamics (SPH) method and traditional FEM to study structural response subjected to subsurface blasts. Fully coupled numerical method is presented, in which the SPH was employed to model the large deformation of the near-field (to the

detonation) media while for the intermediate and far field, FEM was utilized. In addition, a three-phase soil model was incorporated into the model. Lu and Wang (2004), Lu *et al.* (2005) employed the same method to conduct a comparative study of this problem using 2-D and 3-D model. Results showed that a 2-D model can give reasonable prediction in blast load on structure, crater size and critical response in the structural member nearest to the explosion. However, result differences between 2-D and 3-D models are remarkable in other parts of structure.

Morris *et al.* (2004) simulated underground structures subjected to dynamic loading and investigated the stability of them in response to explosion-induced strong ground motion using distinct element method (DEM) and obtained preliminary results from a parameter study. Both continuous medium soil and discontinuous medium rock, were incorporated in the model.

Park *et al.* (2005) combined BEM with FEM to investigate the dynamic behavior of underground structures in multi-layered soil. The buried structure and its adjacent soil were modeled with FEM while the far field domain was modeled with BEM. The transmission and reflection of waves at each layer interface were considered.

In major design codes, the prediction of ground shock induced by underground explosion is based on peak particle velocity. In fact, besides this parameter, principal frequency, which rarely discussed in literature, is also important, especially for the structure on ground surface. Wu and Hao (2005) established a numerical model to simulate stress wave at a granite site by explosion in an underground chamber. Attenuation was discussed both on ground surface and in free field.

Wang *et al.* (2006a, b) employed the Johnson-Holmquist-Concrete model, an elasto-plastic damage model, to investigate the effects of artificial cavities on the attenuation of air-blast waves in concrete defense layer buried in soil. Rectangular and circular cavities were discussed separately and the effects of multiple cavities on attenuation of air-blast waves were investigated. Moreover, attenuation effect of wave intensity through filling expanded polystyrene geo-foam into cavities was investigated.



Yankelevsky *et al.* (2008) investigated explosion characteristics of a cylindrical explosive buried in soil close to a rigid obstacle using Lagrange approach and modified variational-difference method. The soil was modeled as elasto-plastic medium while pressure distribution along the rigid obstacle was studied with soil-structure interaction.

A distinct advantage of numerical methods is that the comprehensive models can be established readily to represent the real detonation and response situations. However, they can be very computationally intensive; In addition, relevant critical parameters are difficult to determine. Further, verification and validation of the numerical models against analytical or experimental works are pre-requests.

### **2.2.2 Experimental study**

Experimental results are considered to be most reliable and can be applied to verify analytical and numerical models. However, it is expensive, labor-intensive and time-consuming. In addition, it is difficult, if not impossible, to conduct parametric studies using prototype model tests due to the cost issues. Alternatively, small-scaled model tests offer a much more cost-effective and faster way, although dimensional analysis and some assumptions are required.

Some small-scale field explosion tests were done by Anand (2002) in Singapore soils. Reflected pressures and accelerations are recorded for reinforced concrete box and aluminum structure in different standoff distances. The test results can be used to determine the seismic velocity and attenuation coefficient of the soil.

Kobiela and Krauthammer (2004) studied transient soil pressures acting on a protective cylindrical structure (silo) without cover, caused by underground explosions. The measured pressures depended on the charge mass, burial depth and standoff distance. It is found that the maximum value of normal pressure at a large standoff distance from the explosion did not occur on the front surface, but on the sides of the

structure; the greatest value of the tangential pressure caused by shock wave did not appear on the front surface, but at the rear of the structure.

Talesnick *et al.* (2008) carried an experiment aimed at measuring the soil contact pressures which develop on a buried structure as it interacts with the surrounding soil. The study was based on measurements on model structures tested in a pressure chamber filled with fine sand. The influence of roof stiffness on the pressure depends on the stress history.

### **2.2.3 Theoretical analysis**

Analytical methods, which are abstracted from physical prototypes, provide reasonable approaches for real situation, especially for the cases with relatively simple geometries and loading conditions. In fact, all design codes, are based on analytical, semi-analytical and empirical-analytical method (e.g. ASCE manual-42 1985; TM-5-855-1 1986). In addition, much meaningful research contribution has been achieved analytically.

Wong and Weidlinger (1983) reviewed the design codes of underground structure and found that all the considerations regarding soil-structure interaction did not consider the effect of load change due to the structural response. They coupled the load with structural response to achieve higher accuracy and some practical points on underground structure design were discussed. Weidlinger and Hinman (1988) used this coupled approach to analyze underground structures subjected to subsurface explosion. Weidlinger and Hinman (1991) also investigated the effects of cavitation in the process of a stress wave propagating in soil diffracted by an embedded structure. Complicated nonlinearities and discontinuities were found in the system response.

Different from deterministic sense of dynamic response of underground structure subjected to blast loads, Wang and Tan (1995) established stochastic techniques for analyzing shallow-buried reinforced concrete box-typed structures. A stochastic SDOF

model was employed and random variables, including damping, were incorporated into the structural resistance functions which delineate the effect of flexure, shear and in-plane thrust with fragility expressed as a function of the peak load. In addition, a Monte Carlo simulation was performed to obtain statistical results to compare with theoretical prediction.

Chen and Chen (1996) examined the dynamic response of shallow buried flexible plates subjected to impact loading. A circular flexible plate buried in sand, under an impact from surface of the sand, is modeled with an idealized single-degree-of-freedom (SDOF) system. In addition, an experiment of similar configuration was conducted with impact load generated from a falling ball.

Dancygier and Karinski (1999) studied the effect of soil shear resistance on the buried structure response under dynamic loading. Wave propagation effect and soil arching effect were combined to represent a comprehensive soil-structure interaction. Further, a buried circular plate subjected to surface dynamic load was analyzed through an SDOF model. It is found that for short duration blast loads, wave propagation dominates; but for long duration loads, soil shear resistance, which affects soil arching, become important and must be considered. Dancygier and Karinski (1999) also investigated the dynamic response of a buried structure under steady-state vibration at the ground surface, in which both wave propagation and soil arching effects were incorporated. It is found that there exists a range of excitation loading period which significantly increases the deflection of the structure when the natural frequency of the repetitive load is close to one of the natural frequencies of the system consisting of structure and surrounding soil.

Huo et al. (2006) analyzed the deep rectangular structures subjected to far-field shear stresses using complex variable theory and conformal mapping. The deformation imposed on an underground structure was simplified to a pseudo-static one. It is found that the deformations depend on relative stiffness between structure and surrounding soil as well as the structure shape.

## **2.3 In-structure shock of underground structures**

In the preceding section, strength aspect of underground structures under dynamic loads is reviewed. On no account can we ignore the significance of the strength and failure-prevention of underground structures under dynamic loads. Nevertheless, the safety of the personnel and the serviceability of the inside equipment are equally important. Failure in either aspect will completely prevent the whole structure from performing its designed tasks. Therefore, it is necessary to discuss the serviceability of such structures in terms of in-structure shock.

### **2.3.1 In-structure shock prediction in major design codes**

A major concern in designing a protective structure is to prevent structural failure. However, the in-structure shock analysis is equally important. For long-duration motions of underground structures induced by nuclear explosions, the in-structure shock is well documented (ASCE manual-42 1985) since the soil motion is relatively uniform when compared to typical underground structure dimensions. However, the prediction of in-structure shock environment for short-duration ground shocks, such as those generated by conventional weapons, remains to be understood.

The *Fundamentals of protective design for conventional weapons* (TM-5-855-1) and the *Structures to resist the effects of accidental explosions* (TM-5-1300) are two major design codes evaluating the shock level within an underground structure. For a typical box-typed underground structure, the in-structure shock is predicted by TM-5-855-1.

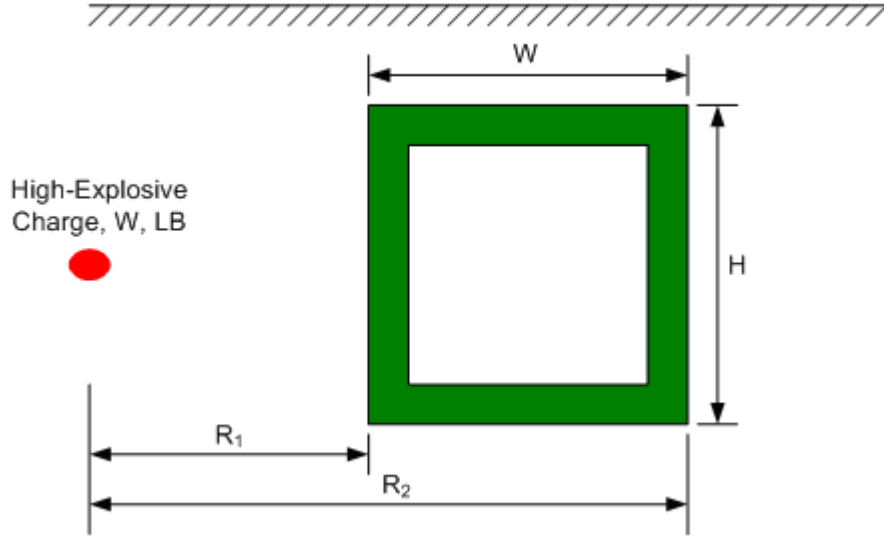


Fig. 2.1 A rectangular underground structure subjected to a subsurface detonation

For a typical box-typed structure subjected to a subsurface detonation, as indicated in Fig. 2.1, the in-structure shock is evaluated as follows:

First, ignore the underground structure and only consider the free field motion in the domain the structure occupies. The displacement, velocity and acceleration of the structure are obtained by integrating the free field values of the corresponding parameters over the span:

$$A_{avg} \times W^{\frac{1}{3}} = \frac{50 f_c c W^{\frac{n+1}{3}} (R_1^{-n} - R_2^{-n})}{n(R_2 - R_1)} \quad (2.1)$$

$$V_{avg} = \frac{160 f_c W^{\frac{n}{3}} (R_1^{-n+1} - R_2^{-n+1})}{(n-1)(R_2 - R_1)} \quad (2.2)$$

$$\frac{d_{avg}}{W^{\frac{1}{3}}} = \frac{500 f_c W^{\frac{n-1}{3}} (R_1^{-n+2} - R_2^{-n+2})}{c(n-2)(R_2 - R_1)} \quad (2.3)$$

where

$A_{avg}$  = average free-field acceleration across the structure, g

$V_{avg}$  = average free-field velocity across the structure, fps

$d_{avg}$  = average free-field displacement across the structure, ft

$W$  = TNT equivalent, lb

$c$  = seismic velocity, fps

$f_c$  = coupling factor

$n$  = attenuation coefficient

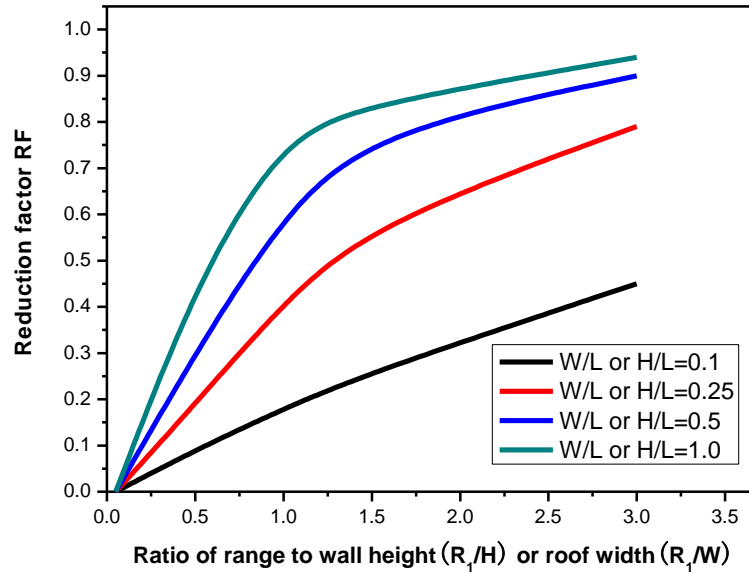


Fig. 2.2 Reduction factor for in-structure acceleration and velocity ( $L$  is the standoff distance between the charge center and the structure)

Among these responses, the free field acceleration is of the greatest concern since it is the excitation to the inside attached equipment.

Second, according to the test data in some soils, the acceleration in Eq. (2.1) is over-predicted. To modify, a reduction factor, defined as the ratio of the equivalent uniformly distributed load to the maximum pressure in the actual load distribution, is multiplied to the prediction in Eq. (2.1). For a typical box-typed buried structure subjected to a spherical subsurface explosion, the reduction factor is given in TM-5-855-1 in terms of the standoff distance and structural dimensions, shown in Fig. 2.2.

The peak structural responses obtained then are used to construct approximate shock response spectra, which predict the maximum responses of the devices attached to the structure. A specific device with support is idealized as a lump-mass SDOF system, which is represented by the corresponding natural frequency, or circular natural frequency, calculated from the specific mass and stiffness. The relationship between the maximum relative displacement  $D$ , the maximum pseudo-velocity  $V$ , and the maximum absolute-acceleration  $A$  of the underground structure is approximately:

$$\frac{A}{\omega_n} = V = \omega_n D \quad (2.4)$$

where  $\omega_n$  is the natural circular frequency of the SDOF system consisting of certain device and support. Further, the values of  $D$ ,  $V$  and  $A$  is multiplied by amplification factors of 1.2, 1.5 and 2.0 to make the approximate shock response spectra typically conservative.

The design guides propose a rough approach of the in-structure shock of underground structures. Empirical formulas are given based on a limited amount of test data (TM-5-855-1). However, obviously, the predictions of in-structure shock of underground structures in design codes such as TM-5-855-1 are over-simplified. First, the displacement, velocity and acceleration of the structure subjected to a subsurface detonation are calculated only based on the free field soil motion. The properties of the structure, i.e. the dimensions and thickness of the structural members which defines how hollow the structure is, are completely ignored. In fact, these predicted responses are the values in the geometric center of the buried structure. Second, the soil-structure

interaction, is also neglected. In addition, it is not clear how the approximate shock response spectra are constructed based on the peak in-structure displacement, velocity and acceleration. Generally, to construct shock response spectra (or seismic response spectra), a time history of excitation acceleration time history is needed.

### **2.3.2 Research on in-structure shock of underground structures**

With dynamic soil-structure interaction incorporated, Weidlinger and Hinman (1988) used an SDOF model to delineate the motion characteristics of an underground structure subjected to a subsurface blast. The whole structure is assumed as a rigid body and rigid body displacement and velocity were derived.

Further, Alwis and Lam (1994) studied the rigid body response of underground protective structures under exponentially decreasing blast load using an SDOF model. The soil-structure interaction, in nature, transmission and reflection of stress wave at interface of two different materials, was incorporated into the analysis and shock response spectrum (SRS) was obtained based on the calculated rigid body response.

In early years, only considering the rigid body motion of a buried structure in the analysis of the in-structure shock was sufficient. With the development of the warhead penetration capacity in the past decades, the in-structure shock induced by the local structural response becomes a major concern to the safety of the interior contents. When the blast wave encounters an underground structure, it causes not only global motion of the whole structure, but also a sudden deflection of structural elements, which in turn acts as an excitation to the equipment attached. Yang (1994) investigated the response of buried shelter to blast loadings due to conventional weapon detonation with FEM, using commercial code ABAQUS. Empirical formulas were used to calibrate the input parameters of the numerical model. After the structural member responses were computed, shock response spectra of the equipment mounted to the shelter were constructed. The difference between this model and the previous two



works is that the deflection of the structural member is considered to construct the response spectra. However, the relevant information appears to be scarce because of the confidential nature of the subject.

## **2.4 In-structure shock mitigation of underground structures**

There are various methods to mitigate in-structure shock of underground structures subjected to a soil-transmitted blast load, mainly categorized into two major groups: one is modifying the surrounding soil so that the load applied on the structure is reduced; the other is modifying the structure itself to make the shock experienced by the equipment within the structure lower.

For the former category, first, the underground structure should be buried in site with soft soil. If this requirement cannot be satisfied, the soil surrounding the structure should be backfilled with soft soil. In addition, placing barrier such as PVC tubes between the detonation and the structure can attenuate the blast to some degree (e.g. Kobiela et al. 2007). Similarly, barriers of the other forms can be employed (Wang et al. 2010). For instance, making an open trench, placing a concrete plate in the soil as well as infilling an excavated trench with a layer of geofoam (a typical geofoam is Expanded Polystyrene (EPS) foam, which is a lightweight material, made by expansion of raw plastic beads).

For the latter category, to ensure the serviceability of the equipment attached to the buried structures, various measures should be taken within the structure. For horizontal shock, steel shots are used to allow the equipment with support to roll freely and nylon ropes are used to prevent its excessive movement (Waymire 1989). For vertical shock induced by incident floor motion, the general mitigation philosophy is to use a system to dissipate energy imparted by the relative motion between the moving floor and the equipment with supporting, i.e. adding a crushable foam layer; or provide a so-called 'shock impedance mismatch' which causes poor coupling between the floor and the

equipment (Waymire 1989). For certain device in a traditional underground structure, a separate isolator can be applied to mitigate in-structure shock.

However, for different shock-sensitive devices in an underground structure, testing, design and installation of such separate isolators are expensive, labor-intensive and time-consuming. More important, to mitigate in-structure shock on personnel in underground structures, the only way is to reduce shock level, rather than add isolators.

## 2.5 Cellular solids and structures

Cellular solids are a kind of material with struts and plates interconnected as networks while cellular structures are structures formed with thin-walled plate or struts regularly stacked (Gibson and Ashby 1997). They can be roughly categorized as honeycombs and foams. For foams, there are mainly two types: open-cell foam, through which fluid can flow; and close-cell foam, through which fluid cannot flow, shown in Fig. 2.3. Compared to the general solids, cellular solids have many exceptional properties such as low thermal conductivity, being lightweight. These advantages over the solid counterpart make it versatile in applications: thermal insulation, vibration isolation and packaging, bio-compatible components, filters, structural construction, sound suppression and energy absorption.

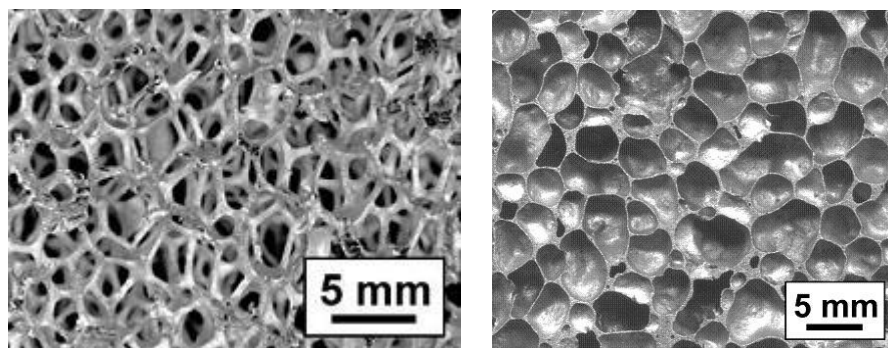


Fig. 2.3 Open-cell and close-cell metal foams

Among various properties of cellular solids, the most important one is the relative density, defined as the ratio of the cellular solids to the base material from which it is made. In fact, many other features such as Young's modulus, yield strength, plateau stress, densification strain are dependent on the relative density. Conventionally, only the cellular solids with relative density less than 0.3 are considered as typical. Cellular solids with relative density greater than 0.3 are generally treated as solids containing isolated pores or voids (Gibson and Ashby 1997).

It is worth noting that the literatures for cellular materials are a huge collection, not possible exhaustively reviewed in the thesis. Therefore the author selects and covers some significant findings and contributions.

### **2.5.1 Compression of cellular solids**

Among the behaviors of cellular solids under mechanical loads such as bending, shear, tension and compression, compression response is most important. When a cellular solid is compressed, three clearly-defined stages are observed. Initially, when the nominal strain is small, stress-strain curve is a straight line, whose mechanism is that cell walls undergo elastic bending of small deflection. Second, when the strain increases, the stress-strain curve is in a plateau with large strain but almost constant stress, where the cell walls buckle elastically, collapse plastically or fracture brittly (Lu and Yu 2003). With further development of the strain, an increasing number of cell walls buckle. Finally, when the strain is sufficiently large, stress increases with strain dramatically, whose mechanism is the collapsed cell walls are compressed together and compacted firmly.

It should be noted that in the second phase, the stress being almost constant for a nominal strain up to 0.7 or 0.8, forms a plateau. This property makes it an efficient energy absorber.

Ruan et al. (2002) experimentally studied the compressive behavior of close-cell metal foam under low and medium strain rates ranging from  $10^{-3}$  to  $10^1 \text{ s}^{-1}$ . It is found that the deformation is not uniform over the whole specimen. The deformation mechanism is that the weakest part is crushed first and the second weakest part next. The next weakest part is not crushed until the weakest part is completely densified.

### 2.5.2 Plateau stress and densification strain

Cellular materials consisting of two-dimensional cells with the third dimension solid are called honeycombs. If the cells of the cellular solids are three-dimensional, they are called foam, which we will focus on in this thesis.

In compression, two parameters are of special significance: the plateau stress and densification strain. The plateau stress of cellular solids is governed by the following mechanism: elastic buckling, plastic collapse and brittle fracture (Lu and Yu 2003). For typical low density open-cell foam, the plateau stress can be empirically determined as:

$$\sigma_{pl} = C_1 \left( \frac{\rho}{\rho_s} \right)^{\frac{3}{2}} \sigma_{ys} \quad (2.5)$$

where  $\rho$  is foam density and  $\rho_s$  is density of the base material from which the foam is made.  $C_1$  is a constant obtained from experiment, 0.25 to 0.35 for aluminum foam (Ashby et al. 2000).  $\sigma_{ys}$  is the base material yield strength. If the foam is close-celled, the influence of trapped air cannot be neglected and other empirical formulas are given (Lu and Yu 2003).

The densification strain, defined as the strain at which the densification occurs, is empirically expressed as:

$$\varepsilon_D = 1 - \lambda \frac{\rho}{\rho_s} \quad (2.6)$$

where  $\lambda$  is a constant determined by a number of tests, taken as 1.4 or 1.5 (Ashby et al. 2000). The physical meaning of  $\lambda$  can be illustrated as follows. After densification, the density of the foam becomes:

$$\rho^* = \frac{\rho}{1 - \varepsilon_D} \quad (2.7)$$

Combination of Eq. (2.6) and Eq. (2.7) yields:

$$\rho^* = \frac{\rho_s}{\lambda} \quad \lambda = \frac{\rho_s}{\rho^*} \quad (2.8)$$

From Eq. (2.8), it is straightforward to know  $\lambda$  is the ratio of base material density to the foam density after densification, which reflects how compact or firm the foam is crushed for a given load. In fact,  $\lambda$  should be a function of the compressive load intensity and the value of  $\lambda$  should approach 1 if the foam is compressed by a load with extremely high intensity, especially for open-cell foams.

## 2.6 Dynamic behaviors of cellular materials

### 2.6.1 Different crushing modes

When cellular solids and structures are subjected to dynamic load, the mechanical behaviors are different from those under quasi-static load. When the crushing velocity is low, the compression of foam without defects is in a uniform manner, similar to that under quasi-static load; and foam with defects crushed from the defects. For ideal honeycomb and foams, at first, when they are initially crushed in a low velocity, localized band develops within them; with the advance of the loading, more and more localized bands occurs, until the honeycomb or foam is entirely crushed.

When the impact velocity is sufficiently high, for instance, 50-70 m/s, the deformation mechanism is totally different: the densification is highly localized in the impact end,

where the honeycomb or foam is crushed to densification strain. In other part, no localized band, even no deformation occurs. This crushing or densification propagates progressively from the impact end with the advance of the compressive loading.

In a crushing velocity between these two velocities mentioned above, the foam densification is in a transition manner. It is a combination of the global deformation and progressive collapse. Localized bands occur within certain area from the impact end and other foam outside this region does not deform (Lu and Yu 2003).

It is evident that the critical velocity does exist for specific foam, above which the foam will undergoes progressive collapse. It may depend on the cell wall thickness, cell wall length-to-thickness ratio, foam relative density, strain rate dependency of the base material, etc. However, until now, this critical velocity is not successfully predicted yet in the sense of mechanism.

## **2.6.2 Material models for dynamic crushing with applications**

### *Rigid-perfectly-plastic-locking model and other similar models*

Among all the models delineating the metal foams under high velocity crushing, the most important model is the shock model based on rigid-perfectly-plastic-locking (RPPL) idealization, briefed as follows.

Reid and Peng (1997) experimentally studied the high velocity impact of wood and found that the crushing is localized and propagates like a shock wave front. Based on the observation, a rigid-perfectly-plastic-locking (RPPL) model was proposed to theoretically describe the crushing process. It is found that the model is successful in predicting the wood response under high velocity impact, especially suitable for modeling the dynamic enhancement. This model was widely applied to delineate and predict the responses of various foam-like materials and structures, i.e. metal foam.

Hanssen et al. (2002) carried out full-scaled field test to study the responses of a metal foam- attached panel subjected to blast loads. A ballistic pendulum was used. It is found that the energy and impulse transmitted to the pendulum increases by adding the metal foam, which means the mitigation effect is negative. Further, one-dimensional foam subjected to blast load using shock theory is analyzed theoretically and it is found that the global response of the pendulum is not altered by adding the metal foam.

Tan et al. (2005a, 2005b) experimentally and theoretically investigated the dynamic compressive strength of homogeneous metal foam. Different from others, they used a direct-impact technique and found that the collapse strength is significantly dependent on the compression rate. Lopatnikov et al. (2003) used Taylor cylinder-Hopkinson bar test to investigate the dynamic behavior of foam under high velocity compression. A theory was proposed and compared favorably with the test results. During the test, the shock fronts were clearly captured, indicated in Fig. 2.4.

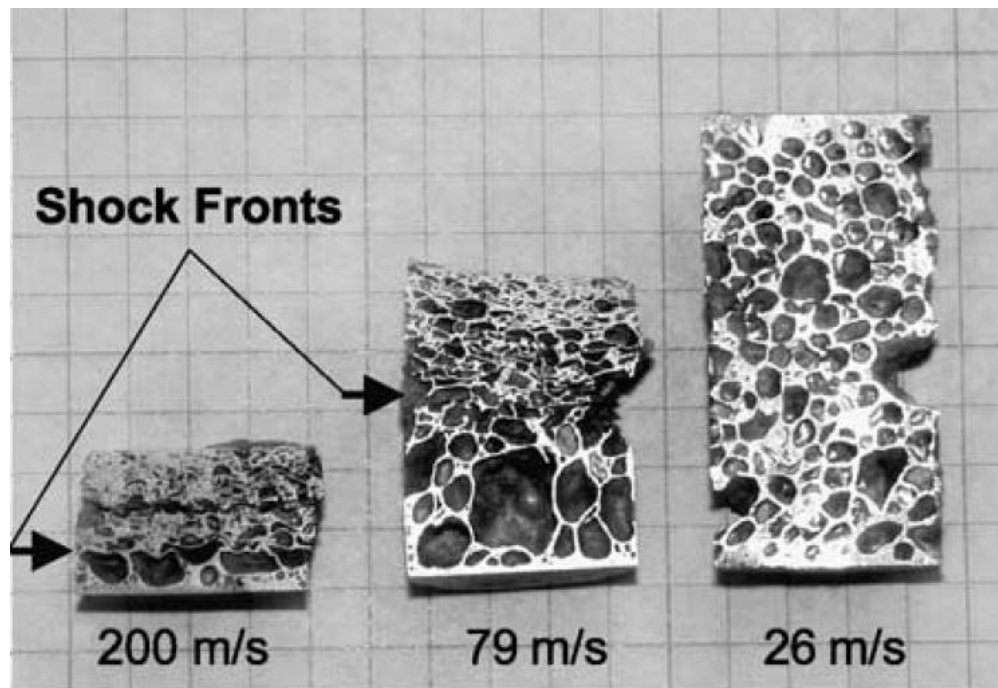


Fig. 2.4 Shock fronts under various impact velocities (Lopatnikov et al. 2003)

Deshpande and Fleck (2005) theoretically investigated the dynamic response of sandwich plates under impulsive loading. The effect of strain hardening of the foam core is studied and it is found that for realistic mass ratio of core to face sheet, the strain hardening effect can be neglected. Further, sandwich response to underwater explosion was analyzed.

Guruprasad and Mukherjee (2000a, 2000b) experimentally and theoretically studied the responses of layered sacrificial cladding under blast loading. The cladding was constructed with thin mild steel sheets, stacked layer by layer. Each layer of the cladding is the same, which makes the overall configuration resembles that of the homogeneous foam. It is found that under blast load, the cladding collapses progressively from the surface nearest to the explosion to other part.

In preceding reviews, for most of the cases, only the foams or claddings themselves were studied. Ma and Ye (2007a), as well as Ye and Ma (2007) examined the responses of the system consisting of not only the blast and cladding, but also the protected structure, called a load-cladding-structure (LCS). They explained why sometimes the protection effect is negative, that is, the responses are even higher than the cases without foam cladding. Further, design maps are established for effective mitigation of blast using metal foam cladding. Besides, Ma and Ye (2007b) also investigated the double-layered blast mitigation cladding.

Lopatnikov et al. (2004) theoretically examined the high velocity impact on metal foam. Four discrete impact velocity divisions were established. Two of these regimes are of special significance and discussed in detail: one is the impact velocity higher than the elastic wave speed of the foam, the other is the impact velocity smaller than the elastic precursor but higher than the effective sound velocity corresponding to the plateau region. Different mechanism was discussed.

Li and Reid (2006) discussed some fundamental problems on dynamic foam crushing, including physical quantity jump at the shock front, effective sound velocity and impact velocity, as well as the ‘strain frozen’ assumption. They also analyzed the



Colombia space shuttle accident. Li et al. (2006) also examined several commonly used definitions of the onset of the densification strain and clarified the ambiguity of them. It is found that the densification strain onset determined by the energy absorption efficiency is unique and consistent.

Harrigan et al. (2010) theoretically re-examined the shocks in cellular materials. They clarified some conflicting predictions for the response of cellular solids in some loading situations. Different analytical approaches were discussed with examples.

Zhu et al. (2009) theoretically optimized a rectangular blast mitigation sandwich panel with the objective as the minimal permanent maximum deflection, for given mass and loads. The governing mechanism was analyzed and the key control parameters are identified as ratio of the two side lengths, relative density of foam core as well as core thickness.

Generally the blast mitigation claddings are flat, compatible with the plane surfaces of the protected structure. Further, in applications, curved sandwich panels are also widely used in marine vessels and civil infrastructures. Shen et al. (2010) experimentally investigated the responses of curved sandwich panels subjected to blast loading using a four-cable ballistic pendulum, where four edges of the panel were fully clamped. It is found that the collapse mode was changed by the initial panel curvature and the performance of panel is superior to that of the flat counterpart.

In addition, some other model, are further developed based on this RPPL model. RPPL model ignores the elastic response of the foam, by assuming it absorbs negligibly small energy in a small strain range. Harrigan et al. (2010) compared the difference between the RPPL model and the more refined elastic-perfectly-plastic-enhancement (EPPH) model, which considered the elastic wave propagation and enhancement after which the densification strain is reached.

*FEM model: Voronoi or honeycomb model*

Ma et al. (2009) conducted numerical simulation using Voronoi meso-scaled model, finding the densification stress at the stationary end is insensitive to the strain rate while it is strongly rate-dependent at the impact end.

Zou et al. (2009) numerically simulated the two-dimensional honeycomb under dynamic crushing using FEM. It is found that when the crushing velocity is higher than a critical value, shock front forms with thickness as a cell size. Densification strain increases with increasing crushing velocity and converges to a value once the critical velocity is achieved, where a shock front foams. The study numerically validated the rigid-perfectly-plastic-locking (RPPL) model and pointed out the RPPL model slightly over-estimates the densification stress and energy absorption.

#### *FEM model: Continuous model in hypercodes*

With the wide application of the metal foam in the fields of marine vessels, civil infrastructures and military vehicles, several leading commercial software such as ANSYS/LS-DYNA and ANSYS/AUTODYN also developed and implemented foam model into their hypercodes. The detailed micro-structure is ignored and the foam is idealized as continuous solid, whose usage is exactly the same as other solid materials.

#### *Spring model*

Besides continuous models, Shim et al. (1990) proposed a discrete model describing the dynamic behavior of cellular materials. This one-dimensional model discretizes each layer of cell into a lumped mass and a massless spring and idealized the cellular material into a series of such mass and springs. The governing equations for each layer/cell were established and solve numerically.

However, Harrigan et al. (2010) found that the mass-spring models has disadvantage in predicting the shock behavior of foams thus it should be examined carefully if used.

### **2.6.3 Gradient foam**

The mechanical behavior of homogeneous foam subjected to high velocity crushing was intensively investigated in the past decades. Recently, research on dynamic properties of non-homogeneous foam emerged. Roughly, there are two categories of non-homogeneous foams: first, several layers of homogeneous foams with different relative densities stacked together to form a step-wise gradient foam; the other is foam with continuous relative density variation.

Beals and Thompson (1997) experimentally investigated the static compression behavior of gradient foam. It is found that the crushing is initiated from the weakest part- the layer with lowest density, then the next weakest layer, until the whole foam specimen is completely densified. This progressive collapse from the weakest foam part is the same as the homogeneous foam with defect and the phenomenon is the same as expected. However, if the crushing velocity is sufficiently high, things may be different.

Kiernan et al. (2009) numerically studied the gradient foam with FEM. After calibrating the FEM model with a SHPB test on homogeneous foam, the calibrated numerical SHPB test is employed to investigate the wave propagation properties of gradient foam. It is found that the energy dissipation is shaped by the gradient.

Sun et al. (2010) studied the gradient foam filled thin-wall structure under low velocity impact using FEM. It is found that the gradient foam filled structure is superior to its uniform counterpart in overall crashworthiness. Cui et al. (2009) conducted FEM simulation for gradient foam under impact and found the similar conclusion: the energy absorption characteristics are improved by the gradient. The large the density difference, the more efficient is the energy absorption. The same conclusion is also achieved by Ajdari et al. (2011) based on the FEM simulation.

Zeng et al. (2010) experimentally tested the hollow sphere agglomerates with density gradient subjected to impacts (impact velocity less than 50 m/s). The density gradient was achieved by putting four layers of agglomerates together. They found that the energy absorption capacity is not changed. Further, a numerical simulation is performed with higher impact velocity and it is found that placing the hardest layer near the impact end and weakest layer as the last layer have some merits in energy absorption.

### **3 IN-STRUCTURE SHOCK OF UNDERGROUND STRUCTURES: THEORETICAL ASSESSMENT**

Some structures installed or submerged in certain media may be subjected to media-transmitted dynamic loads. Typical cases are blast load on underground structures induced by surface or subsurface detonations and load on submarines by underwater explosions. To effectively design such structures under media-transmitted dynamic loads, it is necessary to estimate the loads applied on them and calculate the structural responses. Amongst, the dynamic media-structure interaction plays an important role in determining the load applied on the structures. Therefore, understanding the interaction mechanism and effect becomes a prerequisite.

A plate model is proposed, which can provide more information than the single-degree-of-freedom interaction model in terms of higher mode responses. Furthermore, according to Kiger (1998), the use of dynamic soil-structure interaction (SSI) damping in plastic structural analysis should be avoided. Therefore in the present study, the structural deformation is assumed elastic.

In this chapter, the dynamic soil-structure interaction is introduced first, followed by a detailed discussion on the effect of the interaction on the structural responses. Then, with one representative strip of a buried structure modeled as a modified Euler beam, the in-structure shock of an underground structure subjected to a subsurface blast is theoretically analyzed, with SSI incorporated. In addition, shock response spectra are employed to evaluate the safety of the devices within the structure and a case study is conducted.

#### **3.1 Dynamic soil-structure interaction**

In fact, the nature of the SSI is the load mitigation caused by the particle velocity difference between the soil and the structure. The soil particle velocity is determined directly by the free-field pressure and independent of the structural response: it is calculated as the free-field pressure divided by the acoustic impedance of soil. However, the particle velocity of certain material point in the structure differs in location and time. At the instant of arrival of the incident stress wave on a buried structure, the velocity of the structure is zero and free field soil-transmitted blast is fully reflected thus the pressure applied is twice the free field value. With the deformation of the structure, the pressure applied is mitigated to some degree and the amplification factor, defined as the ratio of the pressure applied on the structure to the incident pressure, is less than 2 although the value of the pressure applied does not necessarily decrease and may even increase. This load alleviation effect is caused by the existence of the structure material point velocity in terms of the rigid body motion or structural deformation, or both. This qualitative analysis delineates the cause and nature of the SSI effect on underground structures subjected to dynamic loads. However, the aspects influencing the SSI cannot be identified only based on the qualitative analysis. Therefore quantitative analysis of the SSI effect is also conducted and the factors affecting the SSI are discussed.

Before quantitative analysis, some assumptions are listed:

First, the free field ground shock is modeled one-dimensional. Typically, when in-structure shock is the major concern, the standoff distance from the charge center and the structure should be moderate. Subsequently, the curvature of the ground shock is significantly small compared to a typical underground structure thus neglected. However, if the subsurface detonation is close to the structure, the structure will undergo large, plastic deformation even damaged, which is out of the scope of the present study.

Second, the structural response is elastic. As stated in the item above, when the standoff distance between the charge center and the structure is relatively distant, the

intensity of the ground shock at the structure is moderate. Subsequently, the structural deformation is small compared to the member dimensions, within the elastic limit.

Third, a structural member of the underground structure is modeled as a simply supported concrete plate with unmovable edges. A typical underground structure is a large hollow concrete box. The edge constraints of one slab to others are between simply supported and clamped. For conservative design purpose, they are modeled as simply supported. In addition, due to the huge total mass of a typical underground protective structure, the rigid body motion is significantly small and ignored thus the supports are modeled unmovable.

Fourth, further, the soil and plate are in perfect contact with each other and there is no separation. It is well known that soil cannot withstand tension. If in some instants when the velocity of the structural member is larger than the soil particle velocity, separation between the soil and the structural member occurs. In the present thesis, the separation is not considered, which will lead to a conservative prediction of the in-structure shock. Further, the difference between predictions with and without consideration of the separation is discussed in Section 5.4.

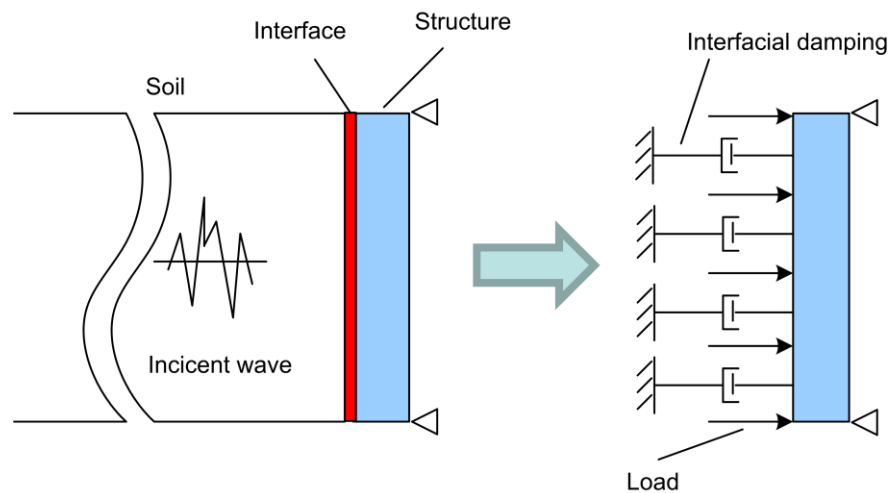


Fig. 3.1 A structure in soil subjected to a soil-transmitted dynamic load and its analytical model (in fact, the interface, highlighted in red, has zero thickness)

For a plate subjected to a dynamic excitation, the governing equation is:

$$D\nabla^4 w(x, y, t) + \rho h \frac{\partial^2 w(x, y, t)}{\partial t^2} = P(x, y, t) \quad (3.1)$$

where  $D = \frac{Eh^3}{12(1-\nu^2)}$  is the flexural rigidity of the plate;  $\rho$  and  $h$  are density and thickness of the plate, respectively;  $w$  the displacement or deflection of any point in the plate;  $t, x, y$  the time and two axes with origin at one corner of the plate;  $E, \nu$  Young's modulus and Poisson's ratio of concrete, respectively.  $P(x, y, t)$  is the load time history applied on the plate.

When a compressive propagating in soil encounters a concrete plate, as shown in Fig. 3.1, it is partially reflected and partially transmitted at the interface, defined as the layer with zero thickness between the structure and the surrounding soil. Compared to concrete, the acoustic impedance of soil is smaller, permitting the reflected wave is compressive provided that the incident wave is compressive. The load applied on the plate is the sum of the free field pressure time history and the reflected wave (Wong and Weidlinger 1983), which can be expressed as

$$P(x, y, t) = 2\sigma_f(x, y, t) - \rho_s c_s \frac{\partial w(x, y, t)}{\partial t} \quad (3.2)$$

where  $\sigma_f(x, y, t)$  is the free-field stress time history at the interface of soil and concrete plate;  $\rho_s c_s$  acoustic impedance of soil.

Combination of Eq. (3.1) and Eq. (3.2) yields:

$$D\nabla^4 w(x, y, t) + \rho h \frac{\partial^2 w(x, y, t)}{\partial t^2} + \rho_s c_s \frac{\partial w(x, y, t)}{\partial t} = 2\sigma_f(x, y, t) \quad (3.3)$$



In Eq. (3.3), the effect of SSI is mathematically defined in the governing equation: a damping term is introduced, which has an effect of reducing the structural response, indicated in Fig. 3.1.

With the boundary condition taken as simply supported, the plate deformation can be expressed:

$$w(x, y, t) = \sum_{m=1}^{\infty} \sum_{n=1}^{\infty} W_{mn}(x, y) \eta_{mn}(t) \quad (3.4)$$

where  $W_{mn}(x, y)$  is the  $m, n$ th mode shape and  $\eta_{mn}(t)$  the  $m, n$ th generalized coordinate. From Eq. (3.3) and the boundary condition, the  $m, n$ th mode shape can be readily determined as

$$W_{mn}(x, y) = \frac{2}{\sqrt{\rho h a b}} \sin \frac{m\pi x}{a} \sin \frac{n\pi y}{b} \quad (3.5)$$

where  $m, n$  and  $a, b$  are mode numbers and two in-plane dimensions of the plate, respectively. Substituting (3.4) into (3.3), the governing equation for the plate is:

$$\begin{aligned} & \rho h \sum_{m=1}^{\infty} \sum_{n=1}^{\infty} W_{mn}(x, y) \ddot{\eta}_{mn}(t) + \rho_s c_s \sum_{m=1}^{\infty} \sum_{n=1}^{\infty} W_{mn}(x, y) \dot{\eta}_{mn}(t) \\ & + D \sum_{m=1}^{\infty} \sum_{n=1}^{\infty} \nabla^4 W_{mn}(x, y) \eta_{mn}(t) = 2\sigma_f(x, y, t) \end{aligned} \quad (3.6)$$

Take into account the relationship between the differential and original forms of mode shape, Eq. (3.6) can be further written as:

$$\begin{aligned} & \rho h \sum_{m=1}^{\infty} \sum_{n=1}^{\infty} W_{mn}(x, y) \ddot{\eta}_{mn}(t) + \rho_s c_s \sum_{m=1}^{\infty} \sum_{n=1}^{\infty} W_{mn}(x, y) \dot{\eta}_{mn}(t) \\ & + \sum_{m=1}^{\infty} \sum_{n=1}^{\infty} \pi^4 D \left[ \left( \frac{m}{a} \right)^2 + \left( \frac{n}{b} \right)^2 \right]^2 W_{mn}(x, y) \eta_{mn}(t) = 2\sigma_f(x, y, t) \end{aligned} \quad (3.7)$$

Multiply Eq. (3.7) with  $W_{mn}(x, y)$  and integrate both sides from 0 to  $a$  and 0 to  $b$ , with respect to  $x$  and  $y$ , respectively. Recall the orthogonality condition of modes (Clough and Penzien 1993), the governing equation for the  $m, n$ th mode in generalized space is:

$$\ddot{\eta}_{mn}(t) + \frac{\rho_s c_s}{\rho h} \dot{\eta}_{mn}(t) + \omega_{mn}^2 \eta_{mn}(t) = \int_0^a \int_0^b 2\sigma_f(x, y, t) W_{mn}(x, y) dx dy \quad (3.8)$$

where the natural frequency of  $m, n$ th mode is

$$\omega_{mn} = \pi^2 \sqrt{\frac{D}{\rho h} \left[ \left( \frac{m}{a} \right)^2 + \left( \frac{n}{b} \right)^2 \right]} \quad (3.9)$$

From Eq. (3.8), the presence of the interface between soil and structure introduces a viscous damping item into the governing equation of certain mode of the plate subjected to a dynamic load, termed as interfacial damping. To investigate this damping effect, define the interfacial damping ratio:

$$\zeta_{mn} = \frac{\frac{\rho_s c_s}{\rho h}}{2\omega_{mn}} = \frac{\frac{\rho_s c_s}{\rho h}}{2\pi^2 \sqrt{\frac{D}{\rho h} \left[ \left( \frac{m}{a} \right)^2 + \left( \frac{n}{b} \right)^2 \right]}} \quad (3.10)$$

Substituting the expression of flexural rigidity of the plate into Eq. (3.10), the interfacial damping ratio can be simplified and rewritten as:

$$\zeta_{mn} = \frac{1}{\pi^2} \frac{\rho_s c_s}{\rho c} \sqrt{3(1-\nu^2)} \frac{\left( \frac{a}{h} \right)^2}{\left( \frac{a}{b} \right)^2 n^2 + m^2} \quad (3.11)$$

It can be seen from Eq. (3.11) that many factors from both the plate and the surrounding soil, i.e. acoustic impedance, Poisson's ratio and geometrical dimensions as well as the mode number of the concrete plate, contribute to the damping ratio. Further, the ratio can be generalized as two functions multiplied:

$$\zeta_{mn} = Kf(\lambda, \nu)g(\gamma, \varphi, m, n) \quad (3.12)$$

where  $K = \frac{1}{\pi^2}$ ,  $f(\lambda, \nu) = \lambda \sqrt{3(1-\nu^2)}$ ,  $\lambda = \frac{\rho_s c_s}{\rho c}$ ,  $g(\gamma, \varphi, m, n) = \frac{\gamma^2}{\varphi^2 n^2 + m^2}$ ,  $\gamma = a/h$ ,  
 $\varphi = a/b$ .

In Eq. (3.12), specifically,  $f$  is a material property function which includes the ratio of acoustic impedance of the soil to concrete plate as well as the Poisson's ratio of the plate.  $g$  is a function of mode numbers and plate geometrical configuration.

### 3.2 Factors affecting the dynamic soil-structure interaction

To understand the effect of the DSSI on the plate response, some factors of potential significance are discussed. According to structural dynamics, the effect of viscous damping on a system is not monotonic, which does not necessarily mean the larger the damping ratio, the greater the damping effect. In fact, viscous damping has greatest effect when the damping ratio is exactly equal to unity. Therefore only based on Eq. (3.11), it is not possible to predict whether the damping effect becomes stronger or not when the damping ratio increases. The information is not sufficient until a specific damping ratio is calculated. To illustrate, a case study is conducted: the ratio of  $a/b$  and  $a/h$  are assumed to be 2 and 20, respectively. Fig. 3.2 shows the first several order interfacial damping ratios of the system consisting of the concrete plate and surrounding wet sandy clay with an acoustic impedance of 1.917 Mkg/s. It is clear that some of the lower modes are overdamped while the higher modes are underdamped.

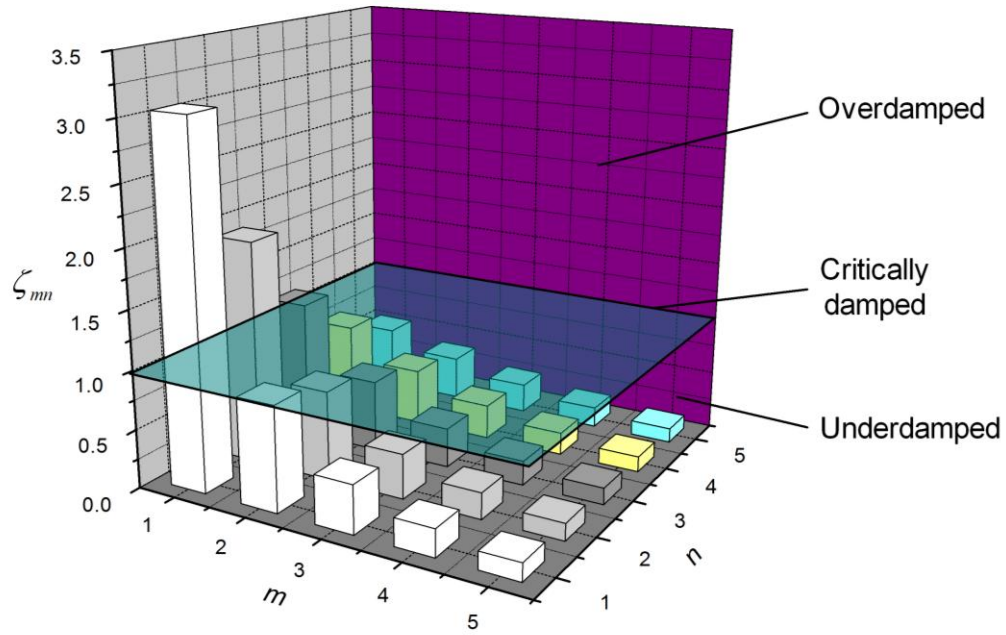


Fig. 3.2 Interfacial damping ratios of a system consisting of certain concrete plate and surrounding wet sandy clay

#### *The effect of structure thickness*

If the ratio  $a/h$  decreases with other parameters fixed, that is, the concrete slab becomes relatively thicker, from Eq. (3.11), the damping ratio of every mode will decrease. In limit condition, the thickness of the plate becomes infinity, then the interfacial damping ratio of each mode will be very small, nearly zero. In physical point of view, if the plate is no longer a concrete layer, but a very thick structure such as a rod, the interfacial damping can be negligible, which is in agreement with classic acoustic theory (Zukas et al. 1982). It is worth noting that the Kirchhoff plate theory is employed to derive the above formulas, which implies that the deflection-to-thickness ratio and thickness-to-characteristic in-plane dimension ratio should be small. However, this limit condition analysis can also shed some light on understanding the interfacial damping.

Of particular interest, the relationship between some of the interfacial damping ratios and the in-plane length-to-thickness ratio  $a/h$  is illustrated in Fig. 3.3 while all other parameters are fixed. It is demonstrated that the interfacial damping ratios increase with the in-plane length-to-thickness ratio, which implies the damping ratio is larger when the plate has smaller thickness and larger in-plane dimensions. From Eq. (3.11), another significant point is that the interfacial damping ratios are dependent on the plate shape rather than its size.

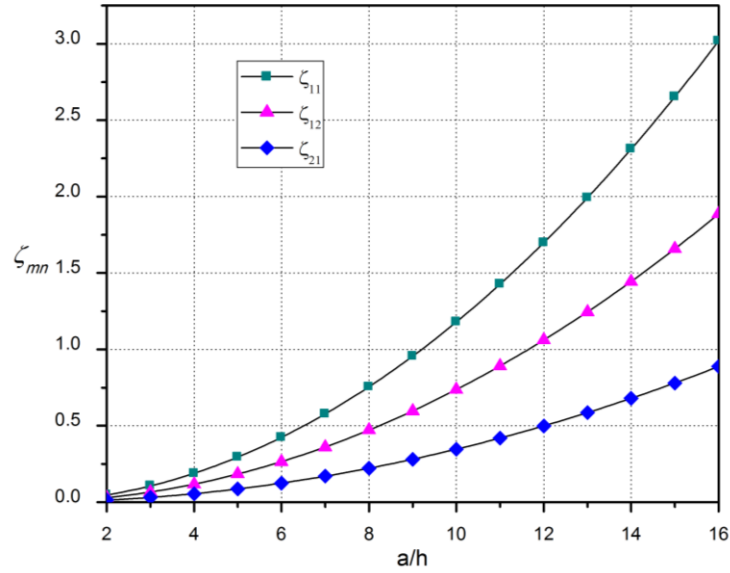


Fig. 3.3 The effect of  $a/h$  on the interfacial damping ratio

#### *The effect of the mode numbers*

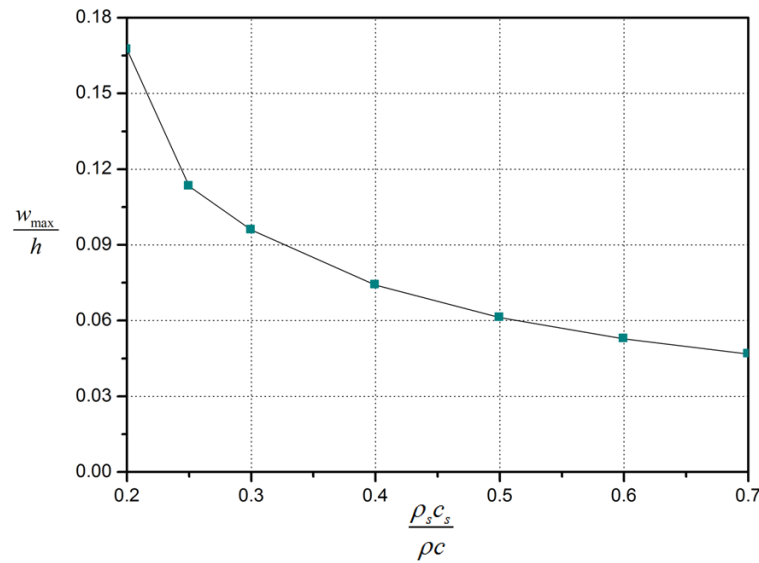
It can be seen from Eq. (3.11) that increasing the mode number of the plate results in a decrease of the interfacial damping ratio, which means the interfacial damping ratio is larger in lower modes and smaller in higher modes.

#### *The effect of in-plane dimensions*

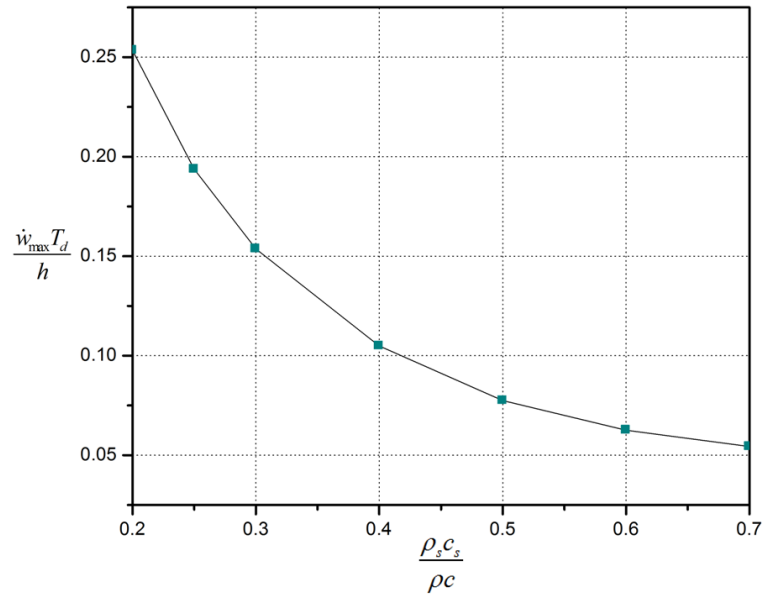
Increase the ratio of in-plane dimensions  $a/b$  with other parameters fixed, that is, decrease  $b$ , the interfacial damping ratio will become smaller, which has the same effect as increasing the plate thickness.

*The effect of acoustic impedance ratio of soil to structure*

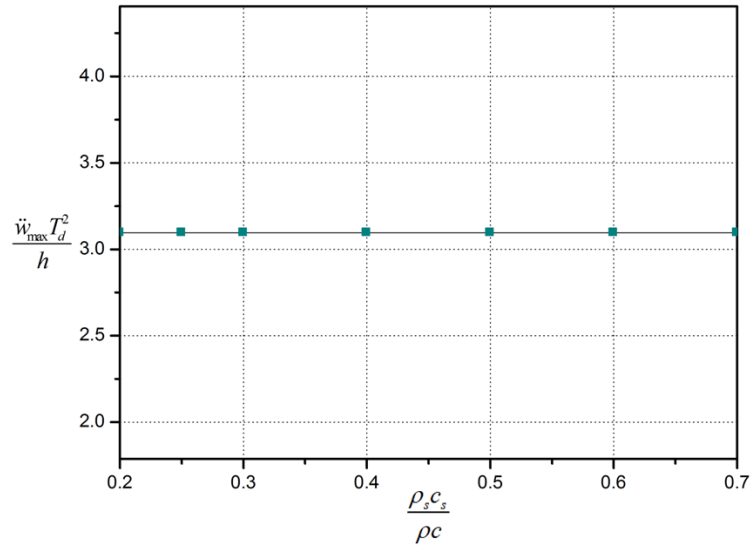
The acoustic impedance of a material is an indicator of its density and the rigidity. In the present case study, when the concrete plate is subjected to a soil-transmitted triangular dynamic load with short duration, changing the impedance of surrounding soil while keeping that of the concrete unchanged illustrate the relationship between the maximum responses of the plate and the acoustic impedance ratio of soil to structure. From Fig. 3.4, the maximum deflection and maximum velocity at the plate center decreases while the maximum acceleration stays unchanged with the increase of the acoustic impedance ratio.



(a)



(b)



(c)

Fig. 3.4 The relationship: (a) the maximum deformation (b) the maximum velocity and (c) the maximum acceleration of the plate center versus the soil-to-structure acoustic impedance ratio,  $h$  is the plate thickness and  $T_d$  is the blast duration

### 3.3 Underground explosion induced shock load and beam model for the structure

The present study is aimed to develop an integrated analytical model for the prediction of the in-structure shock of buried structures, taking into consideration the shock wave in soil, soil-structure interaction and the structural response. The essential response of the structure is represented by a beam model, while the SSI is incorporated by means of interfacial damping. For simplification and without losing generality, it is assumed that the detonation is at a certain distance away from the buried structure and so there is no significant structural damage to the buried structure. Furthermore, the burial depth is assumed to be sufficient so that there is no wave reflection from the ground surface. With the solution of the structural response, the response spectra for the sub-structures attached to the main structure are constructed.

#### 3.3.1 Underground explosion induced shock load

The intensity of the free-field stress wave generated by an underground detonation of conventional weapons may be estimated by a semi-empirical formula given in TM-5-855-1 (1986) as follows,

$$P_0 = \beta f(\rho_s c_s) \left( \frac{R}{W^{1/3}} \right)^{-r} \quad (3.13)$$

where  $P_0$  is the free-field peak pressure, in psi;  $f$  is a coupling factor of the explosion energy to soil, dimensionless. There are two steps for determining the coupling factor: first, the “scaled depth of burst” is calculated as the real burst depth divided by the cubic root of charge weight; then the coupling factor can be readily read for the calculated scaled depth from a well established graph (Smith and Hetherington 1994). The factor increases with the increasing scaled depth: from zero for a surface burst (scaled depth equal to zero) to more than 0.9 when the scaled depth is greater than 0.5



$\text{m/kg}^{1/3}$ . For a deeper burst, i.e., the scalded depth is larger than  $0.5 \text{ m/kg}^{1/3}$ , the burst can be considered as fully confined and the coupling factor can be roughly taken as 1.

$\rho_s c_s$  is the acoustic impedance of soil, in psi/fps;  $r$  is an attenuation coefficient, dimensionless;  $W$  is the TNT equivalent charge weight, in lb;  $R$  is the distance measured from the center of explosion to the structure, in ft; and  $\beta$  is a factor equal to 160 in the imperial unit system, dimensionless. It should be noted that the pressure calculated in psi is converted to SI unit system in Pa before being used in the following.

The shape of the shock wave propagating in soil resembles that of the charge. If the detonation is far from the structure as compared to the characteristic dimension of the structure, the curvature of the shock wave surface may be ignored, so that the load applied on the structure can be approximated as a plane wave, in which the arrival time difference of the actual wave to the structure is also neglected thus the pulse is a function of only time. In engineering practice, an equivalent uniform pressure is applied by multiplying the peak value with a reduction factor based on the actual load distribution. For a rectangular structural member, the factor can be readily obtained (TM-5-855-1 1986).

The temporal variation of the pressure generated by an underground explosion may be approximated by an exponential decaying law (TM5-855-1 1986), i.e.

$$P(t) = P_0 \alpha e^{-t/t_a} \quad (3.14)$$

where  $t_a$  is the travel time of the shock wave from the detonation point to the structure;  $\alpha$  is a reduction factor, defined as ratio of the equivalent uniform pressure on a wall or floor of the structure to the maximum pressure of the actual load distribution. For a typical box-typed underground structure with flat rectangular structural members, the reduction factor in a specific event is a function of the ratio of standoff distance to structural member characteristic dimension, which can be directly read from Fig. 2.2 (TM-5-855-1 1986). For a structural member of non-rectangular shape, based on the actual load distribution on the element, first the total force of the load distribution at an

instant is calculated then the equivalent uniform load can be obtained by dividing the force by the structural element area. Subsequently, according to the definition, the reduction factor can be determined. When the detonation is relatively distant, the pressure distribution is very close to that of a plane wave and the reduction factor is nearly 1. In engineering practice, the pressure time history is usually further simplified as a triangular load, such that

$$\sigma_f(t) = \begin{cases} P_0 \alpha \left(1 - \frac{t}{T_d}\right) & \text{for } t \leq T_d \\ 0 & \text{for } t > T_d \end{cases} \quad (3.15a)$$

where  $T_d$  is the equivalent blast time duration in the triangular simplification. Preserving the impulse and peak pressure as in the exponentially decreasing load yields

$$T_d = \frac{\int_0^\infty P_0 \alpha e^{-t/t_a} dt}{\frac{1}{2} P_0 \alpha} = 2t_a \quad (3.15b)$$

When the blast stress wave intersects a solid structure, the peak pressure exerted on the front face of the structure or structural element is amplified due to the refraction effect. TM-5-855-1 recommends that the peak pressure of the stress wave acting on the structural element be 1.5 times that of the respective free-field value. However, this recommendation does not consider the difference in soil types and structural stiffness, and hence is a rather crude estimation.

When the shock wave arrives at an interface with a structure, the pressure applied on the structure is the sum of the free-field pressure  $\sigma_f$  plus the reflected pressure  $\sigma_c$  (Wong and Weidlinger 1983), as

$$\sigma = \sigma_f + \sigma_c = 2\sigma_f - \rho_s c_s \dot{u} \quad (3.16)$$

where  $\dot{u}$  is the particle velocity of a structure material point. It is worth noting that the above formula is valid only in the time period when the particle velocity in the soil is

higher than that in the structure around the interface. This normally happens within the blast wave duration. When the particle velocity of soil is less than that of the structural element at the interface, the interaction between soil and structure vanishes and the pressure exerted on the structural element becomes zero.

### 3.3.2 Euler beam model

Buried structures are typically in a box-shape. Generally speaking, the response of an element of a box structure may be better represented by a plate or a slab model. As far as the governing in-structure shock is concerned, however, if the dimension of one edge is larger than twice that of the other, it is possible and convenient to further simplify the slab into a beam model, as shown in Fig.3.5. This is reasonable because the most severe in-structure shock is expected to take place in the middle section of the structure. Thus, by taking a strip of unit width parallel to the shorter edges of a wall or floor, a beam model can be established to represent the out-of-plane response of the rectangular structural member.

To simplify the solution, Euler beam theory is adopted here. With the similar process of Eqs. (3.1)-(3.3), the governing equation for a beam under the soil-transmitted blast pressure loading can be written as

$$EI \frac{\partial^4 w(x,t)}{\partial x^4} + \rho A \frac{\partial^2 w(x,t)}{\partial t^2} + \rho_s c_s \frac{\partial w(x,t)}{\partial t} = 2P_0 \alpha \left( 1 - \frac{t}{T_d} \right) \quad (3.17)$$

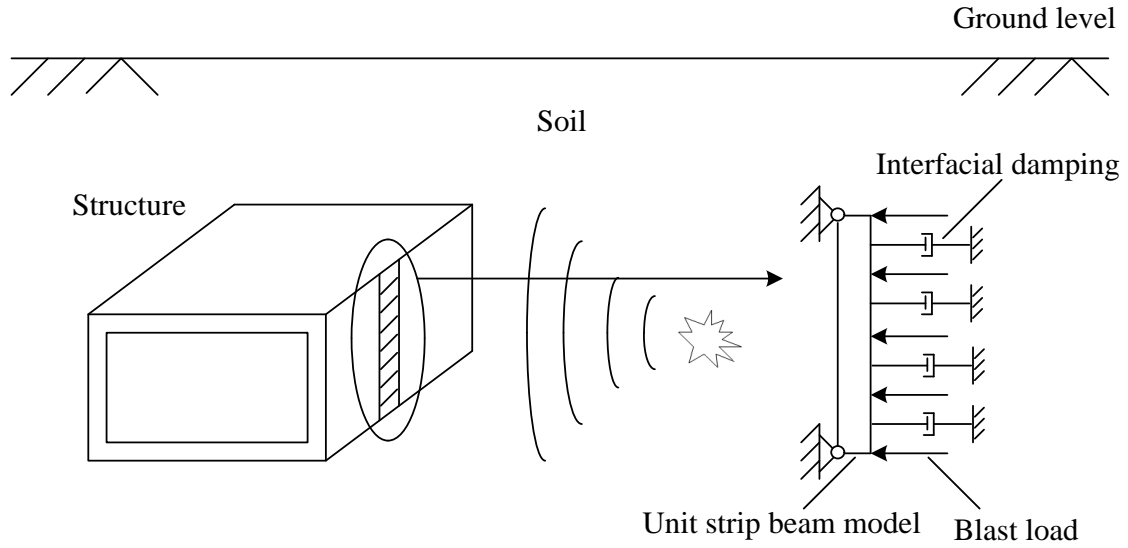


Fig. 3.5 Underground structure subjected to blast load and simplified analysis model

where  $w(x, t)$  is the displacement of the beam, which is a function of the location  $x$  and time  $t$ ;  $EI$ ,  $\rho$ , and  $A$  are the flexural rigidity, density, and area of the cross-section of the beam, respectively; Thus, the soil-structure interaction, in the form of an interfacial damping, is incorporated into the formulation of the structural response. For the elastic response of the beam, the solution of the displacement can be obtained by modal superposition, as

$$w(x, t) = \sum_{n=1}^{\infty} W_n(x) q_n(t) \quad (3.18)$$

where  $W_n(x)$  is the  $n$ th mode shape, and  $q_n(t)$  is the  $n$ th generalized modal coordinate.

The boundary condition of the Euler beam is modeled as follows. Generally, a typical monolithic box RC structure consists of six slabs. The connection of any slab to its adjacent four slabs is neither fixed nor simply supported: it is less rigid than fixed boundary and more rigid than simply supported boundary. Therefore, simply supported boundary, is adopted in the thesis, leading to conservative predictions so that in engineering practice, safer.

From the governing equation, and assuming a simply supported boundary condition (other support conditions may be considered in a similar way if necessary), the  $n$ th mode can be determined as

$$W_n(x) = \sqrt{\frac{2}{\rho A l}} \sin \frac{n\pi x}{l} \quad (3.19)$$

where  $l$  is the length of the beam;  $n$  is an integer from 1 to infinity denoting the orders of the modes.

### 3.4 Response analysis

The response of a structural member to a transient blast load consists of two phases, namely, a loading phase and a free vibration phase.

For the response within the blast duration, substituting Eq. (3.18) into Eq. (3.17) and rewriting leads to

$$\rho A \sum_{n=1}^{\infty} \omega_n^2 W_n(x) q_n(t) + \rho A \sum_{n=1}^{\infty} W_n(x) \ddot{q}_n(t) + \rho_s c_s \sum_{n=1}^{\infty} W_n(x) \dot{q}_n(t) = 2P_0 \alpha \left(1 - \frac{t}{T_d}\right) \quad (3.20)$$

where  $\omega_n = \sqrt{\frac{EI}{\rho A}} \left(\frac{n\pi}{l}\right)^2$  is the  $n$ th natural frequency of the beam. Using the orthogonal property of modes, the equation of motion for the  $n$ th mode in the generalized coordinate space can be expressed as

$$\ddot{q}_n(t) + \frac{\rho_s c_s}{\rho A} \dot{q}_n(t) + \omega_n^2 q_n(t) = 2 \left[1 - (-1)^n\right] \frac{l}{n\pi} \sqrt{\frac{2}{\rho A l}} P_0 \alpha \left(1 - \frac{t}{T_d}\right) \quad (3.21)$$

It can be seen that the interaction effect from the soil and the structure manifests as a damping. An interfacial damping ratio of the system can then be defined as

$$\zeta_n = \frac{\frac{\rho_s c_s}{\rho A}}{2\omega_n} = \frac{\frac{\rho_s c_s}{\rho A}}{2\sqrt{\frac{EI}{\rho A} \left(\frac{n\pi}{l}\right)^2}} \quad (3.22)$$

Substituting Eq. (3.22) into Eq. (3.21), the governing equation for the general mode can be written as

$$\ddot{q}_n(t) + 2\zeta_n \omega_n \dot{q}_n(t) + \omega_n^2 q_n(t) = 2 \left[ 1 - (-1)^n \right] \frac{l}{n\pi} \sqrt{\frac{2}{\rho A l}} P_0 \alpha \left( 1 - \frac{t}{T_d} \right) \quad (3.23)$$

The interfacial damping effectively represents the soil-structure interaction and it depends on the properties of both the structure and surrounding soil. Among the influencing factors are the acoustic impedance of soil as well as the structural element properties such as density, area of the cross-section, flexural rigidity and length. It should be noted that the interfacial damping ratio of the system decreases with the order of modes which means the interfacial damping effect have greater influence on lower modes and less influence on higher modes. For reinforced concrete structure buried in typical soils with density ranging from 1000 kg/m<sup>3</sup> to 2000 kg/m<sup>3</sup> and seismic velocity ranging from 300 m/s to 2000 m/s, the interfacial damping ratios of the first or first several modes are usually larger than 1, while those for the higher modes are less than 1. The continuous beam model has obvious advantage over the SDOF model in the consideration of the SSI. The effect of the interfacial damping on different vibration modes can also be reflected by the continuous beam model. The general coordinate for all modes with different interfacial damping ratio will be derived in the following.

### 3.4.1 Case I: $\xi_n \geq 1$

Let the arrival time of the blast load be time zero. Hence, at time zero both the initial displacement and velocity of the beam are zero,

$$w(x,0)=0, \dot{w}(x,0)=0 \quad (3.24)$$

The initial conditions in the generalized coordinate space can be written as

$$q_n(0)=\int_0^l \rho A W_n(x) w(x,0) dx = 0, \quad \dot{q}_n(0)=\int_0^l \rho A W_n(x) \dot{w}(x,0) dx = 0 \quad (3.25)$$

Solve Eq. (3.23) with the initial conditions, for an interfacial damping ratio larger than or equal to 1, the contribution of the nth mode to the displacement of the structural element is

$$w_n(x,t) = \sqrt{\frac{2}{\rho A l}} \sin \frac{n\pi x}{l} \left[ E_n e^{D_{n,2}t} + F_n e^{D_{n,3}t} + 2D_{n,1} \left( 1 - \frac{t}{T_d} + \frac{2\zeta_n}{\omega_n T_d} \right) \right] \quad (3.26)$$

where

$$E_n = -\frac{D_{n,1} \left[ 1 + \left( T_d + \frac{2\zeta_n}{\omega_n} \right) D_{n,3} \right]}{\omega_n T_d \sqrt{\zeta_n^2 - 1}}, \quad F_n = -\frac{D_{n,1} \left[ 1 + \left( T_d + \frac{2\zeta_n}{\omega_n} \right) D_{n,2} \right]}{\omega_n T_d \sqrt{\zeta_n^2 - 1}}$$

$$D_{n,1} = \left[ 1 - (-1)^n \right] \frac{l}{n\pi} \sqrt{\frac{2}{\rho A l}} \frac{P_0 \alpha}{\omega_n^2}, \quad D_{n,2} = \left( -\zeta_n + \sqrt{\zeta_n^2 - 1} \right) \omega_n, \quad D_{n,3} = \left( -\zeta_n - \sqrt{\zeta_n^2 - 1} \right) \omega_n$$

Subsequently,

$$\dot{w}_n(x,t) = \sqrt{\frac{2}{\rho A l}} \sin \frac{n\pi x}{l} \left( E_n D_{n,2} e^{D_{n,2}t} + F_n D_{n,3} e^{D_{n,3}t} - \frac{2D_{n,1}}{T_d} \right) \quad (3.27)$$

$$\ddot{w}_n(x,t) = \sqrt{\frac{2}{\rho A l}} \sin \frac{n\pi x}{l} \left( E_n D_{n,2}^2 e^{D_{n,2}t} + F_n D_{n,3}^2 e^{D_{n,3}t} \right) \quad (3.28)$$

It should be mentioned that the above solutions (displacement, velocity and acceleration contributions) are valid only within the time overlap of the blast duration and the time period ranging from zero to the maximum displacement.

### 3.4.2 Case II: $\zeta_n < 1$

When the interfacial damping ratio is smaller than 1, the  $n$ th order motion contribution to the displacement variable can be written as

$$w_n(x, t) = \sqrt{\frac{2}{\rho A l}} \sin \frac{n\pi x}{l} \left\{ e^{-\zeta_n \omega_n t} \left[ E_n \sin(D_{n,4}t) + F_n \cos(D_{n,4}t) \right] + 2D_{n,1} \left( 1 - \frac{t}{T_d} + \frac{2\zeta_n}{\omega_n T_d} \right) \right\} \quad (3.29)$$

where

$$E_n = \frac{2D_{n,1}}{D_{n,4}T_d} \left[ 1 - \zeta_n \omega_n \left( T_d + \frac{2\zeta_n}{\omega_n} \right) \right], \quad F_n = -2D_{n,1} \left( 1 + \frac{2\zeta_n}{\omega_n T_d} \right), \quad D_{n,4} = \sqrt{1 - \zeta_n^2} \omega_n$$

Subsequently,

$$\dot{w}_n(x, t) = \sqrt{\frac{2}{\rho A l}} \sin \left( \frac{n\pi x}{l} \right) \left\{ e^{-\zeta_n \omega_n t} \left[ -(\zeta_n \omega_n E_n + D_{n,4} F_n) \sin(D_{n,4}t) + (D_{n,4} E_n - \zeta_n \omega_n F_n) \cos(D_{n,4}t) \right] - \frac{2D_{n,1}}{T_d} \right\} \quad (3.30)$$

$$\ddot{w}_n(x, t) = \sqrt{\frac{2}{\rho A l}} \sin \frac{n\pi x}{l} e^{-\zeta_n \omega_n t} \left\{ \left[ \omega_n^2 E_n (2\zeta_n^2 - 1) + 2\omega_n \zeta_n F_n D_{n,4} \right] \sin(D_{n,4}t) + \left[ -2\omega_n \zeta_n D_{n,4} E_n + \omega_n^2 F_n (2\zeta_n^2 - 1) \right] \cos(D_{n,4}t) \right\} \quad (3.31)$$

Again the solutions are valid only within the time intersection of the blast duration and time period ranging from zero to maximum displacement.

The total displacement, velocity, and acceleration of the structural element should be the summation of contributions from different modes, i.e.,

$$w(x, t) = \sum_{n=1}^{\infty} W_n(x) q_n(t)$$



$$\dot{w}(x, t) = \sum_{n=1}^{\infty} W_n(x) \dot{q}_n(t) \quad (3.32)$$

$$\ddot{w}(x, t) = \sum_{n=1}^{\infty} W_n(x) \ddot{q}_n(t)$$

### 3.4.3 Post-blast phase

After the shock load duration is completed, the soil-structure interaction vanishes and the interfacial damping ratio becomes zero. The governing equation for the generalized coordinate during the free vibration is

$$\ddot{q}_n(t_1) + \omega_n^2 q_n(t_1) = 0 \quad (3.33)$$

Offsetting the time by the blast duration and defining  $t_1 = t - T_d$  for the free vibration phase, the initial condition for  $t_1$  is actually the terminal condition of the shock load duration. Thus, the displacement, velocity and acceleration responses of the structural element after the shock load phase are, respectively:

$$w(x, t_1) = \sum_{n=1}^{\infty} \sqrt{\frac{2}{\rho A l}} \sin \frac{n\pi x}{l} \left[ \frac{\dot{q}_n(t_1=0)}{\omega_n} \sin \omega_n t_1 + q_n(t_1=0) \cos \omega_n t_1 \right] \quad (3.34)$$

$$\dot{w}(x, t_1) = \sum_{n=1}^{\infty} \sqrt{\frac{2}{\rho A l}} \sin \frac{n\pi x}{l} \left[ \dot{q}_n(t_1=0) \cos \omega_n t_1 - \omega_n q_n(t_1=0) \sin \omega_n t_1 \right] \quad (3.35)$$

$$\ddot{w}(x, t_1) = \sum_{n=1}^{\infty} \sqrt{\frac{2}{\rho A l}} \sin \frac{n\pi x}{l} \left[ -\omega_n \dot{q}_n(t_1=0) \sin \omega_n t_1 - \omega_n^2 q_n(t_1=0) \cos \omega_n t_1 \right] \quad (3.36)$$

It should be highlighted that  $t_1$  is the start time of free vibration and the solution is applicable from that time until the displacement reaches its maximum value (if the displacement does not reach its peak value in the blast duration). In an underground

shock scenario, the maximum velocity and acceleration of the structural element are generally achieved within this period and then the responses will attenuate quickly with time. In fact, the chance of the structural member rebounding and interacting again with the surrounding soil does exist. If this happens, the equations will fail. Therefore the equations are valid before the rebound happens, in other words, they are valid until the displacement reaches its maximum value.

Further, under a subsurface detonation, both the rigid body motion of the entire structure and the local deflection of structural member occur. It is very interesting to discuss in-structure shock of underground structures subjected to subsurface detonation with both effects from local deflection and overall response-rigid body motion. However, in some situations, e.g. when the hollow box structure is relatively large and heavy, the local deflection dominates and rigid body motion effect is insignificant, just as discussed in the present study. In the future study, more generally, the rigid body motion of the entire structure will be incorporated into the model and its contribution in the in-structure shock will be analyzed.

### **3.5 A case study of response analysis using beam model**

Consider a box-shaped underground buried structure subjected to a shock load on one side of the structure. It is assumed that the structure is buried in a significant depth so that the reflections from soil surface can be ignored. The whole structure is made of reinforced concrete (RC), and the dimensions of the wall or floor under consideration are 12.8 m×26 m×1 m. Considering the convention of one-way slab, the span of the beam model is 12.8 m and the cross-sectional area is 1 m<sup>2</sup> (1 m by 1 m). The RC has a Young's modulus of 30 GPa and Poisson's ratio of 0.2 as well as density of 2500 kg/m<sup>3</sup>. To represent the one-way slab, the beam model is in a plane strain manner, in which the Young's modulus is modified as  $E/(1-\nu^2)$ , with a value of 31.25 GPa. Three typical soils in Singapore are used, namely dry sand, Kallang soil and Bukit Timah soil (Kallang soil is a kind of clay while Bukit Timah soil is a kind of residual soil, Anand

2002), whose properties are listed in Table 3.1. The explosion scenario considered is a scaled distance (stand-off distance divided by the cube root of the TNT equivalent charge weight) of  $2 \text{ m/kg}^{1/3}$  (125 kg TNT and  $R=10 \text{ m}$ ). It is assumed that the detonation is relatively distant from the structure, a reduction factor of 0.8 is used; the equivalent plane wave peak pressures in three soils are calculated from Eq. (3.13) and the reduction factor. Since the structure is assumed buried very deep in the soil, the coupling factor is taken as 1. The blast load on the buried structure is evaluated to have duration of approximately 20 ms, typical for subsurface blasts (Anand 2002). The ground shock loads in the three soils are shown in Fig. 3.6.

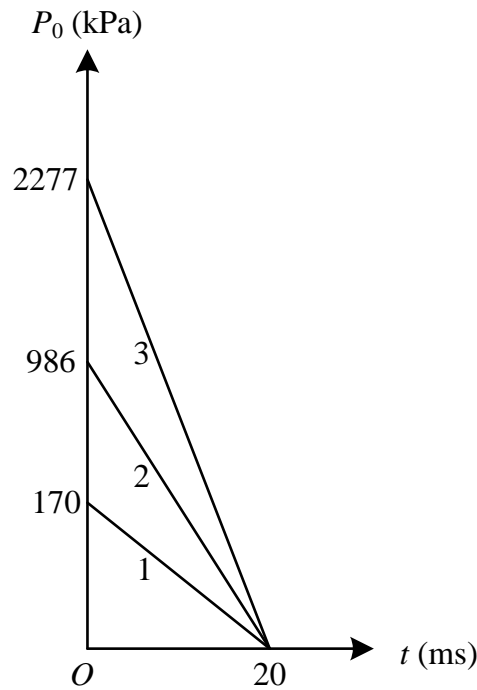


Fig. 3.6 Ground shocks in three soils (1: dry sand; 2, Kallang soil; 3: Bukit Timah soil)

Table 3.1 Properties of typical soils in Singapore

Soil type	Density (kg/m <sup>3</sup> )	Seismic velocity (m/s)	Attenuation coefficient
Dry sand	1633	305	2.75
Kallang soil	1420	1350	2.5
Bukit Timah soil	1800	1650	2.25

According to the formulation in the preceding section, the interfacial damping ratio is evaluated as follows. With the Kallang soil, the beam model is over-damped with the first three vibration modes and the interfacial damping ratios are 9.86, 2.47 and 1.10, respectively; for higher modes, the system is under-damped, with a decreasing interfacial damping ratio as 0.62, 0.39, and so on. However, in the case of dry sand, which has smaller acoustic impedance, only the first mode of the system is interfacially over-damped while other modes are interfacially under-damped. The detailed interfacial damping ratios with respect to the three typical soils are summarized in Table 3.2.

The time histories of displacements, velocities and accelerations of different points on the structural element can then be obtained following the solutions presented in the preceding section. For a conservative consideration, the mid-span response of the beam is particularly studied. As mentioned earlier, the formulae in the present study are valid when the displacement varies from zero to its maximum value, but this is considered to be sufficient for the evaluation of the critical shock environment within the structure as the response will attenuate rapidly after this time.

Table 3.2 Interfacial damping ratios of structure in typical soil

Order	In dry sand	In Kallang soil	In Bukit Timah soil
1	1.65	6.36	9.86
2	0.41	1.59	2.47
3	0.18	0.71	1.10
4	0.10	0.40	0.62
5	0.066	0.25	0.39

Fig. 3.7 shows the time histories of displacement, velocity and acceleration at the mid-span of the element under three different soil conditions, respectively. It can be observed that under such loading, structural and material conditions, the displacements achieve their maximum values in a very short time after the blast ends, whereas the velocities reach their peak values within the shock load duration. The accelerations attain their peak values instantaneously upon loading and attenuate very quickly. It is worth noting that the maximum accelerations are the most important quantities in the response since they are often used to give a criterion of the in-structure shock.

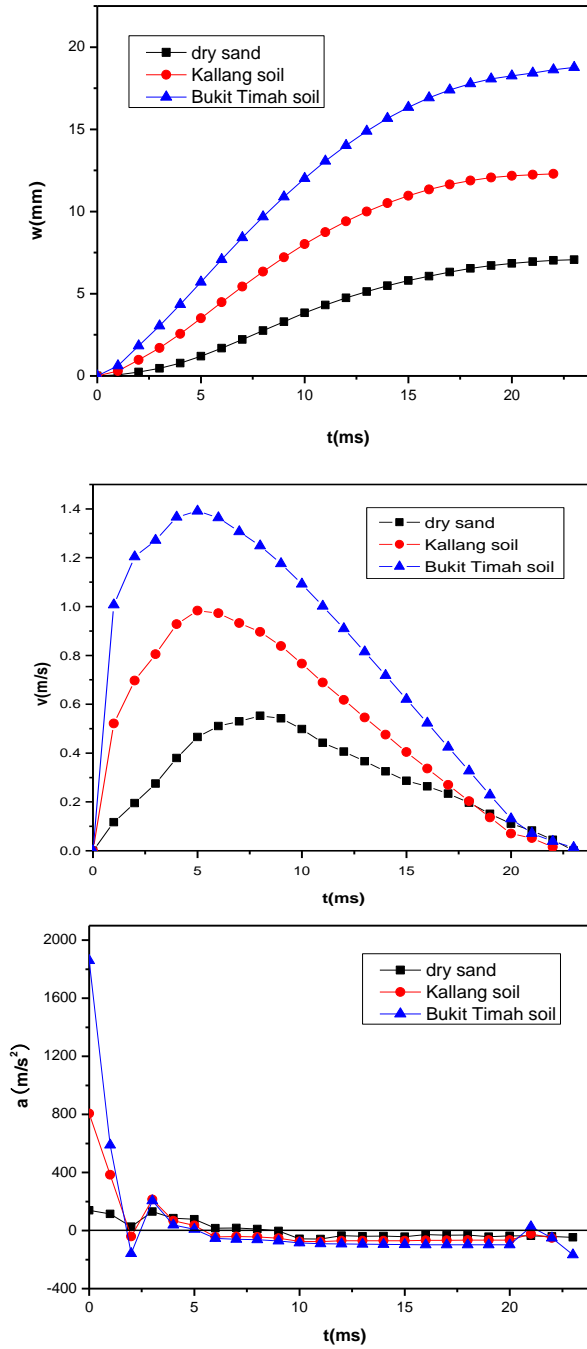


Fig. 3.7 Time histories of displacement, velocity and acceleration at mid-span of the structural member

Different soils have different acoustic impedance, thus resulting in different structural responses. In general, the maximum displacement, velocity and acceleration are higher

in soil with larger acoustic impedance than those in soil with smaller impedance. For larger soil acoustic impedance, the structural element achieves its maximum velocity sooner and its acceleration attenuates more quickly. It is of particular importance to note that, comparing to the maximum displacement and the maximum velocity, the maximum acceleration appears to be most sensitive to the soil condition. In a soil with large acoustic impedance, the maximum acceleration can be very high, and this poses the most serious threat to the equipment in the structure. Therefore, it is more desirable that an underground protective structure be constructed at a site where the soil has smaller acoustic impedance. Alternatively, it may be considered to use backfill low impedance soil to surround the buried structure for the purpose of in-structure shock mitigation.

Consider a situation in which all the conditions are the same except that the blast duration is changed to 40 ms. For comparison purpose, only Kallang soil is used. From Fig. 3.8, the mid-span displacement and velocity under 40 ms blast duration are remarkably higher than those under 20 ms blast duration, respectively. However, it is interesting to observe that the mid-span acceleration time histories under two blast durations are almost same.

Fig. 3.9 plots the relationship between the maximum responses and the scaled distance. Such plots are very useful in practical applications. All the maximum responses decrease with the scaled distance, as can be expected. However, different from the maximum displacement and velocity, the maximum acceleration decreases with the scaled distance extremely quickly in soil with larger acoustic impedance.

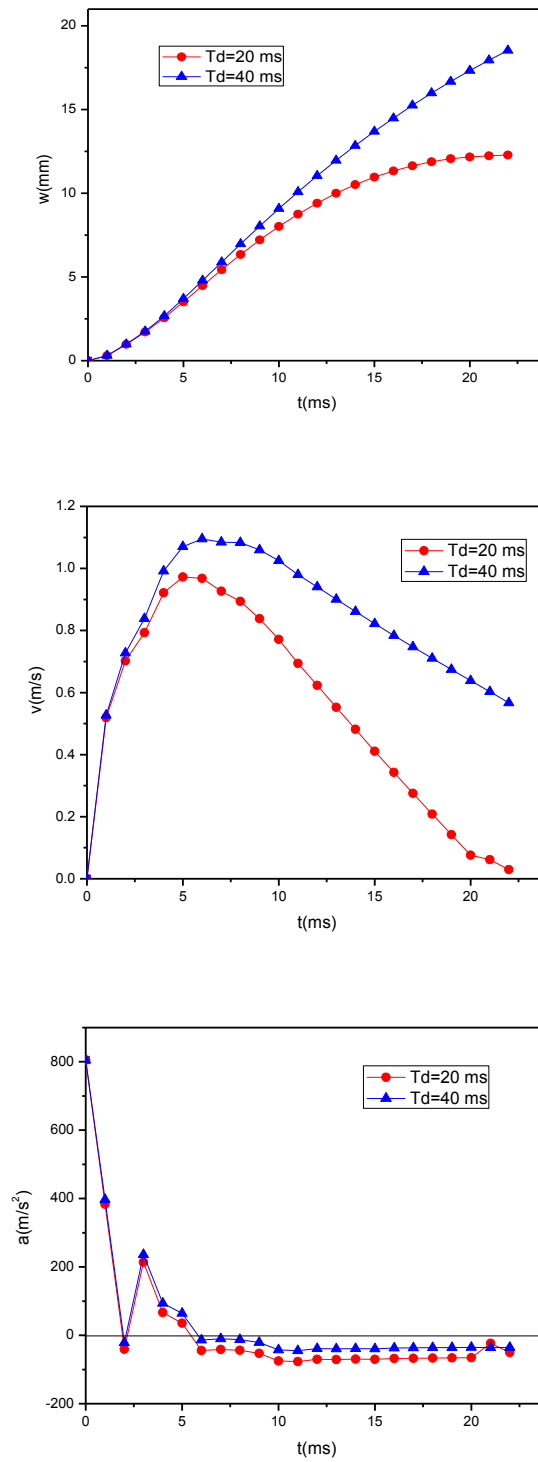


Fig. 3.8 Mid-span response comparison under different blast durations, Kallang soil



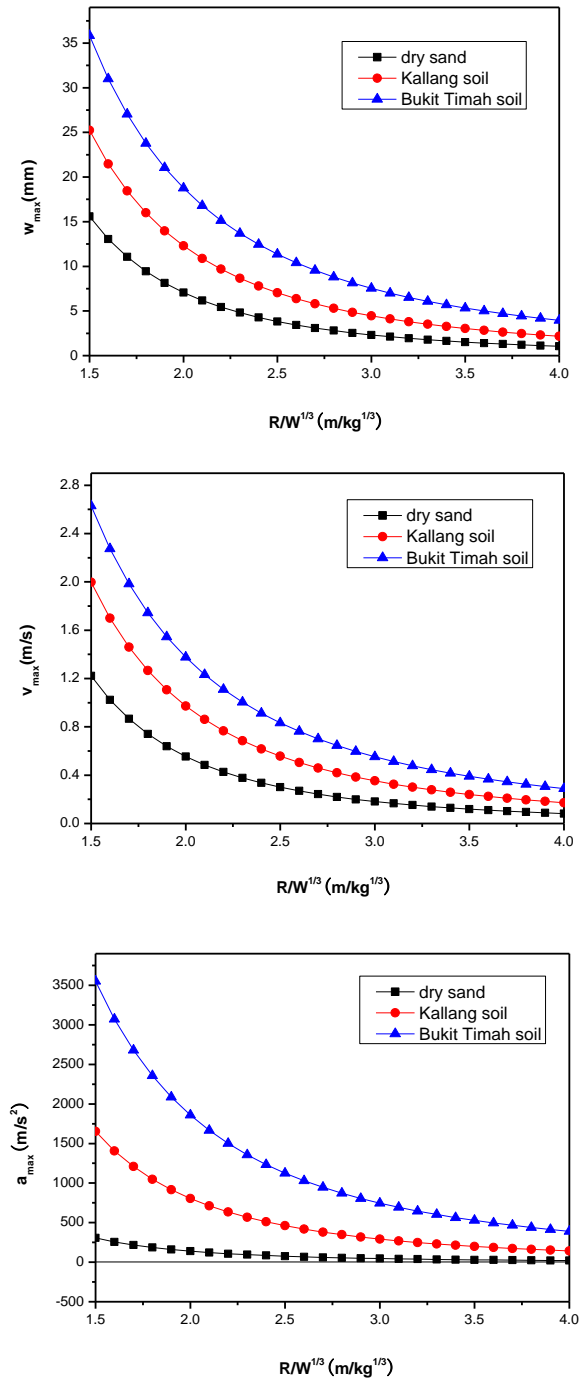


Fig. 3.9 Maximum displacement, velocity and acceleration at mid-span of the structural member

In fact, the load exerts on the structural element only when the soil particle velocity is higher than that of the structure material points. According to the assumption, the characteristic of soil particle velocity induced by the subsurface detonation is that it achieves peak value initially and then attenuates to zero in the end of the blast. For the velocity of structure, various positions have different velocity time histories; although magnitudes in different material points differ, the patterns are similar: the velocity achieves peak value quickly from initial condition at rest, then attenuates to nearly zero in the end of the pulse (in case study of a typical underground blast), as shown in Fig. 3.7. In the whole process, some central points of the structure may experience velocity larger than soil particle velocity in some instants. Therefore for these points the actual load applied on the structural element may have a few peaks due to contact and separation of the structure with the surrounding soil. However, it is assumed that throughout the shock duration, the particle velocity is larger than that of the structure (in fact, in some instants, this assumption in some points around the mid-span may not be valid), indicating there is no separation between soil and structure, which will results in a conservative prediction.

### **3.6 In-structure shock and response spectrum**

An in-structure shock model of the underground structure aims to give a comprehensive evaluation of the shock environment within the structure. When the detonation parameters are given, the shock level the equipment will experience can be predicted using such a model.

With the beam model presented, the dynamic response of a buried structure can be calculated in detail in terms of the displacement, velocity and acceleration time histories at any location on the structural element. Subsequently, the shock environment within the structure can be evaluated based on these time histories.

For an equipment unit that is attached to the structure element, the shock excitation essentially comes from the above mentioned dynamic response of the structure. Assuming the mass of the equipment is small as compared to the structural element, the influence of equipment on the structural element can be ignored. Thus the analysis of the equipment response can be uncoupled from the structural response analysis. A device mounted in the structural member is modeled as an SDOF system consisting of mass, spring and damping.

The possible effect of the in-structure shock on the equipment attached to the structure can be well represented by the shock response spectrum, which is a plot of the maximum response of SDOF oscillators subjected to the given input motions against natural frequencies of the SDOF systems, as schematically illustrated in Fig. 3.10, indicating that response spectra are constructed from SDOF systems of different frequencies subjected to the same base excitation- in fact the structural member response under subsurface blast. For the equipment response under a pulse excitation with a very short duration, the effect of damping on the maximum response is relatively insignificant and hence may be neglected (Clough and Penzien 1993).

Figure 3.11 shows the computed in-structure shock response spectra under the explosion scenario described in the preceding section, for the case where the structure is surrounded by Kallang soil. As it is customary in plotting such response spectra, the tripartite plot is employed, from which the maximum displacement, velocity and acceleration can be obtained readily when the natural frequency of the SDOF system representing the equipment is known.

The detailed procedure for establishing the shock response spectra is: first, for an SDOF system with a specific natural frequency under a specific shock (the acceleration time history is known), calculate and find the maximum velocity; next, other maximum responses are obtained by modifying the maximum velocity (maximum displacement by dividing the natural frequency while maximum acceleration by multiplying the natural frequency); finally these maximum responses are plotted in a log-scaled

tripartite paper, where the maximum displacement, maximum velocity and maximum acceleration of an SDOF system under a specific shock can be readily read in three ordinates with different directions. By comparing the spectral response values with the respective tolerance limits for a particular piece of equipment, the safety or possible damage to the equipment can be evaluated.

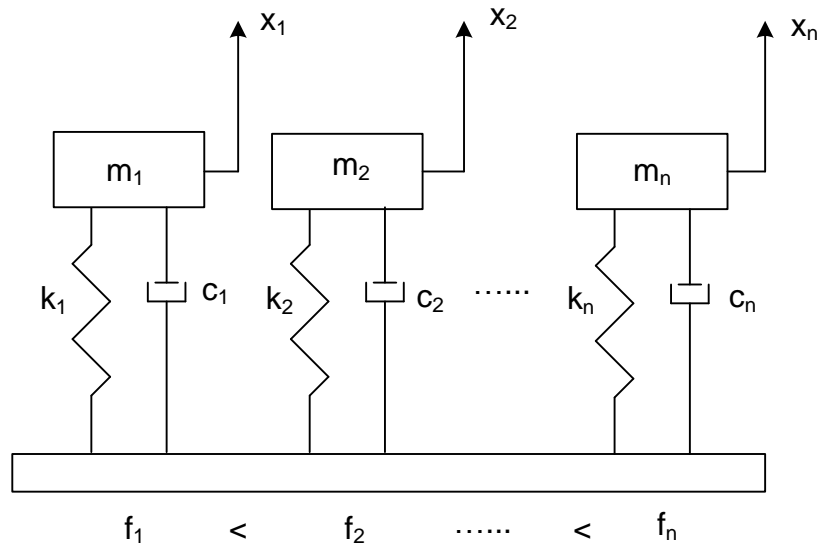


Fig. 3.10 Schematic illustration of shock response spectra

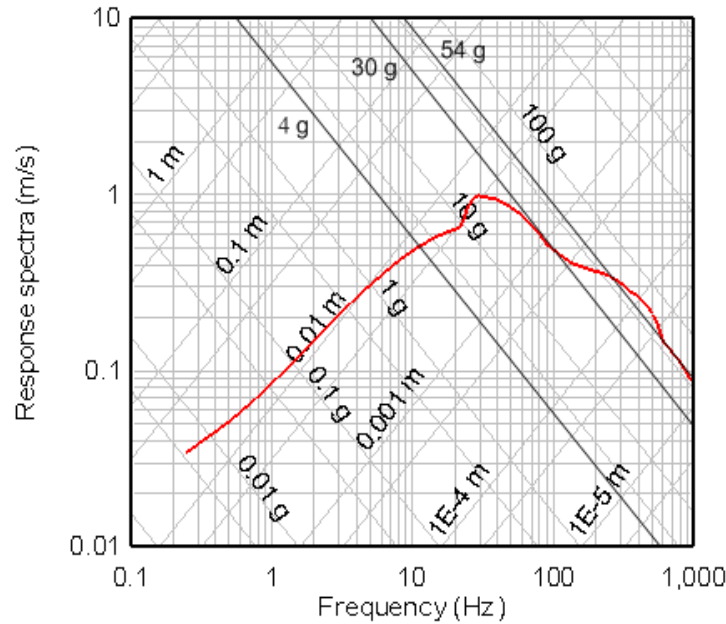
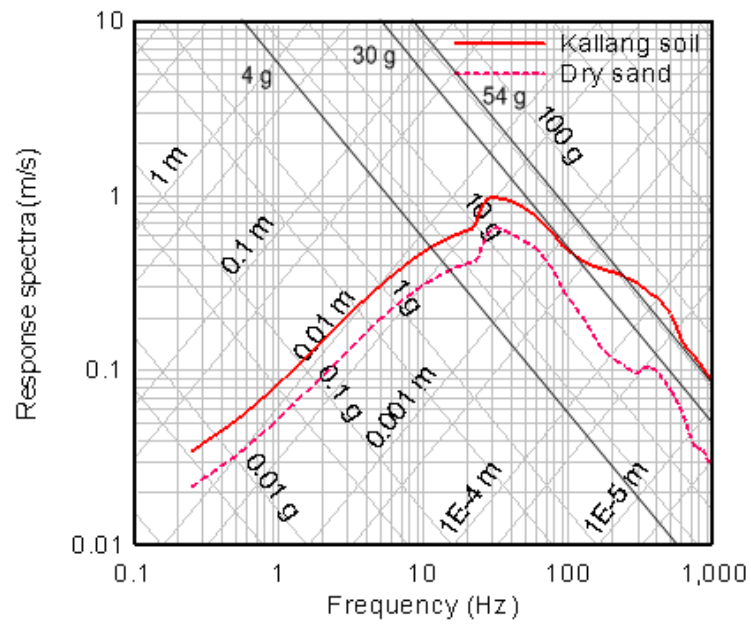
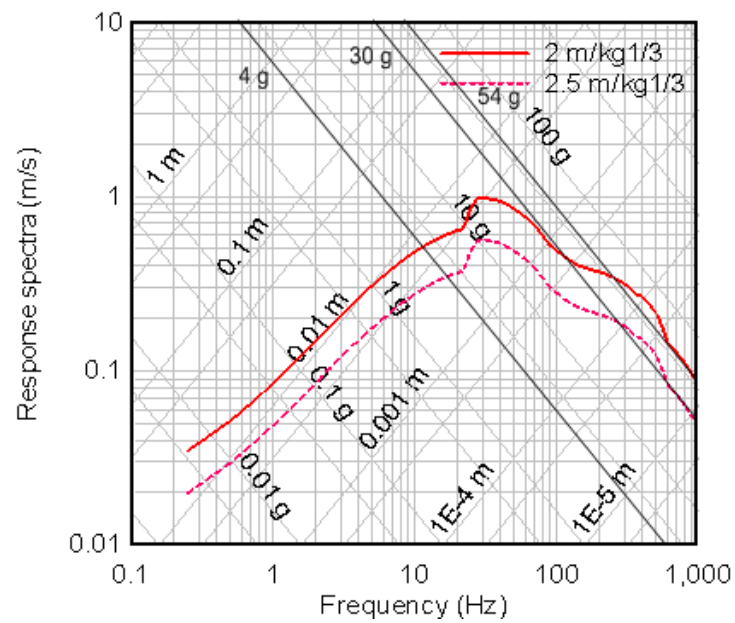


Fig. 3.11 Shock response spectra of equipment under in-structure shock with Kallang soil (vertical tolerances: 4 g- air handling units; 30 g- diesel engine generators; 54 g- computers)

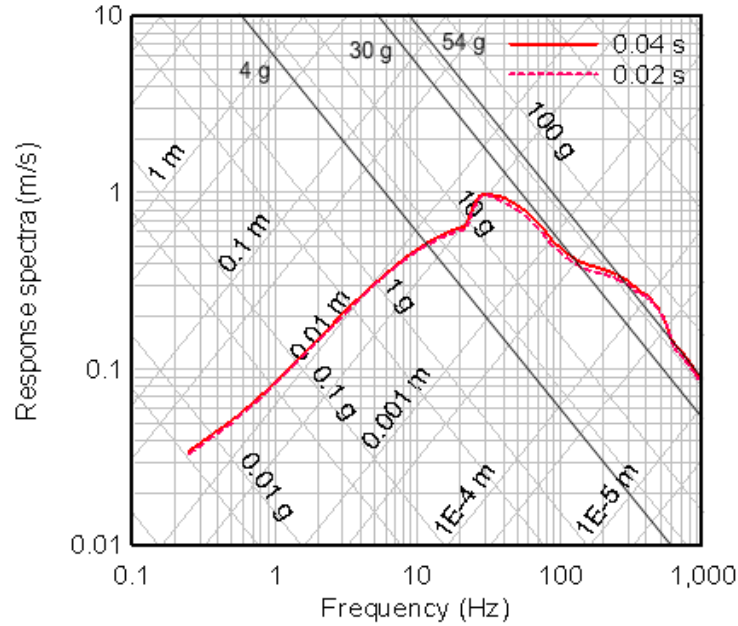
As the structural response (the beam model) is affected by the soil type, scaled distance of the explosion, and the time duration of the blast load, the shock response spectra are expected to exhibit the influence of these factors as well. Fig. 3.12 shows three pairs of the shock response spectra for a comparison. It can be observed that equipment will experience greater response when the buried structure is surrounded by soil with larger acoustic impedance (Fig. 3.12(a)). The equipment also experiences greater response under a closer detonation, as expected. Finally, under shock loads with the same peak pressure but different durations, the equipment responds almost the same since the acceleration time histories of the structural element of different blast durations, attenuating quickly within a very short duration, are almost the same due to the presence of the interfacial damping, shown in Fig. 3.8 and Fig. 3.12.



(a) Different soil



(b) Different scaled distances



(c) Different blast time durations

Fig. 3.12 Influence of various factors on the shock response spectra (vertical tolerances: 4 g- air handling units; 30 g- diesel engine generators; 54 g- computers)

Consider the dimensions of the example box structure to be 12.8 m×26 m×8 m with a wall or floor thickness of 1 m, buried in Kallang soil. The structural member of 12.8 m by 26 m is subjected to a pulse with a scaled distance of  $2 \text{ m/kg}^{1/3}$ . According to TM-5-855-1, the maximum acceleration of the whole structure would be 27 g and the maximum acceleration of the equipment would be 54 g. However, from the present analysis as described in the previous section, the maximum acceleration of the structural element is found to be 82 g at the mid-span, as shown in Fig. 3.7. Moreover, based on the shock spectrum analysis results, the spectral acceleration of an equipment piece will range from 0.01g to about 70 g, depending on its natural frequency. Clearly, because of the neglect of the structural dynamic response, TM-5-855-1 is incapable of providing a comprehensive prediction of in-structure shock and the equipment responses, and in some situations, the prediction by TM-5-855-1 may underestimate the actual responses.

Table 3.3 Equipment shock resistance

Item	Horizontal tolerance (g's)	Vertical tolerance (g's)
Air handling units	4	4
Pumps	8	10
Heat exchanger	19	11
Heat sensing devices	19	20
Control panels	24	23
Diesel engine generators	30	30
Gas turbine generators	31	4
Computers	53	54

Table 3.3 lists some typical limit values of equipment shock resistance (TM-5-855-1 1986). For an illustration, the vertical tolerance of air handling units (4 g), diesel engine generators (30 g) and computers (54 g) are plotted in Fig. 3.11 and Fig. 3.12. For example, from Fig. 11(a) one can observe that under the blast in the present case, a diesel engine generator is absolutely safe, regardless of its support condition, if the underground protective structure is buried in dry sand. It can also be inferred from the figures that for the safety of the equipment, the stiffness of the equipment support should be kept less than certain critical values, which can be deduced from the respective natural frequencies identified from these figures.

It should be pointed out that the results discussed in this and the previous sections are applicable to structures having similar characteristics as those considered in this example case study. Nevertheless, the analysis procedure can be extended to structures



with different properties, and the trends with regard to the various influence factors are expected to hold under typical buried explosion scenarios.

It is worth noting that throughout this chapter, the soil is assumed to be elastic. To make this assumption valid, the peak of the soil-transmitted blast should be not greater than the soil yield strength, i.e.,

$$\beta f(\rho_s c_s) \left( \frac{R}{W^{1/3}} \right)^{-r} \leq \sigma_{sy} \quad (3.37)$$

where  $\sigma_{sy}$  is the soil yield strength. Then if the properties of a specific soil are known, the critical scaled distance is:

$$\left. \frac{R}{W^{1/3}} \right|_{cr} = \left[ \frac{\beta f(\rho_s c_s)}{\sigma_{sy}} \right]^{\frac{1}{r}} \quad (3.38)$$

The formulations are only valid when the scaled distance is larger than the critical value in Eq. (3.38) for a specific soil.

### 3.7 Summary

To model the dynamic soil-structure interaction, an interfacial damping is introduced by the presence of the interface between the soil and the structure, characterized by geometrical configurations and material properties of the structure. With the dynamic soil-structure interaction incorporated, in-structure shock of underground structures subject to subsurface detonation is investigated theoretically using a beam model. Based on the time histories of the structural response, the shock response spectra are subsequently constructed, and these shock response spectra provide an effective means for the assessment of the working condition of the equipment mounted on the structural member. Representative analysis results indicate that the maximum displacement, velocity and acceleration responses are higher when the structure are surrounded by

soil with larger acoustic impedance, and this subsequently results in greater equipment shock level. In particular, the maximum acceleration of the structural element increases with the soil acoustic impedance dramatically. Therefore, for acceleration sensitive equipment, the protective structures should be constructed in a site with small impedance and the equipment should be placed near corners within the structure. Most significantly, the present study establishes a method to predict in-structure shock of underground structures in a systematic and effective way. Factors missing in the crude prediction in TM-5-855-1 such as properties of surrounding soil, the particulars of the underground structure, soil-structure interaction and structural response are considered. Further, the information of equipment and the excitation time history are also incorporated to give predictions for specific devices with different natural frequencies.

## **4 IN-STRUCTURE SHOCK ASSESSMENT OF UNDERGROUND STRUCTURES WITH CONSIDERATION OF RIGID BODY MOTION**

When subjected to a subsurface detonation, in general, an underground structure undergoes two kinds of motions, i.e., the rigid body motion (RBM) of the whole structure and local response of the structural element. To the author's knowledge, continuous model for underground structural response induced by a subsurface explosion with consideration of RBM has not been analytically established.

To assess the shock level within the underground structure more accurately, an analytical model consisting of the RBM and local deflection is presented in this study. Due to the relative large distance between the detonation and the structure in which case no significant damage occurs, the effect of soil flow change on structural loads may be negligible (Baylot 2000). In the current model, the responses of the structural element are obtained in consideration of both the soil-structure interaction (SSI) and the RBM effects. The derived structural response then acts as the excitation for the equipment internally mounted on the structure. The response of the equipment thus can be obtained and compared with the specified tolerance to check its safety. The present study mainly focuses on the derivation of the structural responses by combining the global RBM and the local element response, in which an interfacial damping is introduced to reflect the SSI.

### **4.1 Methodology**

When subjected to a soil-transmitted blast load, the underground structure undergoes RBM as well as deflection simultaneously. It is difficult, or sometimes even impossible, to obtain both the RBM and the deflection at the same time analytically. In the present

chapter, to determine the gross response of certain structural element, the displacement of the structural element is decoupled into two parts: one from RBM and the other from the pure deflection. Based on this decoupling, the lower and upper bounds of the structural element are obtained. Consider two extreme cases:

(a) Without RBM, the load applied totally contributes to the deformation of the structural element and only causes the response of a structural member.

(b) Without deflection, the load applied totally contributes to the RBM and only causes RBM response.

It is obvious that the response (for instance, displacement, velocity and acceleration) of case (a) is significantly greater than that of case (b) for a typical underground structure subjected to a subsurface detonation. Case study calculation results in the following section will confirm this.

#### ***The lower bound***

In deriving the RBM response, the structure is assumed rigid and undergoes pure translation. Obviously, the assumption of rigid structure will lead to an over-prediction of the RBM response. Subsequently, with over-prediction of the RBM, the load allocated to cause pure deflection of the structural element is under-estimated.

The real situation is the soil-transmitted blast load contributes to both the RBM and the deflection simultaneously. The overly-predicted RBM and the under-estimated deformation will result in gross responses lower than those in the real situation. It is not conservative and can be considered as the lower bound of the gross response of the structural element.

#### ***The upper bound***

Furthermore, the upper bound of the gross response is determined by assuming no RBM and the structural element only undergoes pure deflection.

With no doubt, the response of the structural element in real situation is in between of these upper and lower bounds. In a typical in-structure shock problem, the upper and lower bounds responses are close to each other thus the real response is approximately found. In the present study, the method is formulated analytically in detail and validated in a case study.

## **4.2 Rigid body motion of the whole structure**

Conservatively, the most adverse situation is analyzed where the nearest point to the subsurface detonation is the center of certain structural element. If the underground explosion occurs in a location where the nearest point from the structure to the detonation is a corner, the problem is further complicated. In this situation, generally, the RBM of the assumed rigid structure will be a combination of translation and rotation, rather than pure translation, which is out of the scope of the current study.

For a box-type underground structure subjected to a blast load induced, generally, there are several loading phases for the RBM, loading only on the nearest structural element, loading on both nearest and farthest structural elements, loading only on the farthest element and the phase in which only the soil resistance exists on the farthest element. For a typical detonation case, the most important phase is the first one, in which the maximum acceleration and velocity of the entire structure always occur. Therefore only the first loading phase is considered (Weidlinger and Hinman 1988, 1991; Alwis and Lam 1994). As stated in the methodology, when analyzing the RBM, the structural deflection is ignored thus the structure is assumed as a rigid body. The friction between the side walls and the surrounding soil is negligible compared to the blast load thus it is ignored. In addition, among the resistances from the back side of the structure, only the major part induced by the velocity difference between the structure and the surrounding soil is considered (Weidlinger and Hinman 1988, 1991; Alwis and Lam 1994).

Taking the SSI into consideration, with the free body diagram in Fig. 4.1, we have:

$$M \frac{d^2 U(t)}{dt^2} = A \left\{ \left[ \sigma_{f,N} + \rho_s c_s \left( V_N - \frac{dU(t)}{dt} \right) \right] - \rho_s c_s \frac{dU(t)}{dt} \right\} \quad (4.1)$$

where  $M$  = mass of the whole structure;  $A$  = area of a structural element subjected to a blast load;  $\sigma_{f,N}$  and  $V_N$  = free field pressure and soil particle velocity at the nearest structural element, respectively; and  $U(t)$  = RBM displacement of the structure. In consideration of  $\sigma_{f,N} = \rho_s c_s V_N$ , Eq. (4.1) becomes

$$\tau_0 \frac{d^2 U(t)}{dt^2} + \frac{dU(t)}{dt} = \frac{P_0 \alpha}{\rho_s c_s} \left( 1 - \frac{t}{T_d} \right) \quad (4.2)$$

where  $\tau_0 = M / (2A\rho_s c_s)$  is defined as the characteristic response time.

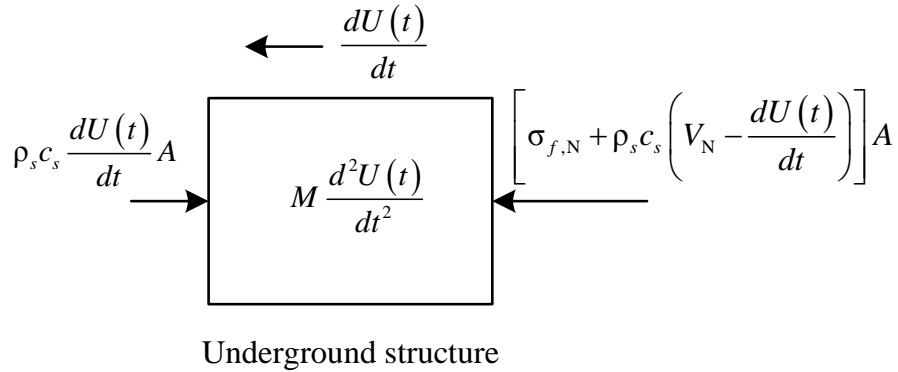


Fig. 4.1 Free body diagram of the underground structure (assumed rigid)

With a stationary initial condition with zero displacement and zero velocity assumed for the structure, the time histories of the RBM which do not consider the structural deflection can be derived as:

$$U(t) = \frac{P_0 \alpha}{\rho_s c_s} \left[ \left( 1 + \frac{\tau_0}{T_d} \right) t - \frac{t^2}{2T_d} + \frac{\tau_0}{T_d} (\tau_0 + T_d) (e^{-t/\tau_0} - 1) \right] \quad (4.3a)$$

$$\dot{U}(t) = \frac{P_0 \alpha}{\rho_s c_s} \left[ \left( 1 + \frac{\tau_0}{T_d} \right) - \frac{t}{T_d} - \left( 1 + \frac{\tau_0}{T_d} \right) e^{-t/\tau_0} \right] \quad (4.3b)$$

$$\ddot{U}(t) = -\frac{P_0 \alpha}{\rho_s c_s} \left[ \frac{1}{T_d} - \left( \frac{1}{\tau_0} + \frac{1}{T_d} \right) e^{-t/\tau_0} \right] \quad (4.3c)$$

It is worth noting that the derived RBM response is obviously greater than that in the real situation by assuming no deflection, ignoring the side friction and some resistance from the back side.

## 4.3 Structural element response to shock load

### 4.3.1 Kirchhoff plate model

For a typical box-type underground structure, each of the structural elements is considered as a Kirchhoff plate in consideration that the thickness-to-span and the maximum-deflection-to-thickness ratios are, in any time, both smaller than 1/5, in which the Kirchhoff-Love plate theory can be applied. In a real structure, each plate of the buried structure is neither fixed nor simply supported to other structural elements. For a safer consideration, the plate is assumed to be simply supported in the current analysis.

In the present study, in-structure shock rather than damage is of major concern. Therefore it is reasonable to assume that the structural response is within the elastic limit. According to Baylot and Hall (1995), in a small scale experiment, when the distance between the detonation and the structure is relatively large, the structure experiences a shock and the structural element deforms elastically without major damage. The governing equation for a plate subjected to dynamic load is:

$$D\nabla^4 w(x, y, t) + \rho h \frac{\partial^2 w(x, y, t)}{\partial t^2} = P(x, y, t) \quad (4.4)$$

In view of the SSI in Section 3.1, the governing equation can be rewritten as:

$$D\nabla^4 w(x, y, t) + \rho h \frac{\partial^2 w(x, y, t)}{\partial t^2} + \rho_s c_s \frac{\partial w(x, y, t)}{\partial t} = 2P_0 \alpha \left( 1 - \frac{t}{T_d} \right) \quad (4.5)$$

where  $D = Eh^3 / [12(1 - \nu^2)]$  is the flexural rigidity of the plate;  $\rho$  and  $h$  = density and thickness of the plate, respectively. Assume the displacement of the structural element as:

$$w(x, y, t) = U(t) + \sum_{m=1}^{\infty} \sum_{n=1}^{\infty} W_{mn}(x, y) \eta_{mn}(t) \quad (4.6)$$

recall that  $U(t)$  = RBM displacement;  $W_{mn}(x, y)$  =  $m, n$ th mode shape, in which  $m, n$  denote the order of the vibration in two orthogonal directions; and  $\eta_{mn}(t)$  = generalized coordinate in the generalized space, or modal space. Since the RBM in fact is the zeroth order of the vibration mode and does not affect the deflection of the structural element, through analyzing the specific mode, with the simply supported boundary condition, the  $m, n$ th mode can be expressed as

$$W_{mn}(x, y) = \frac{2}{\sqrt{\rho h a b}} \sin \frac{m\pi x}{a} \sin \frac{n\pi y}{b} \quad (4.7)$$

where  $a$  and  $b$  are in-plane dimensions of the plate, respectively.

Substituting Eq. (4.6) into Eq. (4.5), and rewrite the governing equation:

$$\begin{aligned} & \rho h \sum_{m=1}^{\infty} \sum_{n=1}^{\infty} W_{mn}(x, y) \ddot{\eta}_{mn}(t) + \rho_s c_s \sum_{m=1}^{\infty} \sum_{n=1}^{\infty} W_{mn}(x, y) \dot{\eta}_{mn}(t) + \\ & D \sum_{m=1}^{\infty} \sum_{n=1}^{\infty} \pi^4 \left[ \left( \frac{m}{a} \right)^2 + \left( \frac{n}{b} \right)^2 \right]^2 W_{mn}(x, y) \eta_{mn}(t) = 2\sigma_f(t) - \rho h \ddot{U}(t) - \rho_s c_s \dot{U}(t) \end{aligned} \quad (4.8)$$

According to the orthogonality condition of the normal modes, the governing equation for the  $m, n$ th mode is



$$\ddot{\eta}_{mn}(t) + \frac{\rho_s c_s}{\rho h} \dot{\eta}_{mn}(t) + \pi^4 \frac{D}{\rho h} \left[ \left( \frac{m}{a} \right)^2 + \left( \frac{n}{b} \right)^2 \right]^2 \eta_{mn}(t) = F_{mn}(t) \quad (4.9)$$

$$F_{mn}(t) = [1 - (-1)^m][1 - (-1)^n] \frac{2}{mn\pi^2} \sqrt{\frac{ab}{\rho h}} [2\sigma_f(t) - \rho h \ddot{U}(t) - \rho_s c_s \dot{U}(t)]$$

To demonstrate the effect of the SSI, the  $m, n$ th interfacial damping ratio is defined as

$$\zeta_{mn} = \frac{\frac{\rho_s c_s}{\rho h}}{2\omega_{mn}} = \frac{\frac{\rho_s c_s}{\rho h}}{2\pi^2 \sqrt{\frac{D}{\rho h} \left[ \left( \frac{m}{a} \right)^2 + \left( \frac{n}{b} \right)^2 \right]}} \quad (4.10)$$

where  $\omega_{mn} = m, n$ th natural frequency of the plate. The interfacial damping ratio, induced by the presence of the interface between the structure and the surrounding soil, delineates the SSI by incorporating nearly all the properties from both the structure and the soil, inclusive of the acoustic impedance of the soil, the in-plane dimensions, mode order numbers, density, thickness and flexural rigidity of the structural element. From the expression, one can know that the interfacial damping ratio decreases with the increase of orders in two directions, which means the damping ratios are greater for lower modes and smaller for higher modes. The same structure buried in different soils have different interfacial damping ratios. For a typical protective structure in certain kinds of soils, the first or first several modes of the structural element may be interfacially over-damped while the higher modes under-damped. The corresponding structural responses are derived as follows.

#### 4.3.2 Case I: $\zeta_{mn} \geq 1$

Assume the arrival time of the blast wave as the time origin. At time zero, both the displacement and the velocity are zero no matter in the physical space or the generalized space. Combining the governing equation and the initial conditions, for an

interfacial damping ratio larger than 1, the local structural responses are obtained, e.g. the m, nth order contribution to the deflection is

$$w_{mn}(x, y, t) = \frac{2}{\sqrt{\rho h a b}} \sin \frac{m\pi x}{a} \sin \frac{n\pi y}{b} \left\{ E_{mn} e^{D_{mn,3}t} + F_{mn} e^{D_{mn,4}t} + Q_{mn} \left[ D_{mn,1} (D_{mn,5} - \omega_{mn}t) + \tau_0 D_{mn,2} e^{-t/\tau_0} \right] \right\} \quad (4.11)$$

where

$$E_{mn} = - \frac{Q_{mn} (\omega_{mn} D_{mn,1} + D_{mn,2} + D_{mn,1} D_{mn,4} D_{mn,5} + \tau_0 D_{mn,2} D_{mn,4})}{D_{mn,4} - D_{mn,3}}$$

$$F_{mn} = \frac{Q_{mn} (\omega_{mn} D_{mn,1} + D_{mn,2} + D_{mn,1} D_{mn,3} D_{mn,5} + \tau_0 D_{mn,2} D_{mn,3})}{D_{mn,4} - D_{mn,3}}$$

$$Q_{mn} = [1 - (-1)^m][1 - (-1)^n] \frac{2}{mn\pi^2} \sqrt{\frac{ab}{\rho h}}$$

$$D_{mn,1} = \frac{P_0 \alpha}{\omega_{mn}^3 T_d}$$

$$D_{mn,2} = \frac{\tau_0 P_0 \alpha}{\omega_{mn}^2 \tau_0^2 - 2\zeta_{mn} \omega_{mn} \tau_0 + 1} \left[ \left( 1 + \frac{\tau_0}{T_d} \right) - \frac{1}{2\zeta_{mn} \omega_{mn}} \left( \frac{1}{\tau_0} + \frac{1}{T_d} \right) \right]$$

$$D_{mn,3} = \left( -\zeta_{mn} + \sqrt{\zeta_{mn}^2 - 1} \right) \omega_{mn}$$

$$D_{mn,4} = \left( -\zeta_{mn} - \sqrt{\zeta_{mn}^2 - 1} \right) \omega_{mn}$$

$$D_{mn,5} = \omega_{mn} (T_d - \tau_0) + \left( 2\zeta_{mn} + \frac{1}{2\zeta_{mn}} \right)$$

the velocity contributed by m, nth mode is

$$\dot{w}_{mn}(x, y, t) = \frac{2}{\sqrt{\rho h a b}} \sin \frac{m\pi x}{a} \sin \frac{n\pi y}{b} \begin{bmatrix} E_{mn} D_{mn,3} e^{D_{mn,3}t} + F_{mn} D_{mn,4} e^{D_{mn,4}t} \\ -Q_{mn} (\omega_{mn} D_{mn,1} + D_{mn,2} e^{-t/\tau_0}) \end{bmatrix} \quad (4.12)$$

and the corresponding acceleration is

$$\ddot{w}_{mn}(x, y, t) = \frac{2}{\sqrt{\rho h a b}} \sin \frac{m\pi x}{a} \sin \frac{n\pi y}{b} \left( E_{mn} D_{mn,3}^2 e^{D_{mn,3}t} + F_{mn} D_{mn,4}^2 e^{D_{mn,4}t} + \frac{Q_{mn}}{\tau_0} D_{mn,2} e^{-t/\tau_0} \right) \quad (4.13)$$

The aforementioned solutions are valid only in blast loading phase in which the structural element deforms to the maximum deflection.

### 4.3.3 Case II: $\zeta_{mn} < 1$

When the interfacial damping ratio is smaller than 1, with the same method, the  $m$ ,  $n$ th order contribution to the displacement is

$$w_{mn}(x, y, t) = \frac{2}{\sqrt{\rho h a b}} \sin \frac{m\pi x}{a} \sin \frac{n\pi y}{b} \left\{ e^{-\zeta_{mn} \omega_{mn} t} \left[ E_{mn} \sin D_{mn,6} t + F_{mn} \cos D_{mn,6} t \right] + Q_{mn} \left[ D_{mn,1} (D_{mn,5} - \omega_{mn} t) + \tau_0 D_{mn,2} e^{-t/\tau_0} \right] \right\} \quad (4.14)$$

where

$$E_{mn} = -\frac{Q_{mn} [\zeta_{mn} \omega_{mn} (D_{mn,1} D_{mn,5} + \tau_0 D_{mn,2}) - \omega_{mn} D_{mn,1} - D_{mn,2}]}{\sqrt{1 - \zeta_{mn}^2} \omega_{mn}}$$

$$F_{mn} = -Q_{mn} (D_{mn,1} D_{mn,5} + \tau_0 D_{mn,2})$$

$$D_{mn,6} = \sqrt{1 - \zeta_{mn}^2} \omega_{mn}$$

$D_{mn,i} (i = 1, 2, 5) = \text{same as defined in the previous section.}$

the velocity contribution of the  $m, n$ th mode is

$$\dot{w}_{mn}(x, y, t) = \frac{2}{\sqrt{\rho h a b}} \sin \frac{m\pi x}{a} \sin \frac{n\pi y}{b} \left\{ -e^{-\zeta_{mn}\omega_{mn}t} \left[ \begin{aligned} &(\zeta_{mn}\omega_{mn}E_{mn} + D_{mn,6}F_{mn})\sin D_{mn,6}t \\ &+ (\zeta_{mn}\omega_{mn}F_{mn} - D_{mn,6}E_{mn})\cos D_{mn,6}t \end{aligned} \right] - Q_{mn}(\omega_{mn}D_{mn,1} + D_{mn,2}e^{-t/\tau_0}) \right\} \quad (4.15)$$

and the corresponding acceleration is

$$\ddot{w}_{mn}(x, y, t) = \frac{2}{\sqrt{\rho h a b}} \sin \frac{m\pi x}{a} \sin \frac{n\pi y}{b} \left\{ e^{-\zeta_{mn}\omega_{mn}t} \left[ \begin{aligned} &(\zeta_{mn}^2\omega_{mn}^2E_{mn} + 2\zeta_{mn}\omega_{mn}D_{mn,6}F_{mn} - D_{mn,6}^2E_{mn})\sin D_{mn,6}t \\ &+ (\zeta_{mn}^2\omega_{mn}^2F_{mn} - 2\zeta_{mn}\omega_{mn}D_{mn,6}E_{mn} - D_{mn,6}^2F_{mn})\cos D_{mn,6}t \end{aligned} \right] + \frac{Q_{mn}}{\tau_0} D_{mn,2}e^{-t/\tau_0} \right\} \quad (4.16)$$

Again the results above are valid only in the time intersection of the blast duration and time period ranging from zero to maximum deflection.

In practical engineering, it stands very rare chance to have an interfacial damping ratio exactly equal to 1. However, if it happens, for mathematical derivation convenience and the physical nature, it can be considered as an interfacially over-damped case.

#### 4.3.4 Gross response in the blast duration: the lower bound

The gross response of the structural element consisting of the RBM and pure deflection is of concern and is also the response lower bound when considering both the RBM and

the deflection simultaneously. The response contribution by the pure deflection, underestimated, is derived above.

When analyzing the RBM by assuming no deflection, the pure RBM responses are overly-predicted thus when analyzing the RBM and the deflection simultaneously, the force allocated for the RBM part  $\rho h \ddot{U}(t) + \rho_s c_s \dot{U}(t)$  (see right hand side of the Eq. (4.8)) is also overly-predicted compared to that of the real situation. Subsequently the RBM contribution to the gross response of the structural element is higher than that in the real situation.

In fact, the RBM response of the whole structure in Case (a), where all the applied load contributes to the RBM, should be significantly higher than the real RBM of the whole structure since in the real situation, the structural member undergoes both the RBM of whole structural and local flexural response simultaneously. However, the substantially over-predicted RBM response of Case (a) can be used to estimate the RBM response when the flexural response of structural member is also considered. Within the blast duration, the total load is twice the free-field pressure time history and the right-hand side of Eq. (4.8) is the load part causing pure flexural response of structural member. Then, the remaining part  $\rho h \ddot{U}(t) + \rho_s c_s \dot{U}(t)$  is the load part for RBM response when both RBM and flexure response are considered. With  $\rho h \ddot{U}(t) + \rho_s c_s \dot{U}(t)$  as load for RBM, the RBM velocity and acceleration time histories when considering RBM and deflection simultaneously are obtained:

$$\dot{U}_m(t) = \frac{P_0 \alpha}{\rho_s c_s} \left\{ e^{-\frac{t}{\tau_0}} \left[ \left( \frac{2h}{h_e} - 1 \right) \left( \frac{1}{\tau_0} + \frac{1}{T_d} \right) t - 1 - \frac{2\tau_0}{T_d} \left( 1 - \frac{h}{h_e} \right) \right] + 1 - \frac{t}{T_d} + \frac{2\tau_0}{T_d} \left( 1 - \frac{h}{h_e} \right) \right\} \quad (4.17a)$$

$$\ddot{U}_m(t) = \frac{P_0 \alpha}{\rho_s c_s} \left\{ \frac{e^{-\frac{t}{\tau_0}}}{\tau_0} \left[ - \left( \frac{2h}{h_e} - 1 \right) \left( \frac{1}{\tau_0} + \frac{1}{T_d} \right) t + \frac{2h}{h_e} + \frac{\tau_0}{T_d} \right] - \frac{1}{T_d} \right\} \quad (4.17b)$$

where  $h_e = M / (\rho A)$  represents the effective thickness of the whole structure.

The following equations are the pure deflection, gross velocity and gross acceleration time histories of the structural element while considering RBM and the deformation simultaneously:

$$w_d(x, y, t) = \sum_{m=1}^{\infty} \sum_{n=1}^{\infty} W_{mn}(x, y) \eta_{mn}(t) \quad (4.18a)$$

$$\dot{w}(x, y, t) = \dot{U}_m(t) + \sum_{m=1}^{\infty} \sum_{n=1}^{\infty} W_{mn}(x, y) \dot{\eta}_{mn}(t) \quad (4.18b)$$

$$\ddot{w}(x, y, t) = \ddot{U}_m(t) + \sum_{m=1}^{\infty} \sum_{n=1}^{\infty} W_{mn}(x, y) \ddot{\eta}_{mn}(t) \quad (4.18c)$$

Amongst, pure deflection, Eq. 4.18(a), rather than the gross displacement, is of interest since only the pure deflection has contribution to the stress distribution in the structure element while the RBM displacement part has no contribution. For a typical in-structure shock problem, structural failure is not the major concern due to the thick wall and the relatively distant explosion location. The gross acceleration time history, Eq. 4.18(c), consisting of the contributions both from the RBM and the pure deflection, is of most significance since it is the direct excitation for the inside device attached to the structural element and related to the force developed within the equipment and directly determine its safety.

The response after the blast duration can be calculated with the application of the terminal conditions of the blast duration phase as initial conditions. In fact, for a typical problem of in-structure shock of underground structure subjected to a subsurface detonation, the response time histories in the blast duration will suffice since the acceleration response used to excite the device achieves peak value initially and decays at a high rate, making the major shock in the initial stage of the blast duration.

Theoretically, the exact responses are achieved by combining all the contributions of modes from first order to infinity. In fact, higher order modes generally make trivial contribution therefore finite modes are used to approximately represent the exact response. The number of modes needed depends on the physical nature of the problem (for dynamic problem with short load duration, more modes are needed) as well as the result accuracy desired. Generally, for a problem of an underground structure with typical geometrical configuration subjected to a typical subsurface-detonation induced blast, 20-30 modes in each direction are sufficient.

Until now, the lower bound responses of a structural element are derived. Further, the upper bound responses are calculated by assuming no RBM. Then the real responses can be approximately found.

#### **4.4 A case study and discussions**

Consider a box-shaped underground structure subjected to a subsurface detonation loading on one of its structural element, made of reinforced concrete with the Young's modulus of 30 GPa, the Poisson's ratio of 0.2, and the density of 2500 kg/m<sup>3</sup>. The length, width, and height of the structure are assumed to be 12.8 m, 14 m, and 8 m, respectively. All the structural elements have the uniform thickness of 1 m. The surrounding soils are dry sand and two typical soils in Singapore, i.e. Kallang soil and Bukit Timah soil (Anand 2007), respectively. Amongst, Bukit Timah soil has the largest acoustic impedance and the smallest attenuation factor while the dry sand has the smallest acoustic impedance and the largest attenuation factor. The scaled distance, defined as the standoff distance divided by the cubic root of the TNT equivalent weight, is 2 m/kg<sup>1/3</sup> ( $R=10$  m,  $W=125$  kg). The shock load duration is 20 ms. All of the parameters used are typical for an underground detonation. First 30 modes in each direction are used to approximate the exact responses and the results converge without any "visible" oscillation.

Obviously, for a scenario that the detonation lies in the extended line through two opposite structural element centers, shown in Fig. 4.2, the center of the nearest plate to the detonation is the most dangerous point and needs special inspections.

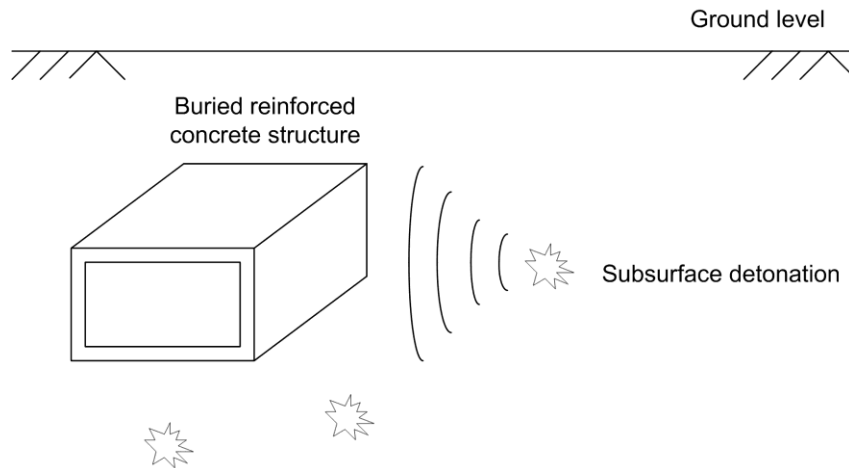
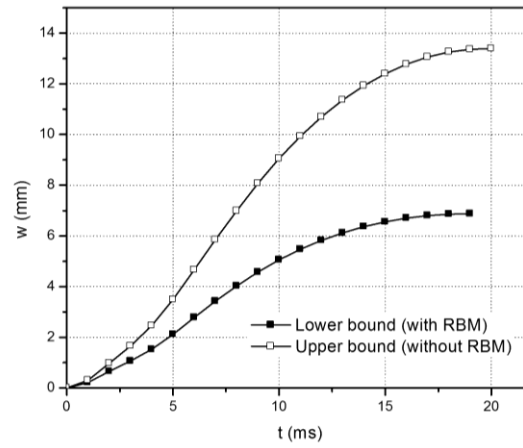


Fig. 4.2 Underground structure subjected to subsurface detonations

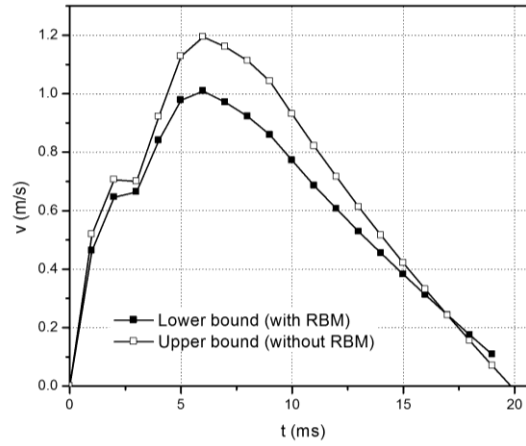
Figure 4.2 gives the upper and lower bounds of structural element center pure deflection, gross velocity and gross acceleration surrounded by Kallang soil. The bounds of pure deflection of the element center are far from each other thus it is difficult to approximate the real deflection. As stated previously, deflection is not the major concern for in-structure shock problem due to the thick structure wall and relatively distant standoff. In this case, the maximum deflection is smaller than 14 mm, compared to the 1 m thickness, the deformation is elastic. Amongst, for acceleration time history, the two bounds are close and the real acceleration can be readily approximated.

In engineering practice, the relationship between the maximum response and the scaled distance is concerned. Figure 4.3 indicates the maximum deflection excluding the RBM decreases with the increase of the scaled distance, so do the maximum gross velocity and acceleration. It is desirable to know the upper and lower bounds of maximum acceleration are close to each other. One can read the approximate peak acceleration of the structural element for specific scaled distance readily.

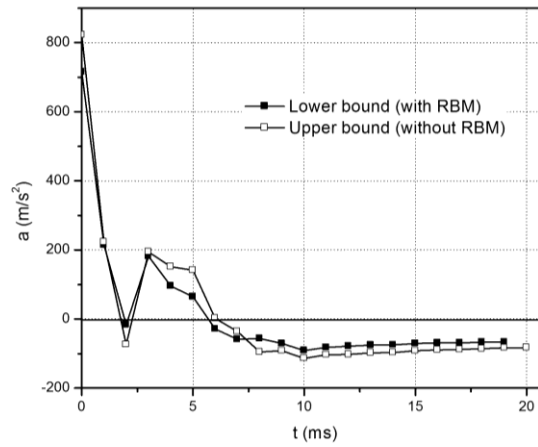




(a)

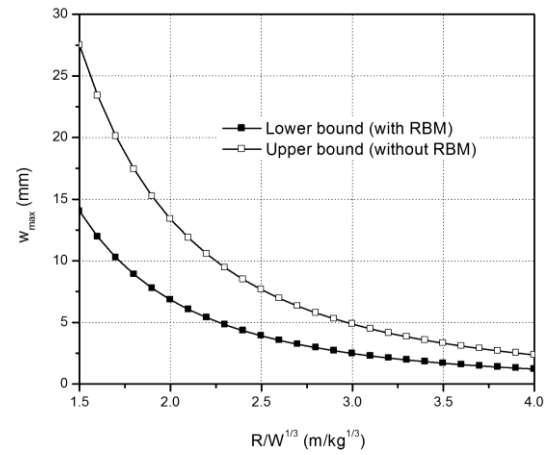


(b)

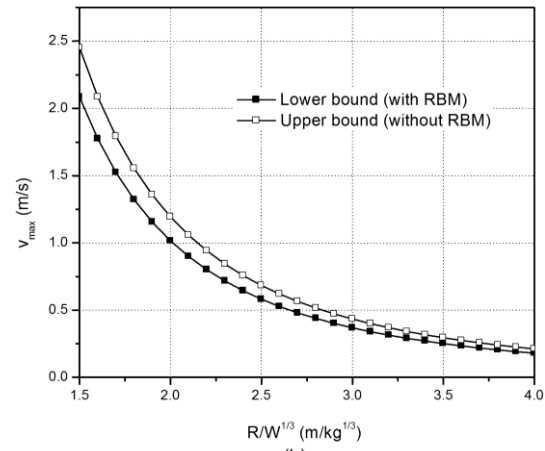


(c)

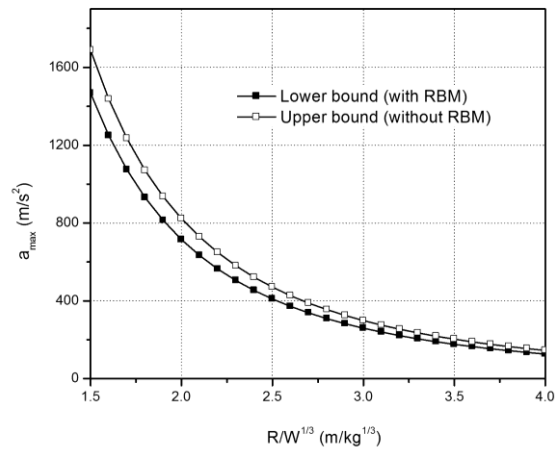
Fig. 4.3 Time histories of upper and lower bounds of (a) deformation; (b) gross velocity; and (c) gross acceleration at the structural element center, Kallang soil



(a)



(b)



(c)

Fig. 4.4 Upper and lower bounds of (a) maximum deformation; (b) gross velocity; and (c) gross acceleration at the structural element center versus scaled distance, Kallang soil

Recall that in deriving the RBM response, the friction between the side walls and surrounding soil and some resistances from the back side are neglected. From the results above, the ignored items are not significant compared to the considered ones. The reason is if the effects of the ignored items are significant and incorporated into the calculation, the lower bound response will become remarkably higher, much closer to the upper bound. However, the upper and lower bounds are already sufficiently close to each other and there is not much room for the lower bound to become higher (for instance, of most significance, consider the gross acceleration of the structural element).

To validate the method used in the present study, the structural dimension along the direction parallel to the blast load is increased to a large value thus the mass of the structure is large. Figure 4.4 indicates that the lowered bounds of the responses including maximum deflection, maximum gross velocity and maximum gross acceleration are very close to, and even coincide with the upper bound responses respectively, confirming the methodology to calculate the lower bound of the gross responses of the structural element.

Further, the influence of different surrounding soils on the gross responses of the structural element is investigated. The average values of the response bounds, rather than the bounds themselves, are calculated and plotted against scaled distance. Figure 4.5 indicates that the maximum displacement excluding the RBM decreases with the increase of the scaled distance, so do the maximum gross velocity and acceleration. Among the response quantities, the most significant one is the maximum acceleration. Different from the maximum displacement exclusive of the RBM and maximum gross velocity, the maximum gross acceleration is highly sensitive to soil types. For instance, for the same structure and the same scaled distance, the maximum gross acceleration may be 10 times greater when buried in the Bukit Timah soil than in dry sand. Therefore, it can be stated that for safety purpose, a buried structure should be installed in a site with small acoustic impedance and large attenuation factor such as the dry sand.

In TM-5-855-1, the maximum acceleration prediction of a buried structure under a subsurface blast load is rather coarse since only an average acceleration value across the structure in a RBM manner is given, in which the density of the surrounding soil and more importantly, the information of the structure is missing, such as the material density, the thickness of the structure element and how hollow the structure is. In the perspective of the shock mechanism, the model in the present study is more reasonable, where both the effects from the RBM and the local deflection are considered. Therefore, this model may be used as a supplement to the design codes.

Figure 4.6 is the total shock response spectra for the current case study. Generally, systems with lower natural frequencies undergo higher displacements, while the systems with higher natural frequencies experience higher accelerations instead. For a series of SDOF systems with different natural frequencies, those with mediate natural frequencies have larger velocity responses.

Table 3.3 lists some typical equipment shock tolerances (TM-5-855-1 1986). For a specific underground detonation, the shock level to the equipment can be readily obtained using the present method. Comparison of these shock values, especially the maximum accelerations, with their corresponding tolerances (drawn in Fig. 4.7) indicates whether the equipment is safe under such shock. If the shock tolerance is exceeded, isolation is needed. For the specific shock parameters applied in this study, the response spectra are plotted against the equipment natural frequencies. From Fig. 4.7, for a specific device, the stiffness of the system consisting of the device and its fixture should not exceed a certain value.

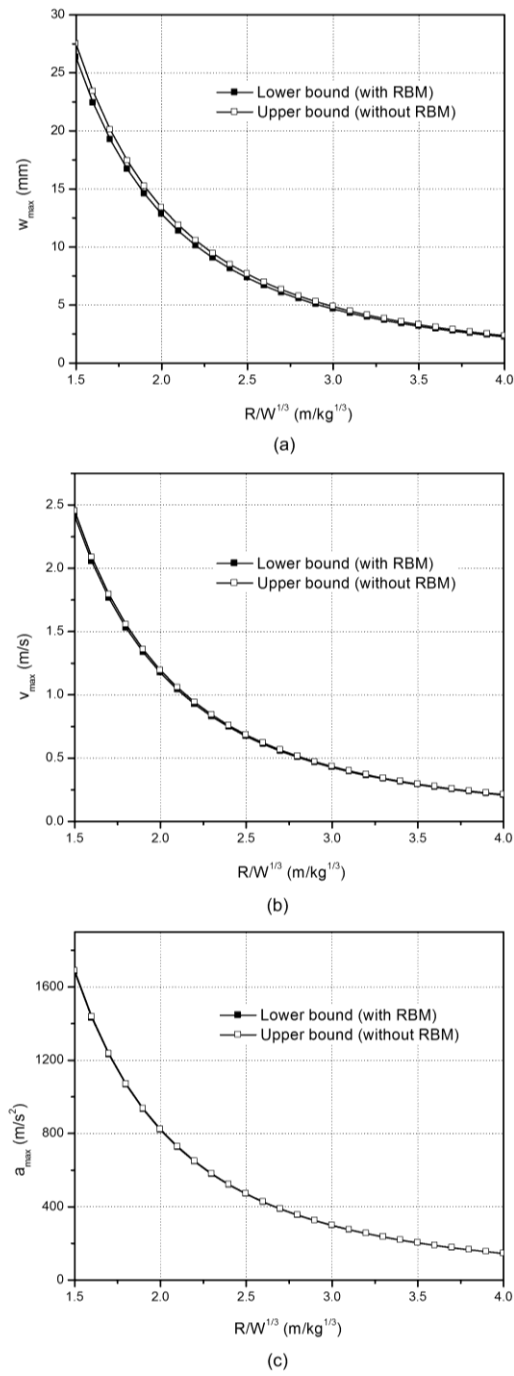


Fig. 4.5 Upper and lower bounds of (a) maximum deformation; (b) gross velocity; and (c) gross acceleration at the structural element center versus scaled distance, Kallang soil (dimension in movement direction = 300 m, for validation of the solution)

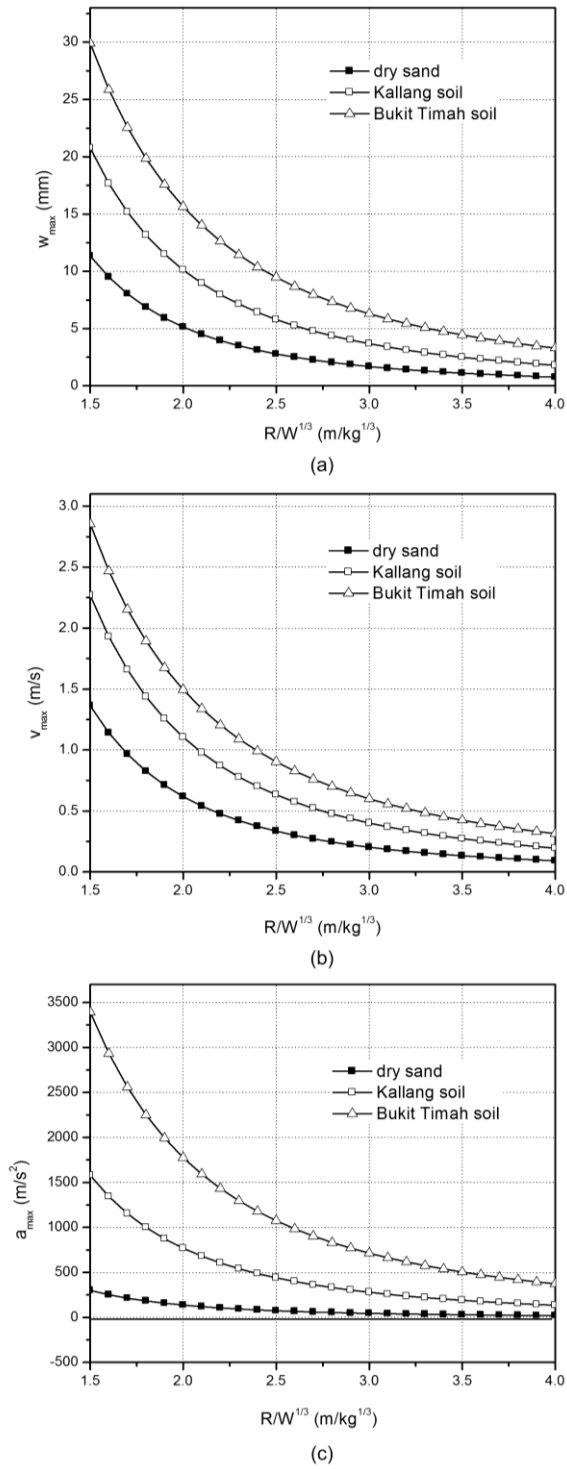


Fig. 4.6 Maximum (a) deformation; (b) gross velocity; and (c) gross acceleration of structural element center versus scaled distance: different soils

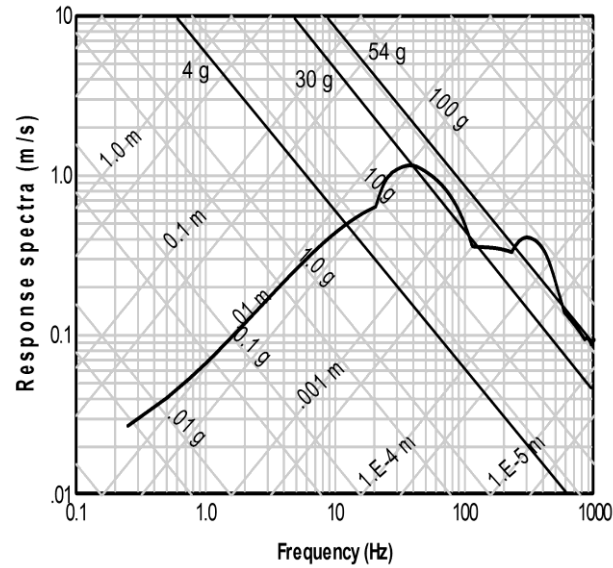


Fig. 4.7 Shock response spectra of devices subjected to in-structure shock, Kallang soil  
(vertical tolerances: 4 g- air handling units; 30 g- diesel engine generators; 54 g- computers)

## 4.5 Summary

In-structure shock evaluation of an underground structures subjected to a subsurface detonation, especially the structural shock response, is investigated analytically. An interfacial damping is incorporated to represent the soil-structure interaction. Rigid body motion of the structure as a whole and the local structural element deflection are analyzed. Shock response spectra are employed to evaluate the shock level within the structure. Comparison of the equipment shock level with the shock tolerance indicates whether the built-in equipment or device is safe or shock isolation is needed. The maximum deformation, gross velocity and gross acceleration are greater in soil with larger acoustic impedance and smaller attenuation factor, which results in higher equipment shock level and, thus, more detrimental. Especially, the maximum acceleration of the structural element is highly sensitive to soil types, thus the protective structure is better constructed in a site with small acoustic impedance and large attenuation factor for safety purpose.

## **5 DOUBLE-LAYER FLOOR TO MITIGATE IN-STRUCTURE SHOCK OF UNDERGROUND STRUCTURES: A CONCEPTUAL DESIGN**

### **5.1 Introduction**

When an underground structure is subjected to a deep subsurface explosion, the floor will experience rigid body motion (RBM) of the whole structure and deformation relative to RBM. Generally, responses of the deflection are significantly larger than those of the RBM if the structure is large and heavy (Ma and Zhou 2010). Traditionally, double-layer wall design is sometimes used for surface protective structures as sacrificial layers. Differently, in this chapter, a thin isolation slab is proposed to be installed internally near floor to mitigate vertical in-structure shock on the contained equipment. By adding such an isolation slab, subjected to the same soil-transmitted blast load, the shock excitation on the devices is altered: from the floor deflection plus the whole structure RBM to the isolation slab vibration induced by the whole structure RBM. At the edges, the slab vibration is zero and the excitation is the whole structure RBM. For this design, on one hand, the isolation slab is not necessarily thick compared to the walls and floors of the protective structure; on the other hand, only a small amount of additional space is needed since the gap between the isolation slab and the floor is negligibly small provided that it is larger than the maximum deflection of the floor when subjected to a typical subsurface detonation. Therefore, obviously, this design is simple and economical.

### **5.2 Rigid body motion of the whole structure: post-blast phase**

The rigid body motion of the whole structure within the blast duration is derived in Section 4.2. In this section, The post-loading phase rigid body motion is analyzed.



When the blast load decreases to zero, offset the time by blast duration,  $t_I = t - T_d$ , the equation of motion (EOM) of the structure after the pulse is:

$$\frac{M}{A} \frac{d^2 U(t_1)}{dt^2} + \rho_s c_s \frac{dU(t_1)}{dt} = 0 \quad (5.1)$$

Combine the EOM and initial condition, in fact the terminal displacement and velocity in the previous phase denoted as  $U(t_1 = 0)$  and  $\dot{U}(t_1 = 0)$ , the responses after the blast are:

$$U(t_1) = U(t_1 = 0) + 2\dot{U}(t_1 = 0)\tau_0 \left[ 1 - e^{-t_1/(2\tau_0)} \right] \quad (5.2a)$$

$$\dot{U}(t_1) = \dot{U}(t_1 = 0) e^{-t_1/(2\tau_0)} \quad (5.2b)$$

$$\ddot{U}(t_1) = -\frac{\dot{U}(t_1 = 0)}{2\tau_0} e^{-t_1/(2\tau_0)} \quad (5.2c)$$

where  $\tau_0 = M / (2A\rho_s c_s)$  is defined as the characteristic response time.

### 5.3 Vibration of the isolation slab

With the same surrounding soil, structural configuration and loading condition, the traditional single-floor structure is modified to a double-floor model by adding an isolation slab as the second floor, shown in Fig. 5.1. These two structures undergo exactly the same responses provided that the relatively small mass of isolation slab relative to that of the whole structure is ignored. Rather than directly mounted to and excited by the floor in traditional structures, the equipment in the double-floor structure is attached to the isolation slab, excited by the RBM-induced slab response.

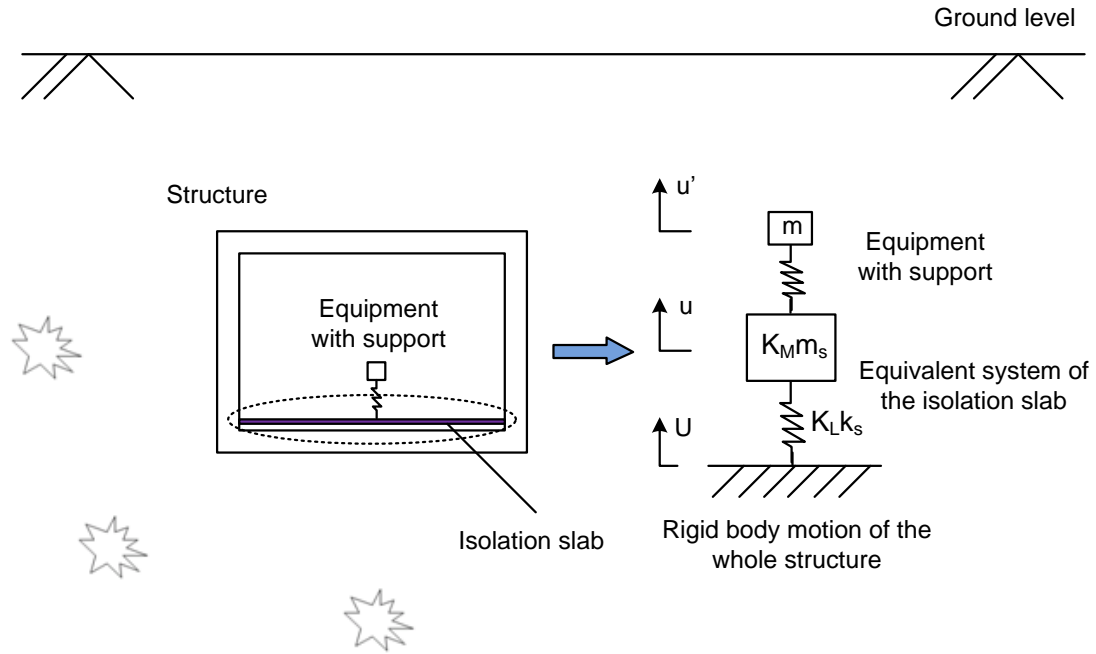


Fig. 5.1 Illustration of the newly designed underground structure and the equivalent system of the isolation slab with attached equipment

From the viewpoint of vibration theory, the advantage of the new design is the excitation source shift: for a traditional structure, shock imposed on the equipment is directly from the combination of global RBM of the whole structure plus some orders of deflection modes of the floor; in contrast, for the new designed structure with isolation slab, the excitation to the equipment is the response of the isolation slab as a secondary system thus the equipment attached becomes a tertiary system.

For practical design purpose, rigorous analysis of structures with continuous mass distribution under dynamic loads is not efficient, even not possible when the loads applied and boundary conditions are difficult to be expressed in manageable mathematical functions. Approximate design method using SDOF idealization is established and well documented (Biggs 1964). With a negligibly small mass compared to the whole structure, the isolation slab is modeled as an SDOF spring-mass system by applying the load factor and mass factor to modify its real stiffness and mass (Biggs 1964), subjected to the excitation induced by the whole structure RBM.

It should be noted that, according to Biggs (1964), this fundamental mode refers to the deformation shape under static load by assuming the dynamic load being applied statically, rather than the first order mode in vibration. With this well established method (Biggs 1964), although the idealization is applied to typical dynamic problems including blast loading, the responses obtained by this static-mode based “fundamental mode” are adequately accurate.

The possible limitation is that, if the duration of the dynamic load applied is extremely short compared to the natural periods of the structural member, i.e., an impulsive load with an almost zero duration, the excited higher order modes of structural member may affect the result accuracy to some degree.

It is worth noting that the isolation slab is built-in to the adjacent structural members. The rotation at the slab boundary is constraint to some degree, although neither fixed nor simply supported, it is closer to fixed boundary. In the present study, it is treated in two steps: first, subjected to a uniform load, the real stiffness is calculated with fixed boundary; second, when this real stiffness is idealized to that of the equivalent system, the constraint is released to some degree by applying the average of the simply supported and fixed load factors.

The equipment mounted onto the isolation slab, together with its support, is simplified as another SDOF system, attached to the SDOF system representing the isolation slab. Thus, a 2-DOF spring-mass system model without damping is established, as shown in Fig. 5.1.

In engineering practice, the mass of the equipment is always significantly smaller than that of the isolation slab. Therefore the 2-DOF system consisting of isolation slab and equipment with support can be decoupled while retaining adequate accuracy. The procedure is: first remove the equipment and analyze the SDOF system representing the isolation slab. Then the response of the SDOF system representing the equipment with support can be obtained with the isolation slab response as excitation. That is, when the mass of the device is significantly smaller than that of the isolation slab, the

2-DOF system becomes an SDOF system. Corresponding to the RBM responses as excitation, the isolation slab responses are derived separately in two phases, i.e., loading and post-loading phases.

### 5.3.1 Phase I: loading phase

The EOM of the isolation slab equivalent SDOF system can be written as:

$$K_M m_s \ddot{u}(t) + K_L k_s u(t) = K_M m_s \frac{P_0 \alpha}{\rho_s c_s} \left[ \frac{1}{T_d} - \left( \frac{1}{\tau_0} + \frac{1}{T_d} \right) e^{-t/\tau_0} \right] \quad (5.3)$$

where  $u(t) = x_s(t) - U(t)$  is the relative displacement between the isolation slab and the whole structure.  $\alpha$  is a reduction factor, defined as ratio of the equivalent uniform pressure on a wall or floor of the structure to the maximum pressure of the actual load distribution. Define circular natural frequency of the equivalent system:

$$\omega = \sqrt{\frac{K_L k_s}{K_M m_s}} \quad (5.4)$$

In structural engineering, a typical damping ratio,  $\zeta=0.05$ , is used (Clough and Penzien 1993). Then, adding such a damping and the EOM is simplified as:

$$\ddot{u}(t) + 2\zeta\omega\dot{u}(t) + \omega^2 u(t) = \frac{P_0 \alpha}{\rho_s c_s} \left[ \frac{1}{T_d} - \left( \frac{1}{\tau_0} + \frac{1}{T_d} \right) e^{-t/\tau_0} \right] \quad (5.5)$$

At the beginning, there is no relative displacement and velocity between the whole structure and isolation slab:

$$u(0) = 0, \dot{u}(0) = 0 \quad (5.6)$$

Combine the EOM and the initial conditions, the responses of the equivalent SDOF system in the blast duration are:

$$u(t) = e^{-\zeta\omega t} (F \sin Dt + P \cos Dt) + \frac{S}{\omega^2} - \frac{B\tau_0^2}{1 - 2\zeta\omega\tau_0 + \omega^2\tau_0^2} e^{-t/\tau_0} \quad (5.7)$$

where

$$B = \frac{P_0\alpha}{\rho_s c_s} \left( \frac{1}{\tau_0} + \frac{1}{T_d} \right), \quad D = \sqrt{1 - \zeta^2} \omega, \quad S = \frac{P_0\alpha}{\rho_s c_s} \frac{1}{T_d}$$

$$F = -\frac{\zeta S}{D\omega} + \frac{B\tau_0(\zeta\omega\tau_0 - 1)}{D(1 - 2\zeta\omega\tau_0 + \omega^2\tau_0^2)}, \quad P = -\frac{S}{\omega^2} + \frac{B\tau_0^2}{1 - 2\zeta\omega\tau_0 + \omega^2\tau_0^2}$$

Then velocity and acceleration can be readily obtained:

$$\dot{u}(t) = e^{-\zeta\omega t} \left[ -(\zeta\omega F + PD) \sin Dt + (-\zeta\omega P + FD) \cos Dt \right] + \frac{B\tau_0}{1 - 2\zeta\omega\tau_0 + \omega^2\tau_0^2} e^{-t/\tau_0} \quad (5.8)$$

$$\ddot{u}(t) = e^{-\zeta\omega t} \left[ (\zeta^2\omega^2 F + 2\zeta\omega PD - FD^2) \sin Dt + (\zeta^2\omega^2 P - 2\zeta\omega FD - PD^2) \cos Dt \right]$$

$$- \frac{B}{1 - 2\zeta\omega\tau_0 + \omega^2\tau_0^2} e^{-t/\tau_0} \quad (5.9)$$

### 5.3.2 Phase II: post-loading phase

Similarly, the governing equation of the isolation slab equivalent SDOF system after the blast load is:

$$\ddot{u}(t_1) + 2\zeta\omega\dot{u}(t_1) + \omega^2 u(t_1) = C e^{-t_1/(2\tau_0)} \quad (5.10)$$

where

$$t_1 = t - T_d, \quad C = \frac{\dot{U}(t = T_d)}{2\tau_0}$$

Combine the governing equation and initial conditions, the displacement of the equivalent SDOF system after the blast is:

$$u(t_1) = e^{-\zeta\omega t_1} (G \sin Dt_1 + Q \cos Dt_1) + \frac{4\tau_0^2 C}{1 - 4\zeta\omega\tau_0 + 4\omega^2\tau_0^2} e^{-t_1/(2\tau_0)} \quad (5.11)$$

where

$$G = \frac{\omega\tau_0 H + I}{D} + \frac{2\tau_0(1 - 2\tau_0^2\omega)C}{D(1 - 4\zeta\omega\tau_0 + 4\omega^2\tau_0^2)}, \quad Q = H - \frac{4\tau_0^2 C}{1 - 4\zeta\omega\tau_0 + 4\omega^2\tau_0^2}$$

and

$$H = u(t = T_d) = e^{-\zeta\omega T_d} (F \sin DT_d + P \cos DT_d) + \frac{S}{\omega^2} - \frac{B\tau_0^2}{1 - 2\zeta\omega\tau_0 + \omega^2\tau_0^2} e^{-T_d/\tau_0}$$

$$I = \dot{u}(t = T_d) = e^{-\zeta\omega T_d} [-(\zeta\omega F + PD) \sin DT_d + (-\zeta\omega P + FD) \cos DT_d] + \frac{B\tau_0}{1 - 2\zeta\omega\tau_0 + \omega^2\tau_0^2} e^{-T_d/\tau_0}$$

are the initial conditions of the time starting at the end of blast duration, in fact, the terminal response in the blast duration.

Similarly the velocity and acceleration after the blast can be obtained:

$$\dot{u}(t_1) = e^{-\zeta\omega t_1} [-(\zeta\omega G + QD) \sin Dt_1 + (-\zeta\omega Q + GD) \cos Dt_1] - \frac{2\tau_0 C}{1 - 4\zeta\omega\tau_0 + 4\omega^2\tau_0^2} e^{-t_1/(2\tau_0)} \quad (5.12)$$

$$\ddot{u}(t_1) = e^{-\zeta\omega t_1} \left[ (\zeta^2\omega^2 G + 2\zeta\omega QD - GD^2) \sin Dt_1 + (\zeta^2\omega^2 Q - 2\zeta\omega GD - QD^2) \cos Dt_1 \right] + \frac{C}{1 - 4\zeta\omega\tau_0 + 4\omega^2\tau_0^2} e^{-t_1/(2\tau_0)} \quad (5.13)$$

It is worth noting that the above solutions of both phases are relative displacement, velocity and acceleration between the isolation slab equivalent system and the whole structure. Finally, summation of these relative responses and the rigid body motion, yields the total responses at the isolation slab center.

In addition, the responses obtained above are for the isolation slab center while the vibrations in the four edges of the slab are the rigid body motion of the whole structure. In the elastic range, superposition principle holds. The response of the locations other than the slab center and edges should be the sum of the whole structure RBM response and the relative deflection response between the isolation slab and the whole structure, which can be interpolated using the shape function and the slab center response. For instance, the approximate shape can be chosen as double sine function.

### **5.3.3 Shock of equipment attached to the isolation slab**

Until now the acceleration time history of the isolation slab is obtained, which is in fact the excitation for the equipment. Further, with the same method, the responses of the equipment with support, modeled as another SDOF system, can be obtained. In engineering practice, to determine whether a device is damaged by a shock, the maximum acceleration regardless of direction is compared with the corresponding tolerance. If the acceleration applied on the device exceeds that of the tolerance (typical values are listed in TM-5-855-1), damage occurs. Here, shock response spectra method (Gupta 1992), well documented, is employed to calculate the maximum acceleration of various devices with supports simplified as SDOF systems of various natural frequencies.

It is worth noting that the system consisting of the isolation slab and the equipment, a typical primary and secondary system, is analyzed with a decoupled method. For a primary and second system, decoupled analysis can be applied with adequate accuracy if the frequency of the primary system only changes slightly no matter the secondary system is coupled or not (Gupta 1992). Therefore, in the present study, if the mass of

the equipment is significantly smaller than that of the isolation slab, the accuracy of the decoupling analysis is adequate. Otherwise, a coupled analysis is required.

## 5.4 A case study and discussions

Consider a box-typed protective structure with an isolation slab, installed in dry sand, subjected to a blast load induced by a subsurface detonation. The detailed structural and loading parameters are:

$$\rho=2500 \text{ kg/m}^3$$

$$E=30 \text{ GPa}$$

$$\nu=0.2$$

$$L_1=9 \text{ m (length of the structure)}$$

$$L_2=7 \text{ m (width of the structure)}$$

$$L_3=5 \text{ m (height of the structure)}$$

$$h=0.5 \text{ m (uniform thickness of all structural members except the isolation slab)}$$

$$h_s=0.2 \text{ m (thickness of the isolation slab)}$$

$$\frac{R}{W^{1/3}} = 2 \text{ m/kg}^{1/3} (R=10 \text{ m, } W=125 \text{ kg})$$

$$T_d=20 \text{ ms (typical for underground detonation, Anand 2002)}$$

$$\alpha=0.65$$

$$f=1$$

$$K_L=0.435$$



$$K_M=0.31$$

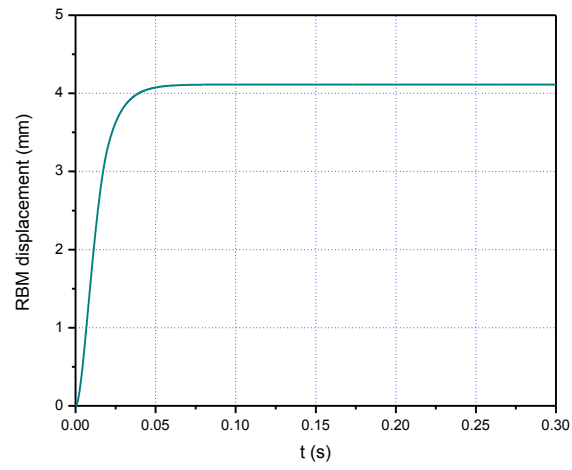
where  $K_L$  and  $K_M$  are obtained as follows: with the dimension ratio of the isolation slab about 0.75, the load factors are read 0.5 and 0.37 for simply supported and fixed boundaries; and the mass factors are read 0.36 and 0.26 for simply supported and fixed boundaries. Then through averaging, the load factor and mass factor are taken as 0.435 and 0.31, respectively.

The equivalent mass of the isolation slab is:

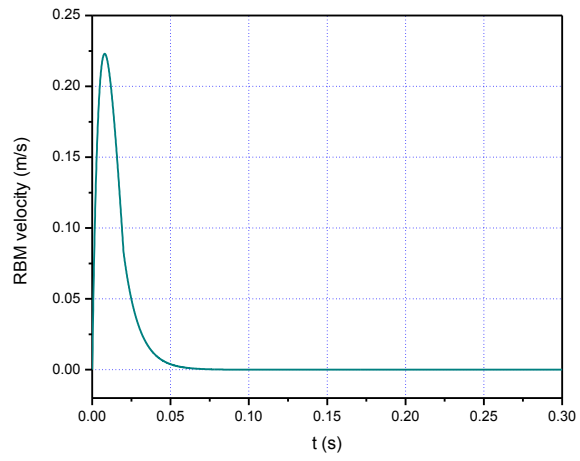
$$K_M m_s = 0.31 \times 2500 \times (0.2 \times 7 \times 9) = 9765 \text{ kg}$$

Obviously the mass of a typical device with support attached to the isolation slab is significantly smaller than that of the slab. Therefore it is reasonable to decouple the isolation slab response from that of the device with support.

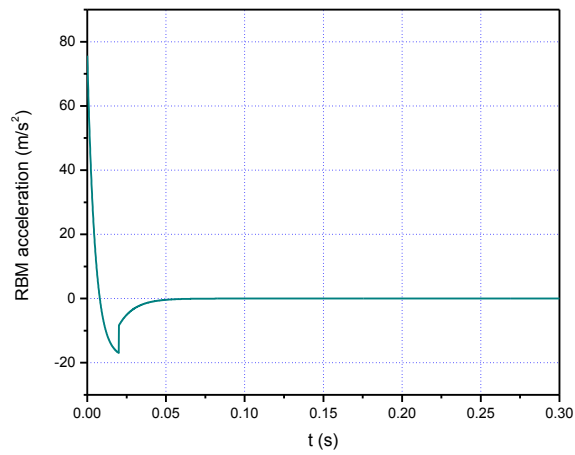
Fig. 5.2 shows the RBM responses of the whole structure. In this case the RBM displacement continues to increase after the blast load vanished at 0.02 s and stops at about 0.05 s with a maximum value of approximate 4 mm. It is known that the RBM displacement is negligibly small due to the huge mass of the structure. The RBM velocity starts at zero and achieves its peak 0.225 m/s quickly at about 0.009 s then attenuation to zero around 0.05 s. Among these RBM responses, the acceleration is of most significance since it is the direct excitation for the isolation slab and subsequently indirect excitation for the equipment. At time zero, it achieves peak value, approximately 8 g, and attenuates in a high rate to zero at about 0.05 s.



(a)



(b)



(c)

Fig. 5.2 The rigid body motion responses of the whole structure

It is worth noting that when the soil particle velocity, calculated as the free field pressure divided by the soil acoustic impedance, is larger than the structure velocity, the blast load applies onto the structure. Otherwise, if the soil particle velocity is smaller than the structure velocity, the soil-transmitted load cannot apply on the structure. Possibly, according to this criteria, there may or may not be re-contact and re-separation between the soil and structure, depending on the blast load time history, soil and structure characteristics. In the present study, the velocity time histories with and without soil-structure separation are plotted, together with the soil particle velocity time history. From Fig. 5.3, the difference is not significant, which implies neglecting the soil-structure separation is reasonable.

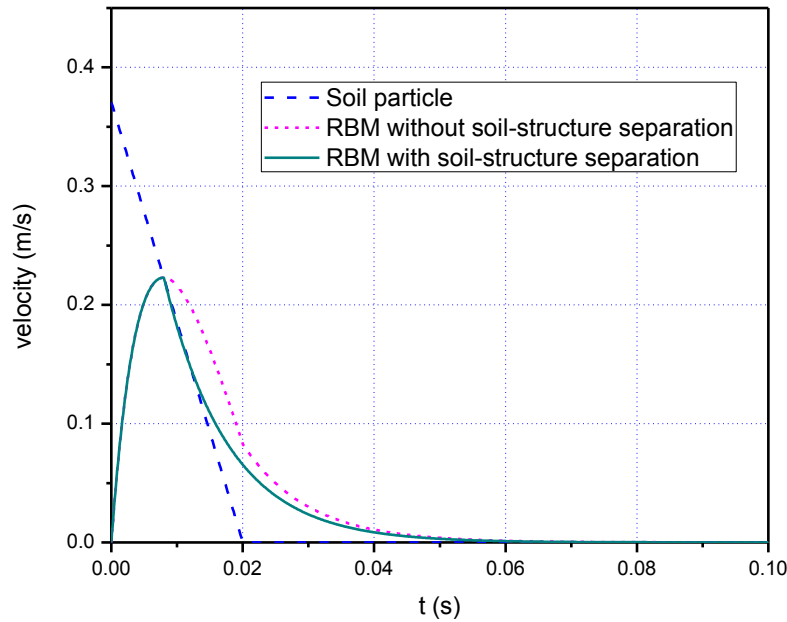
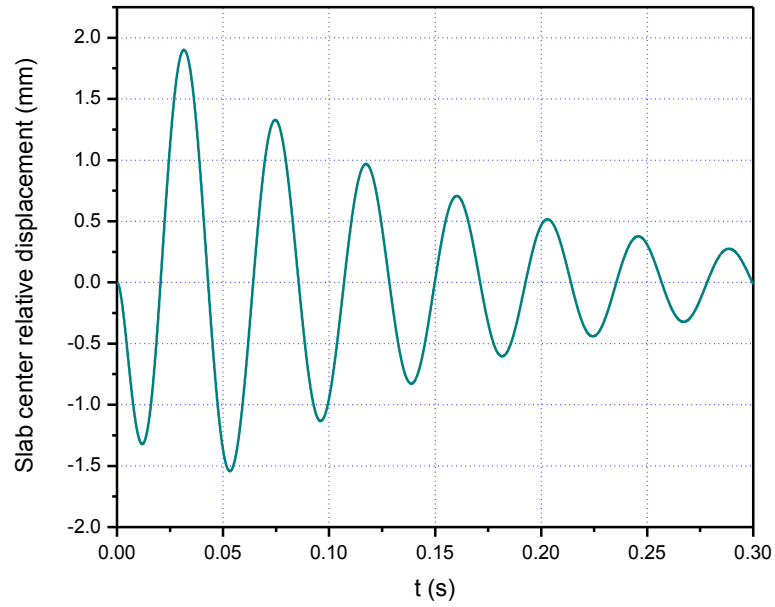


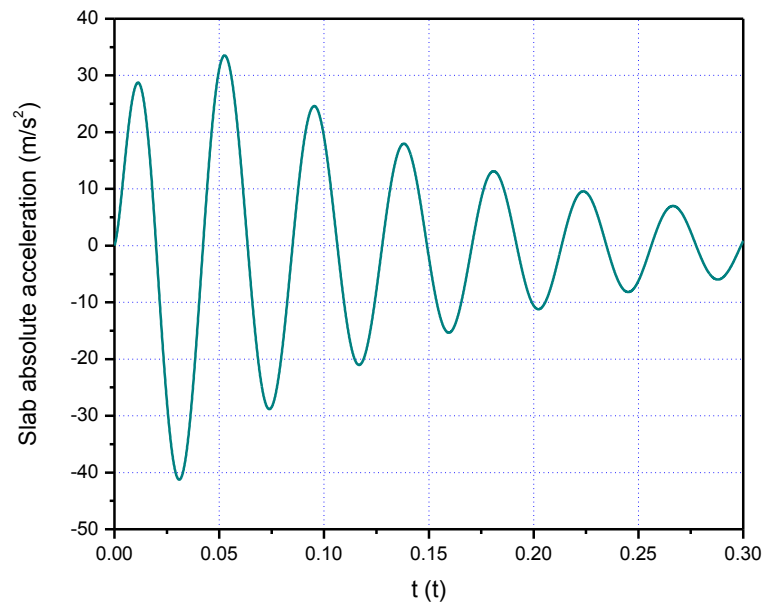
Fig. 5.3 Rigid body motion velocities: with and without soil-structure separation

Further, with the RBM acceleration time history as excitation, the responses of the isolation slab are obtained, shown in Fig. 5.4. The maximum relative displacement between the isolation slab center and the floor is less than 2 mm. Compared to the thickness of 0.2 m, one can know the slab deflection is elastic and will not cause any

damage. When it comes to the absolute acceleration at the isolation slab center, it is favorable to know the peak acceleration is reduced to 4 g.



(a) Relative deflection time history.



(b) Absolute acceleration time history.

Fig. 5.4 The relative deflection and absolute acceleration time histories at the isolation slab center

It is obvious that the acceleration response at the isolation slab center depends on its natural frequency, which is determined by the stiffness and mass. To address this issue, in the present case, all the parameters including the geometrical dimensions and material of the structure as well as the blast load are fixed except the isolation slab equivalent natural frequency. Fig. 5.5 indicates that when its natural frequency is low, in other words, when the slab is relatively flexible, the maximum acceleration is low. The peak isolation slab acceleration increases with the natural frequency before certain value, e.g. 1600 Hz; after that the peak acceleration decreases. It is validated that if the natural frequency of the isolation slab becomes infinite, the acceleration time history of the slab center will exactly converge to that of the RBM of the whole structure. In the range of engineering application, theoretically, under the same blast, the more flexible the isolation slab is, the more effective the in-structure shock mitigation will be. However, this slab may not be too flexible since it will become unstable due to personnel movement and excessively large deflection may occur. Therefore based on these considerations, in design, the thickness of the isolation slab should be judiciously selected to balance the shock mitigation effect and stability.

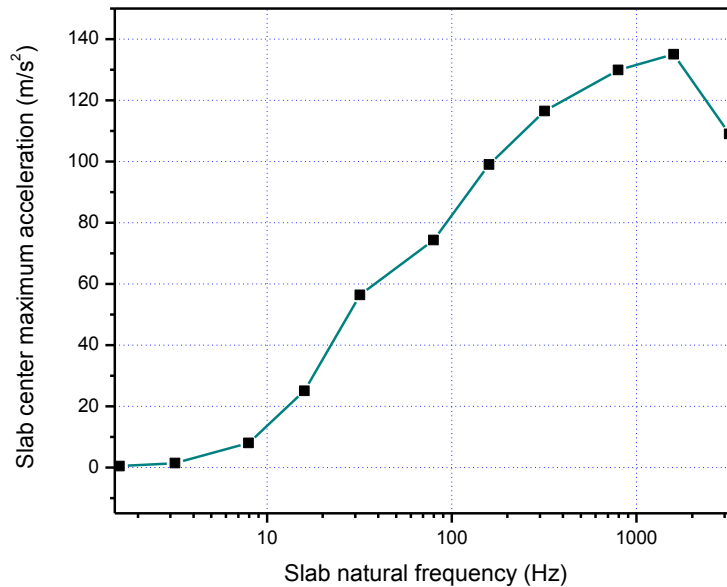


Fig. 5.5 The maximum acceleration of the isolation slab center with respect to slab natural frequency

Then shock response spectra of the equipment attached to the isolation slab subjected to vertical in-structure shock when the structure is buried in dry sand are established. The excitations for the equipment mounted near the edges and at the center of the isolation slab are shown in Fig. 5.2(c) and Fig. 5.4(b), respectively. It is obvious that these two excitations have different characteristics: the one at the isolation slab center is an attenuating oscillation with a lower peak value and a relatively long period while the one at the slab edges has a higher peak value and a relatively short duration. From Fig. 5.6, if the natural frequency of the SDOF system consisting of the equipment and support is less than 5 Hz, the peak acceleration on the equipment near the slab edge, excited in fact by the whole structure RBM, is higher than that of the equipment placed at the slab center; otherwise, shock on equipment at the slab center is severer. Further, from Fig. 5.6, it is worth noting that the equipment with support having a natural frequency of 20 Hz experiences highest acceleration level of approximately 16 g under this specific structural configuration and blast load. Therefore in engineering application, before constructing the protective structure and installing the equipment, shock spectra analysis should be conducted to select appropriate thickness and material of the isolation slab as well as the natural frequency of the equipment with support so that possible strong shock under certain blast load on equipment can be avoided.

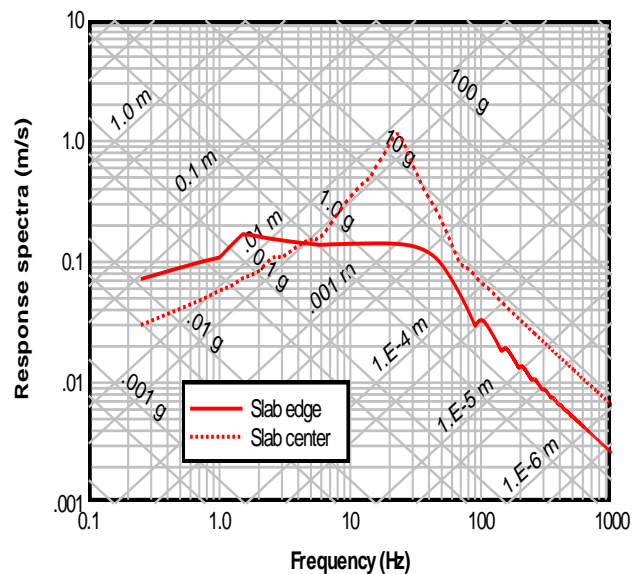


Fig. 5.6 Shock response spectra at isolation slab center and edges: dry sand

Besides the scenario of the structure being installed in dry sand, more situations are also analyzed for structure buried in other soils (Kallang soil and Bukit Timah soil, two typical soils in Singapore), shown in Fig. 5.7 and Fig. 5.8. Similar conclusions can be made to the shock intensity on equipment near the isolation slab edge and at the center. With increase of acoustic impedance and decrease of attenuation coefficient of the surrounding soil, the shock applied on the equipment become severer no matter where the equipment is placed: near slab edges or at center. Thus as expected, the protective structure should be installed in a soil with small acoustic impedance and large attenuation coefficient such as dry sand.

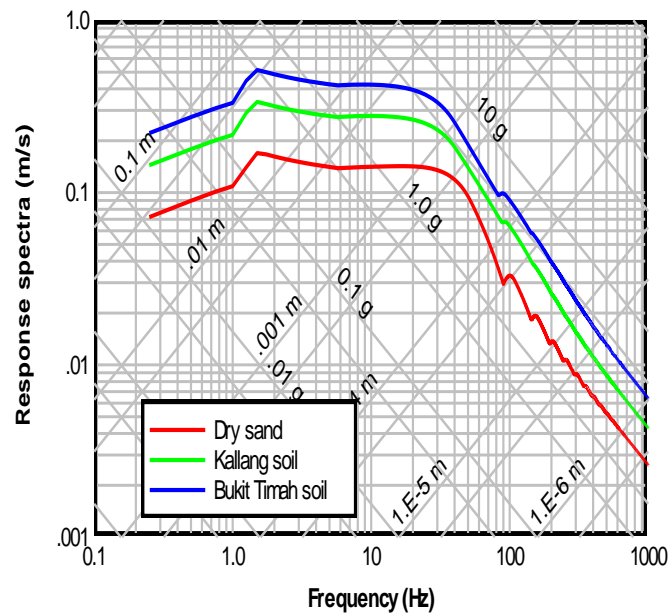
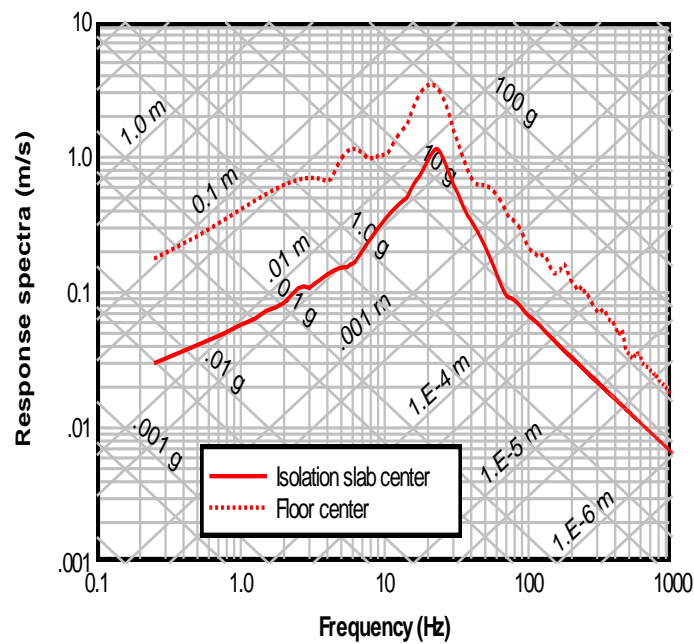


Fig. 5.7 Comparison of shock response spectra for equipment near isolation slab edges:  
structure in different soils

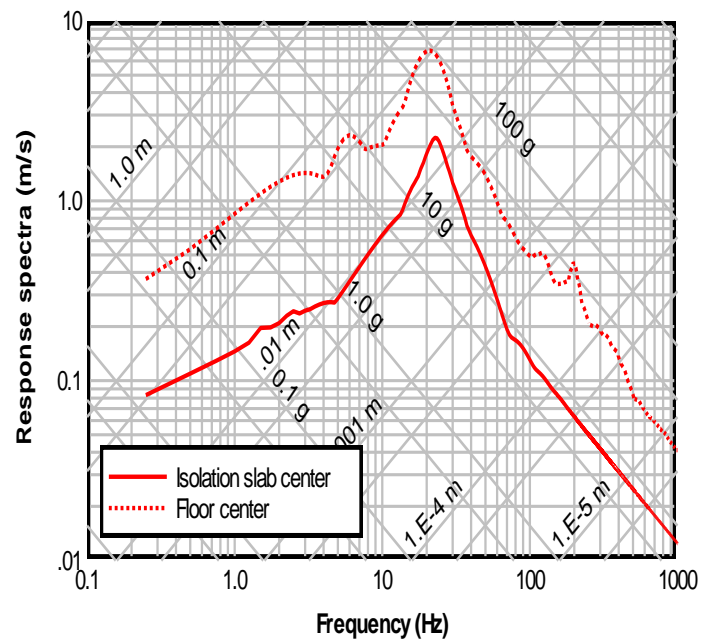
Finally the vertical in-structure shock mitigation effect of the new design is examined by comparing the shock level on equipment. A traditional protective structure of the same configuration but without isolation slab is considered to be installed in dry sand, Kallang soil and Bukit Timah soil, respectively and subjected to a blast load induced by the same subsurface detonation as in the present, the shock levels are evaluated (Ma et

al. 2011). Figure 5.8 shows the comparison of the shock level on the equipment attached to the centers of the isolation slab of the new structure and the floor of the traditional structure, respectively and one can know that by adopting such a design, at least 50% and even higher reduction of the vertical in-structure is achieved in the present case. Further, it is worth noting that the vertical shock mitigation efficiency also depends on the dimensions of the underground structures. For a buried structure with large dimensions and relatively thin wall thickness, rather than a small one with relatively thick walls, the excitation difference for the equipment between the traditional and double-floor structures are significant: the floor deflection dominates while rigid body motion of the whole structure reduces significantly, resulting in a greater excitation for equipment in traditional protective structures and lower excitation

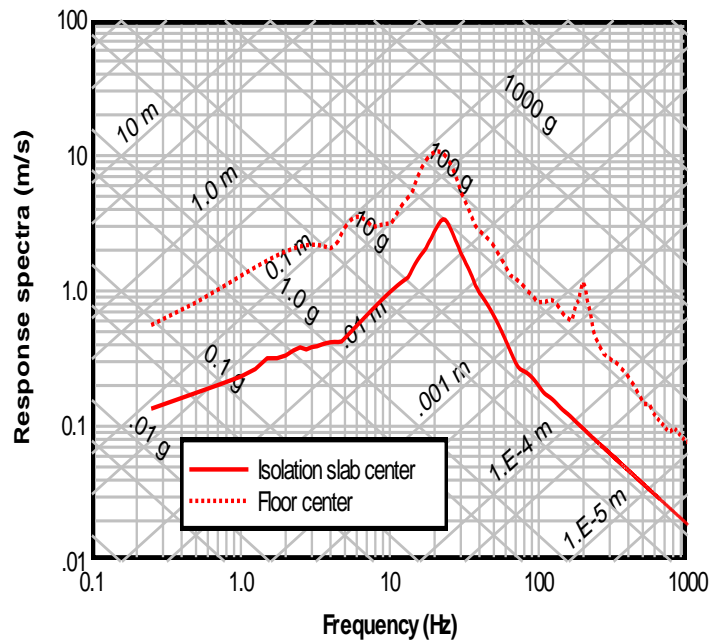


(a) In dry sand.





(b) In Kallang soil.



(c) In Bukit Timah soil.

Fig. 5.8 Shock response spectra comparison: structure with and without isolation slab  
in three typical soils

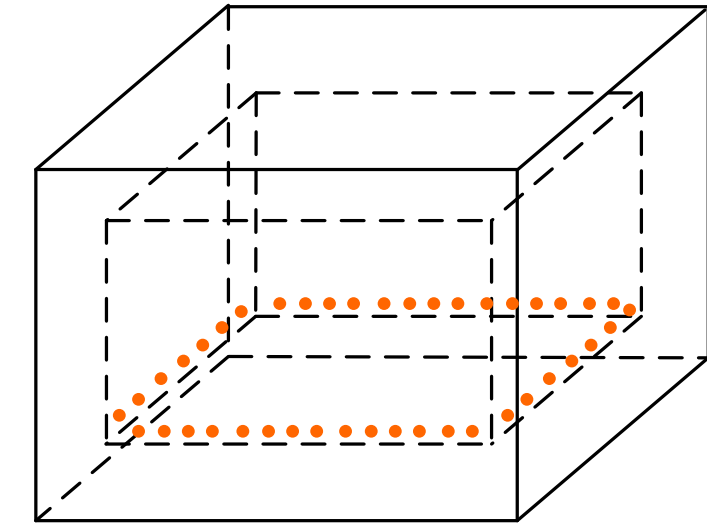
for equipment in the newly proposed structure with isolation slab. Therefore the vertical shock mitigation efficiency of double-floor underground structures increases with structural dimensions. At the same time, the stability of the isolation slab should also be examined in design.

## **5.5 Summary**

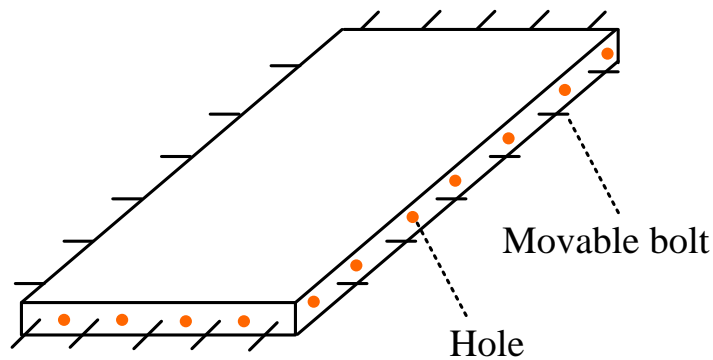
A simple mitigation method for in-structure shock of underground protective structures is proposed. By adding an isolation slab, the excitation for the equipment at the floor center is altered. The excitation source is changed from combination of floor deflection plus rigid body motion of the whole structure to that of the isolation slab. The excitation pattern for the equipment is altered from a shock with a higher peak acceleration and a shorter duration to an attenuation oscillation with a lower peak acceleration and a longer duration. Case study shows that at the isolation slab center, the vertical in-structure shock level on the equipment is effectively reduced while near the edges the shock intensity on equipment is not high. Therefore this design exhibits excellent capacity to reduce the vertical shock level on equipment thus it may provide a supplementary reference for further design and modification of underground structures. The proposed conceptual design of underground structure for mitigating vertical in-structure shock should be verified and validated experimentally.

In engineering practice, the construction of the underground structure is further complicated by adding an isolation slab. For easy modification of existing structures with traditional floors and maintenance, a relatively convenient construction method is presented as follows. First, drill holes in the four walls near the floor where the isolation slab is planned to be installed, shown in Fig. 5.9(a). Then, according to the dimensions of the floor, manufacture several pieces of isolation slab segments with movable bolts (the bolts can be moved into and out of the slab segment with prefabricated devices, similar to locks) and prefabricated holes in every sides, indicated

in Fig. 5.9(b). Finally, install these isolation slab segments into the walls and connect them with each other with the holes and movable holes.



(a)



(b)

Fig. 5. 9 Illustration of the installation of the isolation slab (not to dimension, for illustration purpose only)

Without doubt, the construction cost for an underground structure with such an isolation slab will increase. In fact, the cost is usually not a major concern for protective structure design.

## **6 IN-STRUCTURE SHOCK OF UNDERGROUND STRUCTURES: EXPERIMENTAL INVESTIGATION**

### **6.1 Introduction**

In all the previous study of in-structure shock of underground structures (Weidlinger and Hinman 1988; Alwis and Lam 1996; Ma et al. 2010; Ma et al. 2011), the free field load of the soil-transmitted blast is assumed as an impulse with an instantaneous peak and a rapid linear decay, similar to the one induced by an airburst. In the occasions when the in-structure shock of underground structures is taken into account, the standoff distance is relatively distant and soil or backfill surrounding the structure is relatively soft, it is reasonable to take into consideration the rise time of the soil-transmitted blast load. In this chapter, the rise time of the blast load is considered in the determination of the dynamic structural response and a small scale test is conducted to validate the prediction. It is evident that the in-structure shock is over-predicted by using the blast load with zero rise time. The aim of this study is to make the in-structure shock prediction more reasonable.

### **6.2 Structural response prediction under pulse of non-zero rise time**

For a typical underground structure subjected to a soil-transmitted blast load induced by a subsurface detonation, the most critical situation is considered: the explosion is in the extended line of the structure's symmetry axis. With the rise time taken into consideration, the blast pressure is a triangular load, schematically shown in Fig. 6.1.

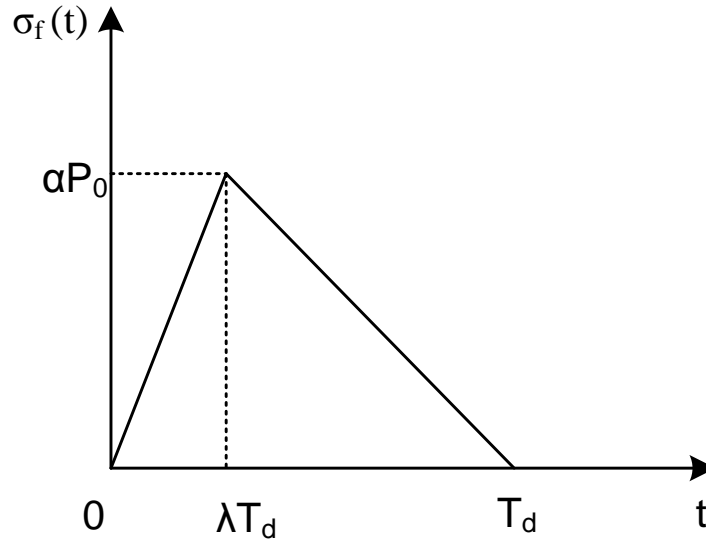


Fig. 6.1 The idealized profile of a soil-transmitted blast

$$\sigma_f(t) = \begin{cases} \frac{P_0 \alpha t}{\lambda T_d} & \text{for } t \leq \lambda T_d \\ \frac{P_0 \alpha (T_d - t)}{(1 - \lambda) T_d} & \text{for } \lambda T_d < t \leq T_d \end{cases} \quad (6.1)$$

where the peak pressure:

$$P_0 = \beta f (\rho_s c_s) \left( \frac{R}{W^{1/3}} \right)^{-r} \quad (6.2)$$

where  $P_0$  is the free-field peak pressure, in psi;  $f$  is a coupling factor of the explosion energy to soil, dimensionless;  $\alpha$  is a reduction factor, defined as ratio of the equivalent uniform pressure on a wall or floor of the structure to the maximum pressure of the actual load distribution;  $\rho_s c_s$  is the acoustic impedance of soil, in psi/fps;  $r$  is an attenuation coefficient, dimensionless;  $W$  is the TNT equivalent charge weight, in lb;  $R$  is the distance measured from the center of explosion to the structure, in ft;  $\beta$  is a factor equal to 160 in the imperial unit system, dimensionless; and  $\lambda$  is a dimensionless

number ranging from 0 to 1. It should be noted that the pressure calculated in psi is converted to SI unit system in Pa before being used in the following.

The key response for the in-structure shock excitation, the major part of the acceleration time history, is in the initial stage of a typical underground blast load and the remaining acceleration time history almost have no contribution. Therefore in the present study, only the response of the structural member within the blast duration is investigated. Further, for a typical underground protective structure, the influence of the global rigid body motion (RBM) is not significant (Ma et al. 2011) thus in the present study, RBM is not considered.

In engineering practice, a structural member of one dimension greater than twice the other or supported only at the opposite edges, is often simplified and analyzed by a beam model in plane strain manner, similar to the model in Chapter 3. The supports of the idealized beam representing the structural member is neither fixed nor simply supported. In the present study, simply supported boundary is used to yield a conservative prediction. Further, a square structural member with two opposite edges simply supported or fixed along, also can be idealized as a beam to analyze.

The response of a structural member subjected to a soil-transmitted blast is derived using the same methodology in Chapter 3, in which the soil-structure interaction is considered but rigid body motion is not incorporated since for a typical underground structure, this effect is not significant (see Chapter 4). The formulations are given in detail in Appendix A.

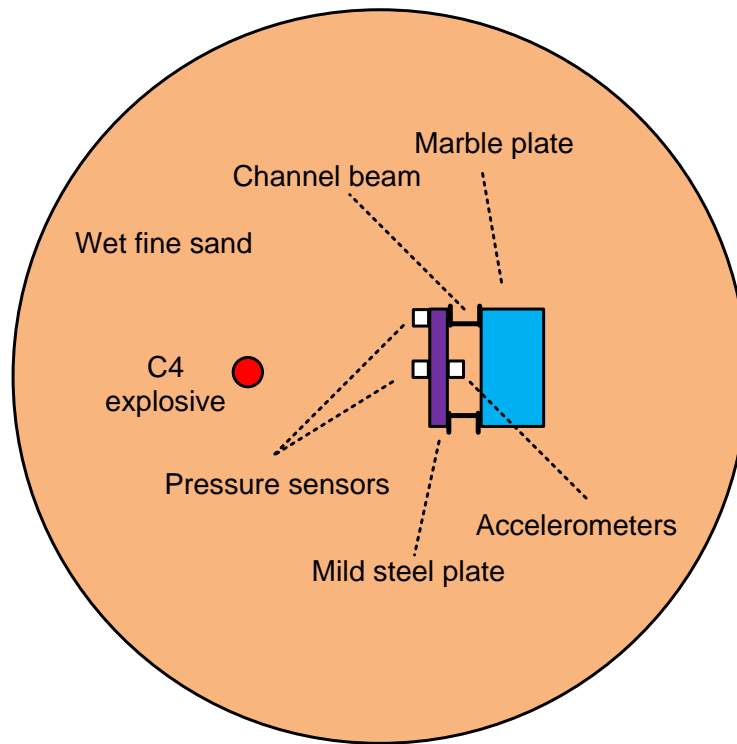
## **6.3 Experiment set-up**

Generally, underground facilities are installed in soil with small acoustic impedance and large attenuation coefficient such as sand and soft soil; otherwise, backfilling is necessary. In the present study, to realistically simulate the soil-transmitted blast, wet fine sand is used as surrounding soil. A large empty cylinder of diameter 6 m is filled

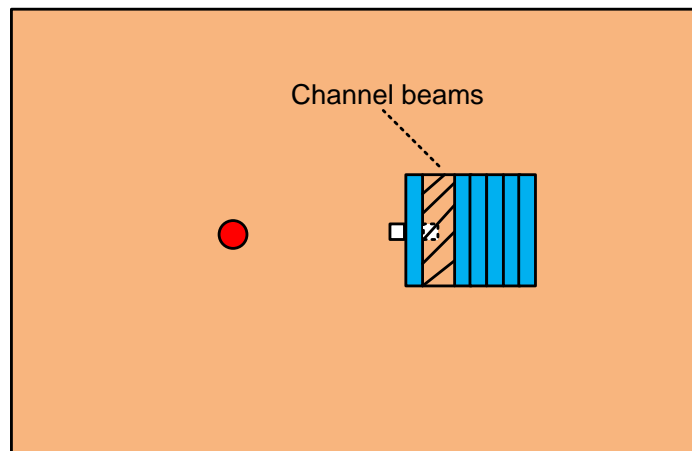
with wet fine sand and the experimental set-up is installed in the middle part. Based on the characteristic dimension of the test site and the acoustic velocity of the wet fine sand, the reflections from the cylinder boundary have no influence to the response of the test structural member thus the test can be considered as being carried out in an infinite medium. The overall design of the experiment is illustrated in Fig. 6.2.

The nature of in-structure shock of underground facilities is the equipment failure under the damaging excessive acceleration induced by the soil-transmitted blast load, in which the main structure only experiences light or even no damage. It is reasonable to analyze the elastic structural responses of the main structure. Subsequently, to ensure the deformation is elastic, a small scale test is designed with mild steel plate and marble stone to represent an underground structure.

To simulate a box-typed underground structure, a test system of one mild steel plate with two channel beams as supports, clamps as well as the marble block are constructed. The mass of the front plate is significantly small compared to the total mass of the test system consisting of the plate, channel beams, wood blocks as well as the steel clamps and the marble plates shown in Fig. 6.3, therefore the influence of rigid body motion can be neglected (Ma et al. 2011). The structural element nearest to the subsurface detonation is represented by the steel plate. In engineering practice where an underground structure is constructed, the boundary condition for this structural member is attached to other four members: neither simply supported nor fixed. In fact, its constraint effect is in between. In the current test, this effect is realized by the clamps with wood blocks, shown in Fig. 6.3(a): the constraints are stronger than simply supported and weaker than fixed boundaries. For convenience of the test set-up, the other two boundaries are kept free so that the mild plate can be analyzed with modified beam model.



(a) Plan view



(b) Side view

Fig. 6.2 The designed test set-up (not to scale)





(a)



(b)

Fig. 6.3 The small scale test set-up

The equipment or devices attached to the main structure is not simulated in the present test since once the responses, especially the acceleration time history, of structural member are obtained, the maximum acceleration experienced by the equipment can be readily calculated with well established shock response spectrum method (Gupta 1992).

An accelerometer is connected to the plate center and pressure sensors are connected to the plate center and column, respectively. First the test system is installed in wet fine sand then it is backfilled.

The ratio of rise time to blast duration is adopted as 0.1. It is taken from the free field pressure time histories induced by subsurface detonations from exactly the same soil in National Defense Academy, Japan (Beppu et al. 2011).

## **6.4 Determination of the standoff distance and plate dimensions**

To make sure the steel plate representing the structural member, nearest to the detonation, deforms elastically, based on the parameters of soil, charge type and weight, the combination of standoff distance and plate dimensions are determined as follows.

For a beam with uniformly distributed load or nearly such uniform load, the maximum bending moment in midspan is:

$$M_{\max} = \frac{pl^2}{8} \quad (6.3)$$

where  $p$  is the linear intensity of the uniform load,  $l$  is the span of the beam.

When the beam or plate is loaded with blast pressure induced by subsurface detonation, the maximum pressure applied is at the beginning of the beam response, which is 2 time the free-field pressure:

$$p = 2P_0 \quad (6.4)$$

where  $P_0$  is the peak value of the induced free-field pressure from subsurface blast.

The maximum stress under uniform-load-caused-bending is:

$$\sigma_m = \frac{M_{\max}}{\frac{h^3}{12}} \frac{h}{2} \quad (6.5)$$

where  $h$  is the thickness of the beam,  $h^3 / 12$  is the inertia moment. Here beam width equal to unity.

For elastic response, the maximum stress (in the surface of the beam) must be smaller than the yield strength of normal steel:

$$\sigma_m = \frac{M_{\max}}{\frac{h^3}{12}} \frac{h}{2} = \frac{\frac{2P_0 l^2}{8}}{\frac{h^3}{12}} \frac{h}{2} \leq \sigma_y \quad (6.6)$$

From Eq. (6.6), we have:

$$\frac{l}{h} \leq \sqrt{\frac{2\sigma_y}{3P_0}} \quad (6.7)$$

Given the yield strength of normal steel  $\sigma_y$  as 250 MPa, with the peak free-field pressure, the relationship between beam span  $l$  and thickness  $h$  can be determined. Through calculation, the mild steel plate is chosen as 20 cm by 20 cm (effective span between the two channel beam supports) with a thickness of 3.2 mm. The standoff distance is chosen as 40 cm and 60 cm, respectively. The time histories acceleration and strain at the plate center are recorded to validate the previous analytical formulations.

The detailed parameters of the experiment are:

$\rho=7800 \text{ kg/m}^3$  (density of mild steel)

$E=210 \text{ GPa}$  (Young's modulus of mild steel)

$\nu=0.3$  (Poisson's ratio of mild steel)

$\sigma_y=250 \text{ MPa}$  (yield strength of mild steel)

$l=0.2 \text{ m}$  (distance between the two channel beam supports)

$h=0.0032 \text{ m}$  (thickness of the plate, 3.2 mm)

$\rho_s=1598 \text{ kg/m}^3$  (density of wet fine sand)

$c_s=200 \text{ m/s}$  (acoustic velocity of wet fine sand)

$n=3$  (attenuation coefficient of wet fine sand)

$f=1$  (coupling factor for all tests, calculated from burial depth of charge 40 cm and the charge weight)

$\alpha$  (40 cm standoff distance)=0.8 (reduction factor)

$\alpha$  (60 cm standoff distance)=0.9 (reduction factor)

$\lambda=0.1$  (ratio of rise time to blast duration)

$T_d$  (40 cm standoff distance)=4 ms (blast duration)

$T_d$  (60 cm standoff distance)=6 ms (blast duration)

$W=0.0105 \text{ kg}$  (in fact, the charge for all tests is 10 g C-4, equivalent to 10.5 g TNT)

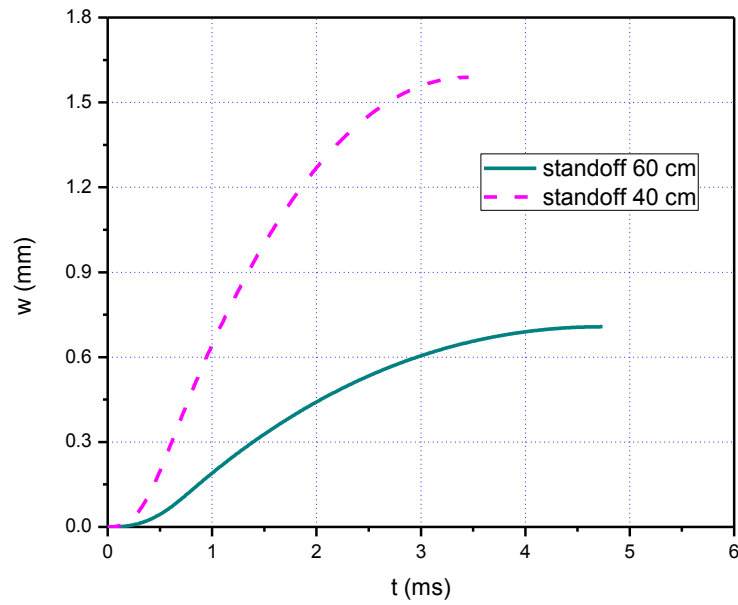
$\frac{R}{W^{1/3}}$  (40 cm standoff distance) =  $1.8267 \text{ m/kg}^{1/3}$  (scaled distance)

$\frac{R}{W^{1/3}}$  (60 cm standoff distance) =  $2.5752 \text{ m/kg}^{1/3}$  (scaled distance)

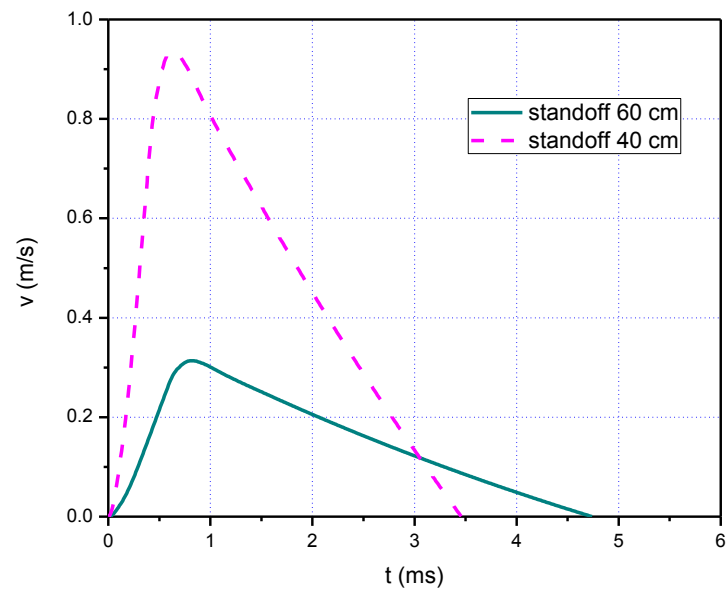
## 6.5 Results and discussion

To compare with the test results, a theoretical case study with the previous formulation is done. The tests are carried out twice for standoff distance 60 cm and once for

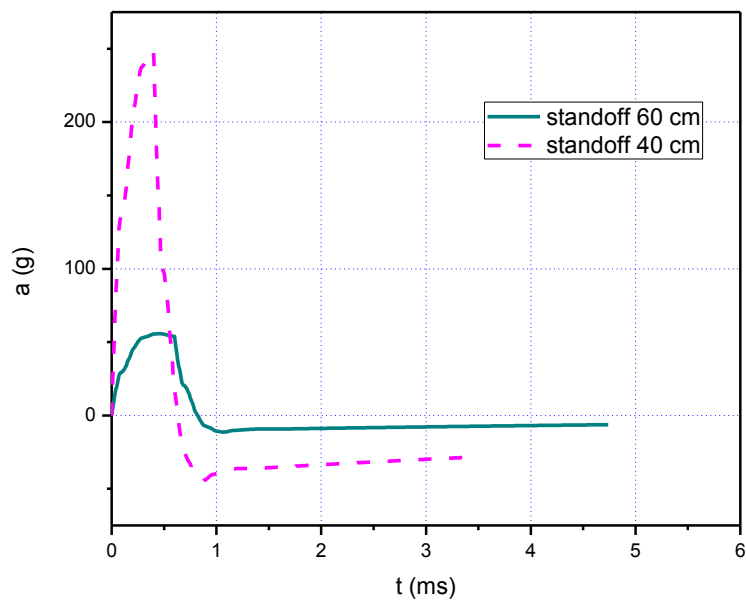
standoff distance 40 cm. Soil density is measured before each test. The acoustic velocity is 200 m/s, regardless of the saturation degree. Therefore, according to TM-5-855-1, the blast duration is 6 ms for 60 cm standoff and 4 ms for 40 cm standoff. In addition, a typical value of attenuation coefficient for fine sand, 3 is used in the theoretical prediction (TM-5-855-1 1986). For the case of standoff distance 40 cm, the average soil density of the two tests,  $1582 \text{ kg/m}^3$  is used. The predicted displacements, velocities and accelerations are indicated in Fig. 6.4.



(a)



(b)



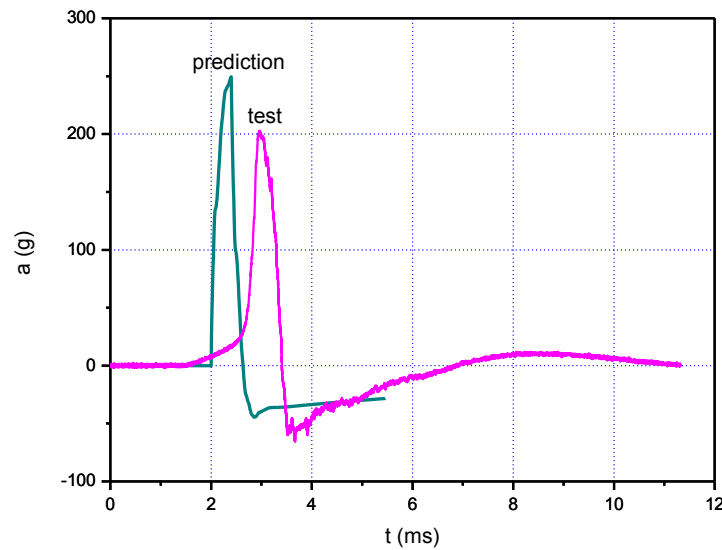
(c)

Fig. 6.4 Predicted response time histories at the mid-span

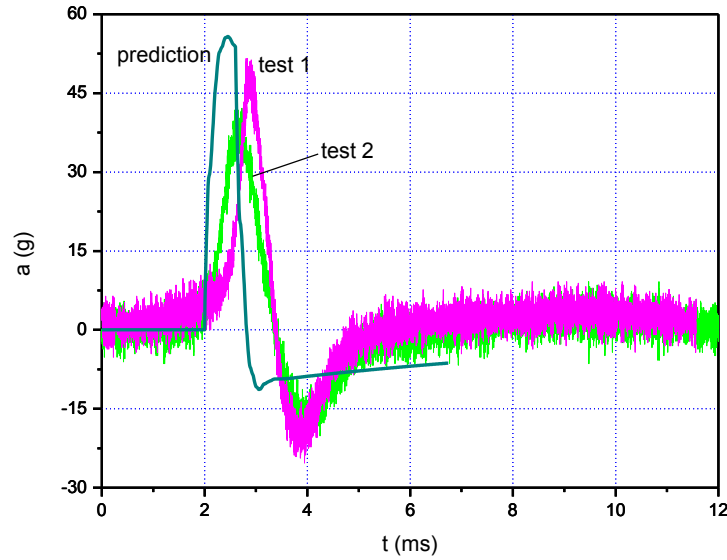
Among the responses, the most important is the acceleration time histories, since it is the excitation to the attached secondary systems. From Fig. 6.4(c), the accelerations only oscillate once, implying that system in the model, consisting of the structural member and the surrounding soil is dominantly over-damped.

It is worth noting that the prediction in the present study is valid until the displacement achieves its peak. Therefore the response time histories with period shorter than the blast duration are presented.

To validate the predictions, the most important time histories- the acceleration time histories, are compared in Fig. 6.5. It is seen that the shape and magnitude of the acceleration time profile are similar. The predicted peak accelerations are higher than that of the tests, for both the cases of 40 cm and 60 cm standoff distances. The underlying mechanism is the rigid body motion of the whole test systems subjected to



(a)



(b)

Fig. 6.5 Comparison of the predicted acceleration time histories with test results: (a) 40 cm standoff distance; (b) 60 cm standoff distance

the soil-transmitted blast load is not considered in the model. In fact, the rigid body motion does exist in the test although its influence is not significant due to the hollowness of the test system and the small mass ratio of the front plate to whole system.

Differences between the predictions and test results do exist. First, the negative parts of the acceleration time histories are under-predicted. Further, the arrival time of the ground shocks are slightly different.

The reason accounting for the difference in arrival time is that in the theoretical prediction, plane wave assumption is adopted. However, in the test, although compared to the dimension of the plate (20 cm by 20 cm), the scaled distance of 40 cm or 60 cm is sufficiently distant, the curvature of the blast does have some effects. Subsequently the real arrival time is different: the mid-span of the plate is firstly loaded then the loading area increases with time from the mid-span to the supports. On the contrary, in



the theoretical prediction, the plane wave applied to the whole plate uniformly at almost the same time when the wave with curvature in the test hits the mid-span. Therefore the major peaks of the tested acceleration time history are relatively later compared to those predicted.

Most importantly, the trends of the predicted acceleration time histories are similar to those of the tests: they do not oscillate, implying the plate is over-damped by the surrounding soil, which is favorably predicted by the model.

To further validate the model, the test strain time history is compared to that of the prediction. In the prediction, the strain time history has the same trend as the displacement time history. From simple calculation based on the strength of materials, they are linked as follows:

$$\varepsilon = \frac{24wh}{5l^2} \quad (6.8)$$

where  $\varepsilon$  and  $w$  are the strain and displacement at the mid-span, respectively.  $l$  is the span and  $h$  is the thickness of the structural member. From Eq. (6.8), the strain time history in fact is the displacement time history multiplied by a constant. Figure 6.6 indicates that the trend and peak value of the predicted strain time history compare favorably with that of the tests.

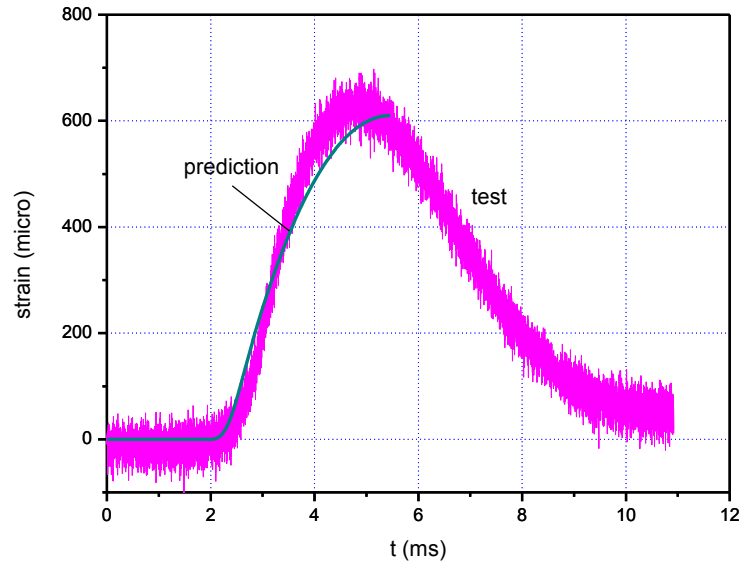


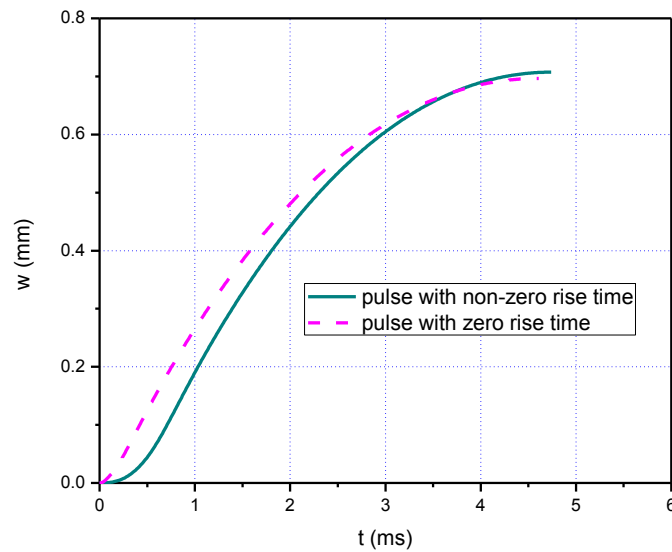
Fig. 6.6 Comparison of the predicted and tested strain time history at the plate center:  
40 cm standoff distance

Based on the acceleration and strain time histories validations, the model in this chapter reasonably predicted the structural responses of underground structures subjected to soil-transmitted loads.

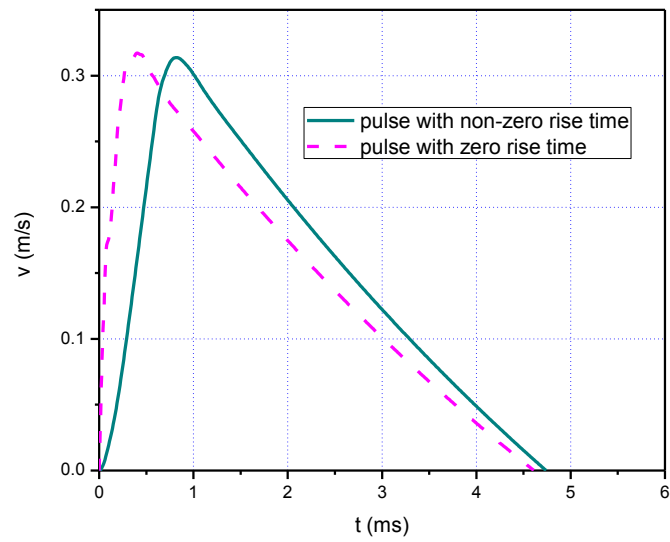
Further, this validated model is used as a benchmark to evaluate the accuracy of previous model. From Eq. (6.1), if  $\lambda$  reduces to zero, the present study reduces to the prediction in Chapter 3. With the same parameters, the two models with and without considering the rise time of the ground shock, are compared in Fig. 6.7. It can be seen that the displacement and velocity time histories are similar although there are some minor differences. The displacement time history for ground shock with zero rise time is higher in the initial stage and achieves peak value slightly earlier. Similarly, the velocity for ground shock with zero rise time also achieves peak value earlier. It is

worth noting that the values of peak displacements and velocities are nearly the same no matter the rise time of the ground shock is considered or not.

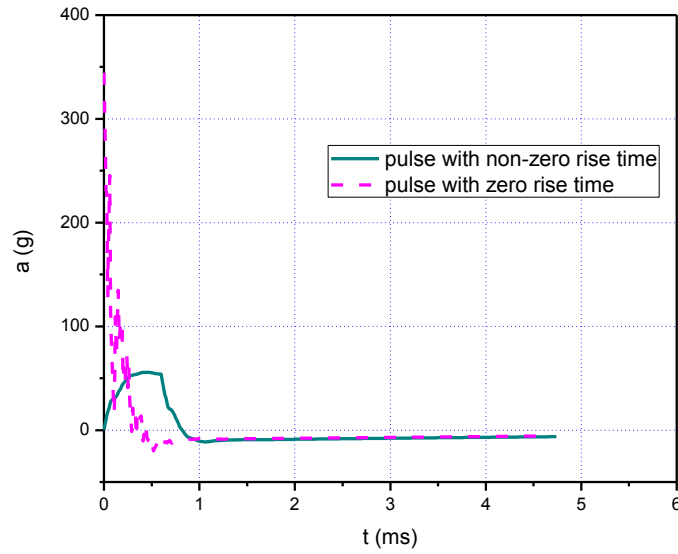
However, from Fig. 6.7(c), the profiles of acceleration time histories at the mid-span are significantly different. Subjected to soil blast with zero rise time, the acceleration achieves its peak at time zero and decreases with time rapidly; in contrast, when the blast rise time is considered, the acceleration is zero initially and has a profile with significantly lower peak value and longer duration. This difference will influence the vibration characteristics of the equipment attached thus should be considered when designing underground facilities.



(a)



(b)



(c)

Fig. 6.7 Comparison of the structural response with and without pulse rise time: 60 cm standoff distance

It should be noted that the acceleration time histories in Fig. 6.7 (c) are the excitations to the attached equipment and devices. To evaluate the shock level experienced by a specific device, shock response spectra are established, as shown in Fig. 6.8. It is interesting that intuitively the shock with zero rise time results in an acceleration time history with significantly higher peak as excitation, which may subsequently lead to severe shock level to the equipment. However, in the present case study, the max acceleration on the device by soil blast with non-zero rise time is higher, which is not as expected. In fact, Fig. 6.7 (c) reveals the underlying mechanism: when subjected to soil blast with zero rise time, the acceleration peak is significantly higher, but the shock duration is shorter than 0.5 ms. In contrast, when subjected to soil blast with non-zero rise time, the acceleration excitation peak is relatively lower, but the duration is longer, almost 1 ms. The difference in the shock duration significantly influences the responses of the attached equipment: the device and support of higher natural frequency should be effectively excited by the pulse with zero blast rise time while the responses induced by non-zero rise time should be larger for device and support of relatively lower natural frequency. According to the trends of the curves, the two curves may intersect at certain frequency higher than 1000 Hz, after which the shock level by blast with zero rise time should be higher. However, in practical range of devices with support, i.e. 1 Hz to 1000 Hz, the shock level on equipment by pulse with non-zero rise time is higher.

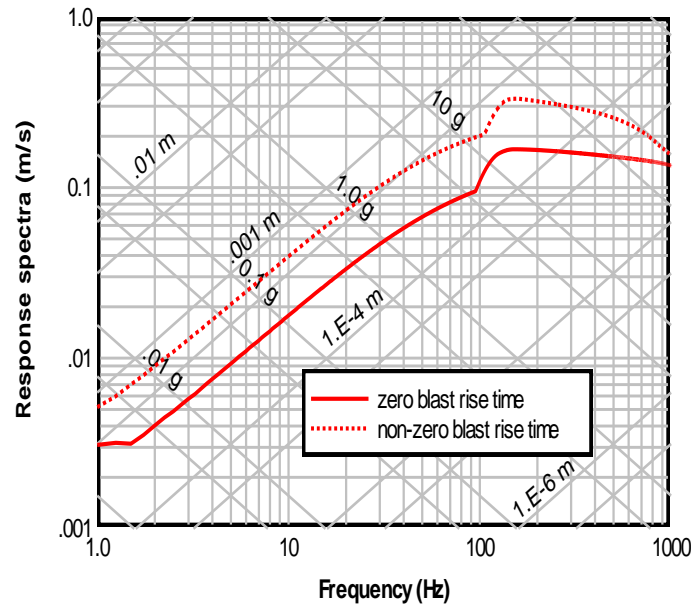


Fig. 6.8 Response spectra comparison of soil blast with zero and non-zero blast rise time

## 6.6 Summary

The in-structure shock of underground facilities is theoretically investigated with the soil blast rise time taken into consideration. A small scale test is designed and conducted to validate the theory prediction. When the scaled model of the underground structure is installed in wet fine sand and subjected to a soil-transmitted blast induced by a small scale subsurface detonation, the acceleration time history favorably compare with the analytical prediction. The peak accelerations of the prediction are slightly higher than that of the tests and the acceleration profiles are reasonably predicted. Further validation of the model is made by comparing the strain of the mid-span to prediction. With this model in this chapter as benchmark, the previous used model with zero blast rise time is calibrated. It is found that the displacement and velocity are similar but the profile of acceleration time history is significantly different. In the practical range of devices with support, i.e. 1 Hz to 1000 Hz, the shock level on

equipment by blast with non-zero rise time is higher. The prediction proposed can be used as a supplement to the design code TM-5-855-1.

## **6.7 Acknowledgment**

The author wishes to appreciate the generous help provided by Prof. Beppu, National Defense Academy, Japan. Due to the usage constraint of explosives in Singapore, experiment related to blast load cannot be done freely. Once I designed the small scaled experiment to validate the analytical prediction, Prof. Beppu helped me to conduct the test in National Defense Academy, Japan. He and his students constructed the test set-up including installing the explosives, pressure sensors, accelerometers, strain gauges as well as backfilling fine sands several times, which are extremely time-consuming. After the test, Prof. Beppu also conducted the data filtering before sending them to me. I am indebted to him for the generous help.

## **7 METAL FOAM CLADDING SUBJECTED TO A LOCALIZED BLAST: A THEORETICAL APPROACH**

### **7.1 Introduction**

To protect key buildings from accidental and terrorist explosions, a conventional method is to strengthen them with thicker and stronger structural members. However, the strengthening is expensive, labor-intensive and time-consuming in construction and retrofit; further, for the same detonation and standoff distance, the blast loads experienced by the strengthened structures of greater rigidity are higher than those of un-strengthened ones. Alternatively, attaching blast mitigation cladding with cellular material core to protect structures as a blast alleviation philosophy has emerged (Ashby et al. 2000). Generally, cellular materials and structures undergo large plastic deformation in relatively low stress level under compression, showing great potential to be used in blast mitigation. In recent years, the dynamic properties of cellular materials and response of structures with cellular material components under blast load were intensively studied (Lu and Yu 2003; Gibson and Ashby 1997; Reid and Peng 1997; Deshpande and Fleck 2005; Lopatnikov et al. 2005; Tan et al. 2005a, b; Ma and Ye 2007a, b; Ye and Ma 2007; Zhu et al. 2009; Harrigan et al. 2010) experimentally, analytically and numerically. Various models delineating the dynamic behaviors of cellular solids were proposed. Amongst, the rigid-perfectly-plastic-locking model using shock theory predicts response of metal foam under high velocity crushing with adequate accuracy and can be analytically formulated in an explicit manner thus was widely applied.

Cellular material and structures can be roughly categorized as honeycombs, lattice structures and metal foams. Further, the studied metal foam cladding response under blast load can be categorized into two major groups. In the first group, the face sheet of the cladding is assumed rigid, not dissipating energy during crushing. In addition, the



explosion is assumed sufficiently distant so that the load is almost uniformly distributed on the face sheet, where the structure, load and response are essentially one-dimensional (Reid and Peng 1997; Lopatnikov et al. 2005; Ma and Ye 2007a, b; Ye and Ma 2007; Harrigan et al. 2010). The merit of this idealization is time history of the cladding response can be readily obtained in close form, allowing for convenient parametric study and key parameter identification, thus the response mechanism is revealed explicitly. However, the drawback is also obvious: for a typical spherical explosion, the uniformly distributed load implies the event should be sufficiently distant thus the model cannot be used for a close range detonation; further, the boundary condition of the cladding is not considered; last, the energy dissipation by the face sheet is completely ignored, leading to an overly conservative prediction.

The other group contains, in contrast, two-dimensional models such as sandwich beams and plates with metal foam cores (e.g. Zhu et al. 2009). By assuming deflection fields, response time history can be derived in one or more phases; or by adopting energy method, the final deformation state can be directly determined. In fact, by assuming deformed shapes of the claddings, the two-dimensional problems are reduced to essentially one-dimensional. The advantage of these models is that close range blast can be studied and the energy dissipation by the face sheet can be taken into consideration. However, almost all of the claddings or just a single metal face sheet examined are clamped or simply supported (Wang 1954; Symonds and Wierzbicki 1979; Jones 1989; Wierzbicki and Nurick 1996; Xue and Hutchinson 2003; Fleck and Deshpande 2004; Qiu et al. 2005; Gharababaei and Darvizeh 2010). With these boundaries, the extent of the bulge formed from the originally flat face sheet is prescribed as the beam span or plate diameter. Due to the relatively small dimensions of the beams or plates used in experiment, no matter the loads are applied on the whole face sheet or only on a patch, the face sheets and claddings always exhibit global deformations.

In engineering practice, when a metal foam cladding attached to a structural member is subjected to a close range detonation, the bulge extent and depth depend on both the

load and cladding properties, are no longer prescribed. Therefore in the present study, a relatively realistic situation for a real-sized cladding subjected to a close range spherical airburst is considered through releasing the boundary condition addressed above. The metal foam cladding is directly attached to the protected structure, which is assumed to be rigid and not move. Compared to the localized area on which the blast load exerted induced by the close range detonation, the whole cladding is relative large and can be treated as infinite. More importantly, the extent of the bulge is no longer pre-defined, it depends on the blast load distribution as well as the cladding parameters such as the foam plateau stress. It is evident that a close range spherical explosion will impose an axisymmetrical load on the face sheet, resulting in an axisymmetrical bulge with largest transverse deflection in the center. By assuming a deflection profile and adopting energy method, the bulge extent and depth are determined without analyzing the crushing time history. Subsequently the densified foam thickness is obtained, which can be used as a preliminary design for a protective cladding.

## **7.2 Determination of the bulge**

### **7.2.1 Deformation profile of the face sheet**

For a close range airburst of a spherical charge, the shock wave effect is included and the debris striking is excluded, the perforation of the face sheet is not considered in the bulging process. When a cladding consisting of a face sheet and a layer of metal foam is subjected to a close range detonation, indicated in Fig. 7.1, the face sheet and foam will undergo deformation. The bulge shape can be approximated by various functions based on the observation of different bulge depths (Jones 1989), shown in Fig. 7.2. For instance:

$$w(r) = W_0 \left[ 1 - \left( \frac{r}{\eta} \right)^\alpha \right] \quad (7.1)$$

where  $W_0$  and  $\eta$  are the depth and extent of the bulge, respectively. Profiles with  $\alpha=1$  or 2 are often used for plates whose maximum deflection is less than half the plate thickness (Jones 1989), where the deformation is dominated by bending and plastic hinges while the membrane force is negligibly small and ignored.

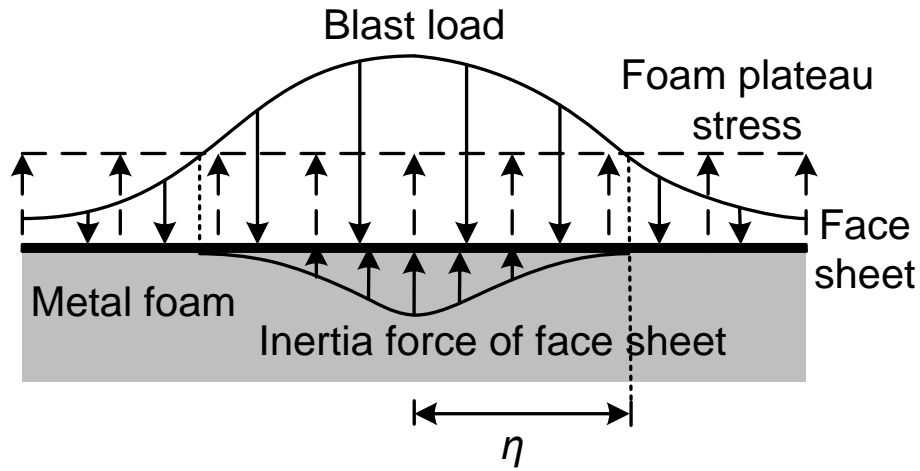


Fig. 7.1 Determination of the bulge extent

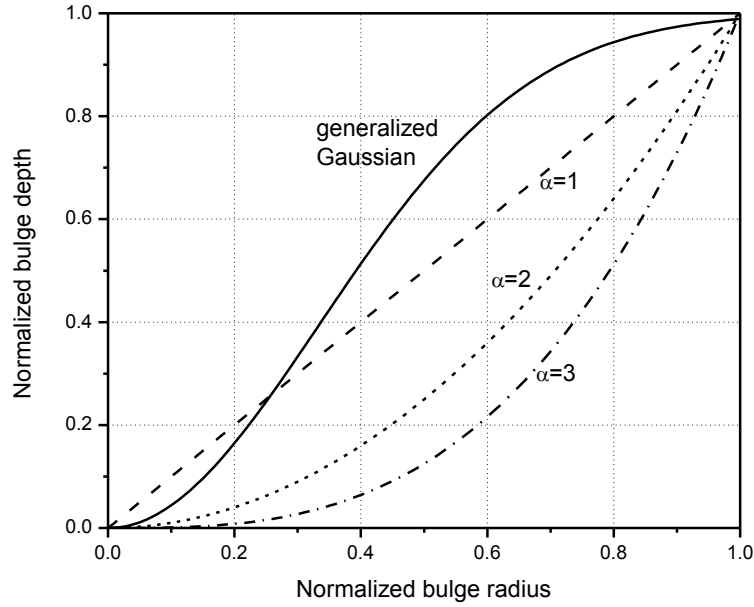


Fig. 7.2 Pre-defined deformation profiles of thin plates

When the maximum deflection is much greater than half the plate thickness, the bulging process is dominated by membrane force and the contribution from bending is relatively smaller and can be neglected (Jones 1989). Then it is not clear whether these deformation profiles in Eq. (7.1) are still reasonable. Based on the observation of the bulge profiles of thin metal plates (ratio of diameter to thickness about 33, clamped) subjected to close range impulsive loads and undergoing large deformation (Gharababaei and Darvizeh 2010), as expected, the rotation at the bulge center is zero. Thus a requirement for a reasonable bulge shape is the rotation at the bulge center should be zero. Further, for large deflection of a thin plate subjected to a localized blast load, the deformation is dominated by in-plane membrane stretching, the transition region around the bulge periphery should be smooth without sharp corner and the rotation at the periphery of the bulge should be near zero. From Fig. 7.2, it is evident

that the bulge shapes delineated by  $w(r) = W_0 \left[ 1 - \left( \frac{r}{\eta} \right)^\alpha \right]$  are not suitable for approximating the bulge in the present study since although the zero center rotation is satisfied, there are sharp corners around the bulge periphery. However, the generalized Gaussian function (refer to Eq. (7.11)) satisfies all the requirements. Another characteristic for large deformation of thin plate subjected to a localized blast is the pulse at the center is further strengthened due to the large central plate deformation thus the bulge around the center is even deeper. The generalized Gaussian function also exhibits the capability to represent this effect thus is adopted to approximate the bulge shape when the maximum deflection is much greater than half the face sheet thickness. In the present study, the face sheet deformation time history is simplified by decoupling the bulge shape from time:  $w(r, t) = W(r)T(t)$ , where  $W(r)$  is a generalized Gaussian function with respect to bulge radius and  $T(t)$  is a function of time.

### 7.2.2 Determination of the bulge extent

For mass efficiency, generally the face sheet of protective claddings is thin, with thickness ranging from less than 1 millimeter to several millimeters (Zhu et al. 2009). Due to the small standoff distance from the detonation to the cladding and the small face sheet thickness, the bulge depth is always much greater than half the face sheet thickness. According to Jones (Jones 1989), for a thin plate, bending moment does not contribute to the energy dissipation when the transverse displacement is larger than half the plate thickness. For sufficiently large transverse displacement of a circular plate, the influence of bending moment may be entirely neglected and the response is solely controlled by membrane force. In addition, for large plastic deflection of a thin plate, the contributions from elasticity, either in initial pre-yield stage or in unloading spring-back, are negligibly small compared to that of plastic deformation (Jones 1989). Therefore in the current study, the face sheet is idealized as a rigid plastic membrane, in which the shear force is also neglected due to the small face sheet thickness.

Consider a blast mitigation cladding, consisting of a thin metal face sheet and a layer of metal foam, protecting structures against impulsive loads. When it is subjected to a blast, to predict the bulge depth with energy method, first the bulge extent should be determined. Generally a load induced by a close range airburst lasts for an extremely short duration, in the order of several microseconds to one millisecond with a sharp increase and a rapid decrease (Smith and Hetherington 1994). The size of the bulge can be determined by analyzing the load applied on, and resistance from the cladding, shown in Fig. 7.1.

Define the nearest point in the face sheet from the explosion prior to deformation as coordinate origin and downward direction is positive. It is evident both the blast load distribution and bulge profile are functions of radius thus it is essentially an axisymmetrical problem. The load applied on the cladding is:

$$p(r,t) = p_c e^{-\frac{r^2}{2b^2}} \left( 1 - \frac{t}{T_d} \right) \quad (7.2)$$

where  $p_c$  is the peak load and  $b$  is characteristic size of the round loading area in a sense that at  $3b$  the loading intensity is 1% of that at the origin.  $T_d$  is the blast duration. Based on the observation that the blast load perpendicularly applied to the cladding with incidence angle, defined as the sharp angle between the wave front and the cladding, greater than 70 degree is negligibly small and can be ignored (TM-5-855-1 1986), the major affected region of the spherical airburst on the face sheet is a round area with radius  $3b$ , where  $b=R$ , the standoff distance between the charge center and cladding.

When metal foam is crushed rapidly, the densification stress at the foam shock front is (Reid and Peng 1997; Ashby et al. 2000; Lu and Yu 2003):

$$\sigma_D = \sigma_{pl} + \frac{\rho_f}{\varepsilon_D} v^2 \quad (7.3)$$

where  $\sigma_{pl}$  is the foam plateau stress, a property determined by relative density, constant.  $\rho_f$  is the foam density before crushing and  $\varepsilon_D$  is the foam densification strain.  $v$  is the crushing velocity.

From Eq. (7.3), it is clear that the densification stress at the shock front consists of two parts: the plateau stress of the foam and the dynamic resistance induced by the high velocity foam crushing, which are quasi-static and dynamic in nature, respectively. In particular, the second item of the right-hand side of Eq. (7.3) is termed as dynamic enhancement, whose physical nature is similar to the dynamic pressure induced by a flow in the field of fluid dynamics. It is worth noting that due to the strain rate effect of materials, the foam plateau stress under dynamic load is higher than that under quasi-static load. In the thesis, this strain rate effect is not considered since the typical metal foam in engineering application is made from aluminum, a typical material insensitive to strain rate effect.

At the instant when the blast load arrives, the deformation and velocity of the face sheet is zero, thus the dynamic enhancement of the metal foam is zero. According to D'Alembert's principle, within the bulge extent, the total blast load applied on the cladding should be equal to the sum of the inertia force of the face sheet and the resistance from the metal foam: the plateau stress, indicated in Fig. 7.1. At the bulge periphery, the deflection, velocity and acceleration are constantly zero, resulting in no inertia force at the bulge boundary. Then by equating the load applied to the foam plateau stress, the extent of the bulge is determined:

$$p_c e^{-\frac{r^2}{2b^2}} = \sigma_{pl}, \quad r = \eta \quad (7.4)$$

The bulge extent is:

$$\eta = \sqrt{2}b \sqrt{\ln \frac{p_c}{\sigma_{pl}}} \quad (7.5)$$

where  $\sigma_{pl}$  is the foam plateau stress. It is evident that the bulge is a round area and according to the rigid plastic assumption, the cladding of radius greater than  $\eta$  is undeformed, where the load does not contribute to the bulging. Subsequently, the load on cladding is truncated at the extent periphery and only the part within the extent contributes to the bulging process.

### 7.2.3 Determination of the bulge depth

Once the bulge extent of the cladding is predicted, the bulge depth can be determined using energy method. As stated in the preceding section, the region with radius greater than  $\eta$  will not be examined since although load applies, this region does not undergo deformation. The duration for a typical near-field explosion is generally much less than 1 millisecond, significantly shorter than the structural response time. It is reasonable to assume the impulse is imparted to the face sheet immediately before any deformation occurs (Zhu et al. 2009). The response of the metal foam cladding is divided into two sequential phases (similar phase division can be found in Zhu et al. 2009): Phase I: air-structure interaction during the blast event, resulting in an initial velocity field of the face sheet when no deformation occurs; Phase II: retardation of the cladding to rest by plastic stretching of the face sheet and the resistance from the foam crushing.

#### *Energy imparted to the cladding*

Take the cladding within the bulge extent to analyze. The impulse imparted into the face sheet is:

$$I = \int_A \int_0^{T_d} p_c e^{-\frac{r^2}{2b^2}} \left( 1 - \frac{t}{T_d} \right) dt dA = \pi T_d p_c b^2 \left( 1 - e^{-\frac{\eta^2}{2b^2}} \right) \quad (7.6)$$



The face sheet is assumed to obtain a velocity field with generalized Gaussian distribution (Ramu and Iyengar 1976; Kennedy and Iyengar 1981):

$$v_0(r) = V_0 e^{-\frac{r^2}{2c^2}}, \quad r \leq \eta \quad (7.7)$$

where  $V_0$  is the velocity at the bulge center and  $c$  is the characteristic size of the bulge. At  $\eta=3c$ , the velocity is 1% of  $V_0$  and considered as zero. The initial momentum of the face sheet is:

$$\Delta MV = \int_A V_0 e^{-\frac{r^2}{2c^2}} \rho_b h_b dA = 2\pi V_0 \rho_b h_b c^2 \left(1 - e^{-\frac{\eta^2}{2c^2}}\right) \quad (7.8)$$

According to the impulse-momentum relation, the initial velocity at the bulge center is determined by equating the imparted impulse to the initial momentum of the face sheet:

$$V_0 = \frac{T_d p_c b^2 \left(1 - e^{-\frac{\eta^2}{2b^2}}\right)}{2\rho_b h_b c^2 \left(1 - e^{-\frac{\eta^2}{2c^2}}\right)} \quad (7.9)$$

Subsequently, the energy imparted to the face sheet is:

$$E_k = \int_A \frac{1}{2} [v(r)]^2 dm = \frac{\pi}{2} V_0^2 \rho_b h_b c^2 \left(1 - e^{-\frac{\eta^2}{2c^2}}\right) = \frac{\pi T_d^2 p_c^2 b^4 \left(1 - e^{-\frac{\eta^2}{2b^2}}\right)^2 \left(1 + e^{-\frac{\eta^2}{2c^2}}\right)}{8\rho_b h_b c^2 \left(1 - e^{-\frac{\eta^2}{2c^2}}\right)} \quad (7.10)$$

This kinetic energy of the face sheet will be dissipated by foam core crushing and face sheet stretching.

*Energy dissipated by foam and face sheet*

As discussed in the preceding section, the bulge shape is approximated by a generalized Gaussian function:

$$w(r) = W_0 e^{-\frac{r^2}{2c^2}} \quad (7.11)$$

During the cladding crushing, the resistance to the face sheet and densified foam varies since although the plateau stress remains constant, the dynamic enhancement related to the crushing velocity changes from the initial peak value to zero monotonically. The work done by the foam to resist the crushing of the face sheet and crushed foam can be divided into two parts: one is from the plateau stress and the other is from the dynamic enhancement. Amongst, the part of energy related to the ever-changing dynamic enhancement is difficult to quantify exactly. To calculate the energy absorbed by foam, first consider a one-dimensional (1-D) cladding with foam core subjected to a high velocity crushing of the face plate with an initial velocity  $V_0$ . The foam resistance to the system consisting of the face plate and crushed foam is (Ashby et al. 2000):

$$\sigma_D = \sigma_{pl} + \frac{\rho_f}{\varepsilon_D} \frac{\rho_b h_b V_0^2 - 2\sigma_{pl} u}{\rho_b h_b + \rho_f u / \varepsilon_D} \quad (7.12)$$

where  $u$  is the face sheet displacement.  $\rho_b$  and  $h_b$  are the density and thickness of the face sheet. The first term is foam plateau stress and the second term is the dynamic enhancement. From Eq. (7.12), the crushing resistance decreases with the increase of the crushed distance. Therefore in the initial stage of the crushing, the crushing velocity is relatively higher, then the dynamic enhancement is stronger, thus the deceleration is stronger and the crushing velocity decreasing rate is relatively higher; on the contrary, in the late stage of crushing, the relatively lower crushing velocity leads to weaker dynamic enhancement, thus the deceleration is relatively smaller, subsequently the crushing velocity decreasing rate is relatively lower, as indicated in Fig. 7.3 (the velocity square, directly proportionate to the dynamic enhancement, instead the velocity itself, is shown).

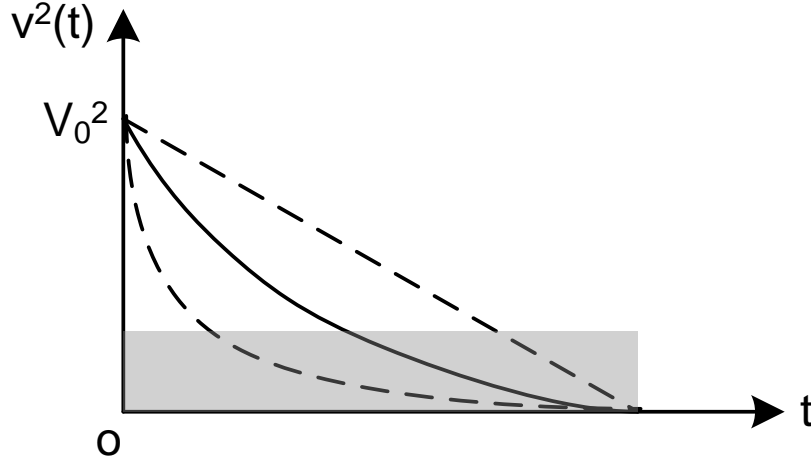


Fig. 7.3 Energy dissipation by the foam dynamic enhancement with respect to time (1-D crushing is assumed)

Consider another 1-D crushing process with the same initial and final conditions. However the dynamic enhancement is assumed to be constant throughout the crushing, where a parameter  $\beta$  is introduced to describe the average dynamic enhancement:

$$\sigma_{Dd} = \frac{\rho_f}{\varepsilon_D} \beta V_0^2 \quad (7.13)$$

For higher face sheet initial velocity,  $\beta$  should be relatively smaller compared to that with lower initial velocity. In other words, the higher the percentage of the dynamic enhancement to the total foam resistance against crushing, the smaller is  $\beta$ .

From Eqs. (7.3) and (7.12), the final length of the crushed foam is obtained when the velocity becomes zero:

$$u_{\max} = \frac{\rho_b h_b V_0^2}{2\sigma_{pl}} \quad (7.14)$$

During the entire crushing process, the work done by the dynamic enhancement is:

$$W_R = \int_0^{u_{\max}} \frac{\rho_f}{\varepsilon_D} \frac{\rho_b h_b V_0^2 - 2\sigma_{pl} u}{\rho_b h_b + \rho_f u / \varepsilon_D} dl = \rho_b h_b \left[ -V_0^2 + \left( V_0^2 + \frac{2\sigma_{pl} \varepsilon_D}{\rho_f} \right) \ln \left( 1 + \frac{\rho_f V_0^2}{2\sigma_{pl} \varepsilon_D} \right) \right] \quad (7.15)$$

Then equate this work to that done by the constant dynamic enhancement in Eq. (7.13),  $\beta$  is determined:

$$\beta = \frac{2\sigma_{pl} \varepsilon_D}{\rho_f V_0^4} \left[ -V_0^2 + \left( V_0^2 + \frac{2\sigma_{pl} \varepsilon_D}{\rho_f} \right) \ln \left( 1 + \frac{\rho_f V_0^2}{2\sigma_{pl} \varepsilon_D} \right) \right] \quad (7.16)$$

From Eq. (7.16), the parameter  $\beta$  depends on the initial velocity of the face sheet, the density, plateau stress and densification strain of the foam, but independent of the density and thickness of the face sheet.

It should be noted that this  $\beta$  is for 1-D foam crushing. When it comes to 2-D cladding as the case of close range airburst, the initially gained kinetic energy of the face sheet is dissipated not only by foam crushing, but also by face sheet stretching. Recall the resistance against crushing consists of the plateau stress and dynamic enhancement in 1-D crushing, with the face sheet stretching taken into consideration, the dynamic resistance of the cladding systems consisting of the face sheet and foam is:

$$\sigma_D = \sigma_{str} + \sigma_{pl} + \frac{\rho_f}{\varepsilon_D} v^2 \quad (7.17)$$

where  $\sigma_{str}$  is the resistance contribution induced by the face sheet stretching, in the direction perpendicular to the initial face sheet. It is evident that the percentage of foam dynamic enhancement to total crushing resistance is lower than the case in 1-D when the same face sheet initial velocity (for 2-D cladding, the velocity refers to that in the bulge center) is considered, resulting in a larger  $\beta$ . Further, based on the initial velocity profile of the face sheet, the velocity is highest at the center and gradually decreases to zero at the bulge periphery. Therefore  $\beta$  is smallest at the center and monotonically increases with radius. In the present study, the  $\beta$  value in 1-D crushing without face sheet stretching is used based on the two considerations above, leading to less energy

dissipated by dynamic enhancement and a conservative prediction with a deeper bulge. The effect of  $\beta$  will be discussed in the following section. The total energy dissipated by the foam during crushing is:

$$\begin{aligned}
 E_f &= \int_A \frac{1}{2} \left[ \sigma_{pl} + \sigma_{pl} + \frac{\rho_f}{\varepsilon_D} \beta v_0^2(r) \right] \varepsilon_D \left[ \frac{w(r)}{\varepsilon_D} \right] dA \\
 &= 2\pi c^2 \sigma_{pl} W_0 \left( 1 - e^{-\frac{\eta^2}{2c^2}} \right) + \frac{\pi}{3} \beta \frac{\rho_f}{\varepsilon_D} c^2 V_0^2 W_0 \left( 1 - e^{-\frac{3\eta^2}{2c^2}} \right)
 \end{aligned} \tag{7.18}$$

Amongst, the first part of the energy is dissipated by the foam plateau stress, corresponding to the energy dissipated by quasi-static crushing, calculated as quasi-static plastic strain energy per unit volume times the crushed foam volume:

$$E_{fpl} = (\sigma_{pl} \varepsilon_D) \int_A \frac{w(r)}{\varepsilon_D} dA = 2\pi W_0 c^2 \sigma_{pl} \left( 1 - e^{-\frac{\eta^2}{2c^2}} \right) \tag{7.19}$$

which is exactly the same as the first term of Eq. (7.18). According to Teeling-Smith and Nurick (1991), the plastic strain energy for a rigid-plastic thin plate with an axisymmetrical bulging is:

$$E_{str} = h_b \int_0^{2\pi} \int_0^\eta \frac{1}{2} \frac{\sigma_{yd}}{\sqrt{1-\nu+\nu^2}} \left( \frac{dw}{dr} \right)^2 r dr d\theta = \frac{\pi h_b \sigma_{yd} W_0^2}{2\sqrt{1-\nu+\nu^2}} \left[ 1 - e^{-\frac{\eta^2}{c^2}} \left( 1 + \frac{\eta^2}{c^2} \right) \right] \tag{7.20}$$

where  $\sigma_{yd}$  and  $\nu$  are the dynamic yield strength and Poisson's ratio of the material of which the face sheet is made, respectively.

#### *Determination of the bulge depth*

By equating the energy dissipated by the face sheet stretching and dynamic foam crushing to the kinetic energy imparted to the face sheet,

$$E_k = E_{str} + E_f \tag{7.21}$$

The governing equation for the bulge depth is:

$$\begin{aligned} \frac{1}{2}V_0^2\rho_b h_b c^2 \left(1 - e^{-\frac{\eta^2}{c^2}}\right) &= \frac{h_b \sigma_{yd} W_0^2}{2\sqrt{1-\nu+\nu^2}} \left[1 - e^{-\frac{\eta^2}{c^2}} \left(1 + \frac{\eta^2}{c^2}\right)\right] + 2c^2 \sigma_{pl} W_0 \left(1 - e^{-\frac{\eta^2}{2c^2}}\right) \\ &+ \frac{1}{3}\beta \frac{\rho_f}{\varepsilon_D} c^2 V_0^2 W_0 \left(1 - e^{-\frac{3\eta^2}{2c^2}}\right) \end{aligned} \quad (7.22)$$

In short term,

$$AW_0^2 + BW_0 + C = 0 \quad (7.23)$$

where

$$\begin{aligned} A &= \frac{h_b \sigma_{yd}}{2\sqrt{1-\nu+\nu^2}} \left[1 - e^{-\frac{\eta^2}{c^2}} \left(1 + \frac{\eta^2}{c^2}\right)\right] \\ B &= 2c^2 \sigma_{pl} \left(1 - e^{-\frac{\eta^2}{2c^2}}\right) + \frac{1}{3}\beta \frac{\rho_f}{\varepsilon_D} c^2 V_0^2 \left(1 - e^{-\frac{3\eta^2}{2c^2}}\right) \\ C &= -E_k = -\frac{1}{2}V_0^2 \rho_b h_b c^2 \left(1 - e^{-\frac{\eta^2}{c^2}}\right) \end{aligned}$$

$$V_0 = \frac{T_d p_c b^2 \left(1 - e^{-\frac{\eta^2}{2b^2}}\right)}{2\rho_b h_b c^2 \left(1 - e^{-\frac{\eta^2}{2c^2}}\right)}$$

where  $V_0$  is given in Eq. (7.9), rewritten here for convenient reference. The bulge depth is (another solution of Eq. (7.23) is negative and discarded):

$$W_0 = \frac{-B + \sqrt{B^2 - 4AC}}{2A} \quad (7.24)$$

### 7.3 Discussions with a case study

Before discussing the cladding response subjected to a close range explosion, the selection of metal foam core, which is a practical problem in design, is addressed first. The product of foam plateau stress and densification strain equals to the energy absorbed per unit volume, or the specific strain energy. On one hand, for a specific blast, to minimize the foam thickness, the foam specific energy should be as high as possible. With the empirical formulas for plateau stress and densification strain of a foam material (Ashby et al. 2000), the specific energy is:

$$W_s = \sigma_{pl} \varepsilon_D = C_1 \sigma_{ys} \left( \frac{\rho_f}{\rho_s} \right)^{\frac{3}{2}} \left( 1 - \lambda \frac{\rho_f}{\rho_s} \right) \quad (7.25)$$

where  $C_1$  is a constant, 0.3 for aluminum foam;  $\rho_f$  and  $\rho_s$  the foam and solid material densities, respectively;  $\sigma_{ys}$  the yield strength of the solid material, 200 MPa for aluminum;  $\lambda$  a constant, taken as 1.5 (Ashby et al. 2000). According to Eq. (7.25), the specific energy of a foam material depends only on the relative density, indicated in Fig. 7.4. Generally, only metal foam with relative density lower than 0.3 exhibits exceptional properties and is used in energy absorption (Gibson and Ashby 1997). Therefore in application, the specific energy increases monotonically with relative density. To maximize volume efficiency, the foam should be as dense as possible provided that the relative density is less than 0.3. On the other hand, for a structure protected by a metal foam cladding, the transmitted load from the foam, equal to the plateau stress, should be lower than the structure tolerance. Finally, the foam should be selected in a balance: it should have a plateau stress just below the structure tolerance so that for a blast, the foam thickness is minimized and at the same time, the protected structure is not overloaded.

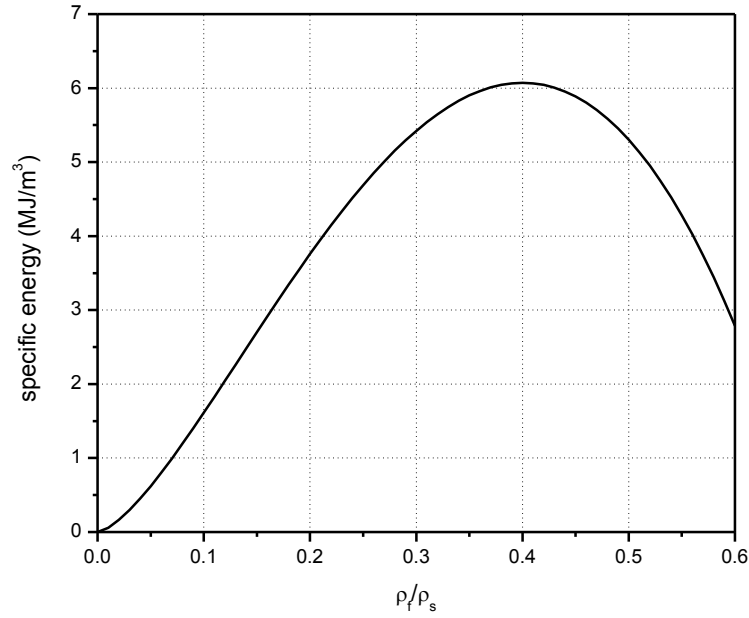


Fig. 7.4 Relation between the specific energy of aluminum foam and its relative density

With Eq. (7.5) and Eq. (7.24), when the close range airburst and cladding parameters are known, the procedure for determining the bulge extent and depth is straightforward. First the blast load exerted on the cladding is calculated with empirical formulas (e.g. Smith and Hetherington 1994; Henrych 1979). Then the bugle extent is obtained through applying Eq. (7.5). Subsequently, the bulge depth can be predicted with Eq. (7.24). Finally, the bulge depth divided by the foam densification strain yields the minimum foam thickness for mitigating this specific close range airburst. It should be noted that when the foam of entire thickness is completely densified, the load transmitted to the protected structure will increase dramatically, even higher than that applied on the cladding (Ye and Ma 2007). Therefore in practical design, this situation should be avoided: for a typical possible blast event, the thickness of the metal foam core should be larger than the calculated crushing foam thickness, rather than the bulge depth.



According to the property of generalized Gaussian function and convention of the characteristic bulge dimension:  $\eta=3c$ . The constants in Eq. (7.23) can be further simplified with adequate accuracy (error less than 1%) as follows:

$$A = \frac{h_b \sigma_{yd}}{2\sqrt{1-\nu+\nu^2}} \quad (7.26a)$$

$$B = 2c^2 \left( \sigma_{pl} + \frac{\beta}{6} \frac{\rho_f}{\varepsilon_D} V_0^2 \right) \quad (7.26b)$$

$$C = -E_k = -\frac{1}{2} V_0^2 \rho_b h_b c^2 \quad (7.26c)$$

$$V_0 = \frac{T_d p_c b^2 \left( 1 - e^{-\frac{\eta^2}{2b^2}} \right)}{2\rho_b h_b c^2} \quad (7.26d)$$

Then the bulge depth can be more readily calculated.

A fundamental requirement for a prediction of a structural response is that it should be able to demonstrate some special cases of the structural behavior even without detailed calculation. Two such special cases are examined: first, if the yield strength of the face sheet approaches infinity, from Eq. (7.23) through Eq. (7.26), the bulge depth approaches zero; further, if the peak blast load is relatively small, i.e. slightly higher than the foam plateau stress, from the same equations, the bulge depth is close to zero. These two special cases are reasonably represented, which validates the prediction to some degree.

Typically, the thickness of the face sheet of a protective cladding is small, always not greater than several millimeters, where the bending and shear resistance around the bulge periphery is negligibly small and ignored. However, if the face sheet is relatively thick, with Eq. (7.5), the bulge extent will be overestimated due to the ignorance of the face sheet bending and shear. Then the face sheet cannot be treated as a rigid plastic

membrane and a refined analysis is required, which is out of the scope of the present study.

From Eq. (7.5), the non-dimensional bugle extent is:

$$\frac{\eta}{R} = \sqrt{2} \sqrt{\ln \frac{p_c}{\sigma_{pl}}} \quad (7.27)$$

recall  $R$  is the standoff distance between the explosion and face sheet. It can be seen that for a specific foam core, the non-dimensional bulge extent increases with the peak load in a decreasing rate, shown in Fig. 7.5. The reason is both the square root function and the logarithm function increase with independent parameter in a decreasing rate respectively and the non-dimensional bulge extent is a compound of these two functions. To create a larger bulge extent, a peak load increasing dramatically in a nonlinear way is required. For instance, with the same standoff distance and foam plateau stress, if the bulge radius is doubled, the peak load should be 55 times the original value.

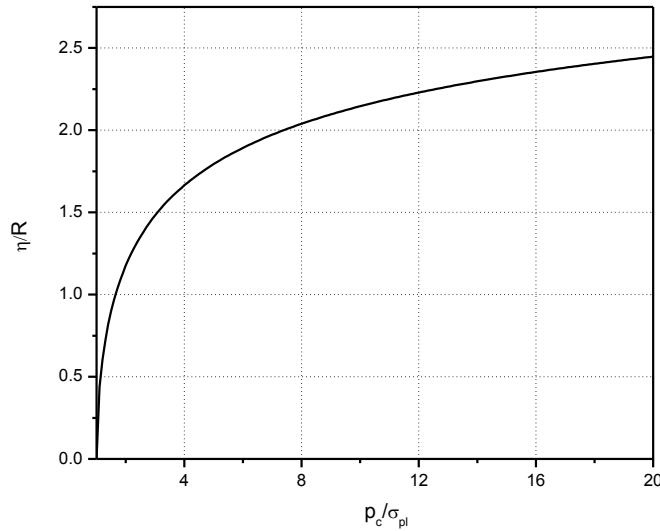


Fig. 7.5 Relation between the non-dimensional bugle extent and peak load

It is also worth noting that Eq. (7.5) and Eq. (7.27) for bulge extent prediction are valid when the peak load  $p_c$  is equal to, or greater than, the foam plateau stress  $\sigma_{pl}$ . If  $p_c$  is smaller than  $\sigma_{pl}$ , Eq. (7.5) and Eq. (7.27) predict complex values, not meaningful. In fact, it is obvious that there is no bulge in that situation. Further, from Eq. (7.5) and Eq. (7.27), a peak load exactly equal to the foam plateau stress leads to a zero bulge extent, reasonable.

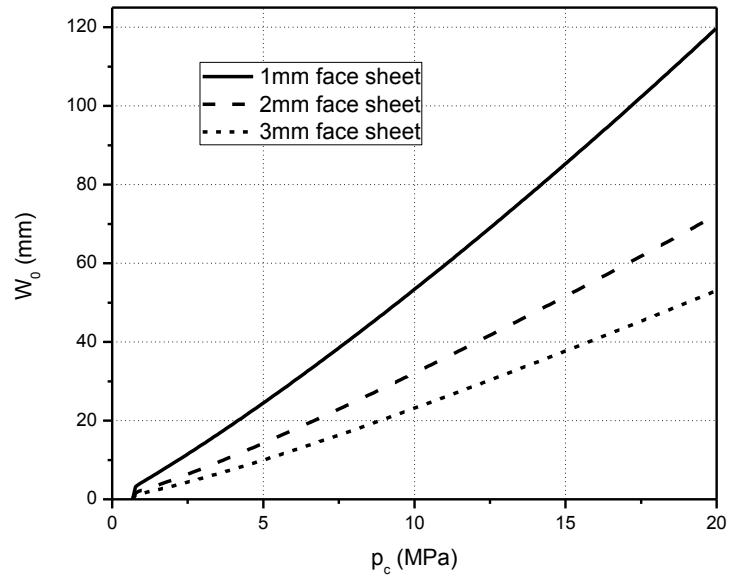
Parametric study is conducted through analyzing a typical cladding subjected to a close range airburst. In the present study, aluminum foam of relative density of 5% with a 0.67 MPa plateau stress is used. The standoff distance is fixed as 0.3 m and the charge weight varies to yield different loading intensities. The face sheet thicknesses are 1 mm, 2 mm and 3 mm, respectively. Certain parameter varies while others remain unchanged to illustrate its influence.

From Fig. 7.6, the bulge depth increases with the peak load on cladding and blast duration. It should be noted that when the peak load increases, with the same standoff distance, the bulge extent also increases. Therefore, a stronger peak load results in not only a larger bulge depth, but also a larger extent. However, a longer blast duration deepens the bugle but has no influence on the extent.

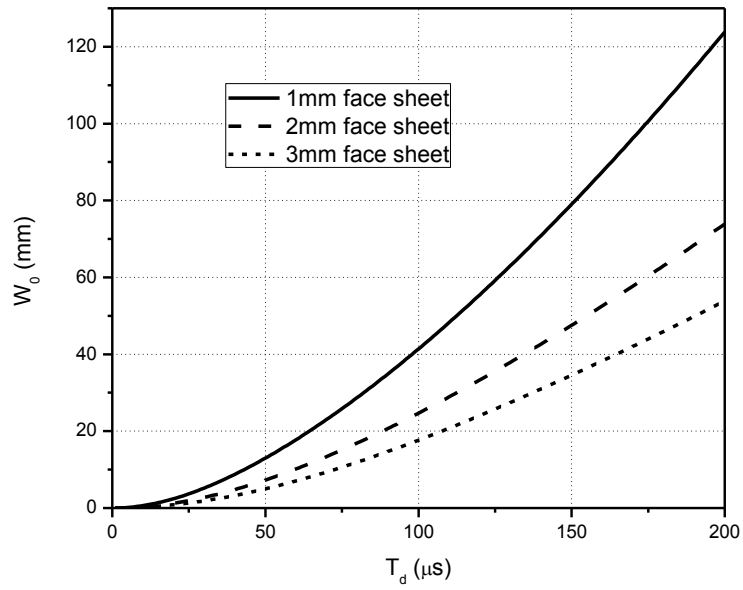
It is suggested that when a material undergoes a dynamic load, its yield strength is no longer a constant and it is a function of the strain rate, delineated by Cowper-Symonds equation (Jones 1989):

$$\frac{\sigma_{yd}}{\sigma_{ys}} = 1 + \left( \frac{\dot{\epsilon}}{D} \right)^{\frac{1}{q}} \quad (7.28)$$

where  $\dot{\epsilon}$  is the strain rate;  $\sigma_{yd}$  and  $\sigma_{ys}$  the dynamic and quasi-static yield strengths;  $D$  and  $q$  two material constants needed to be determined by experiments. For mild steel,  $D$  is 40 and  $q$  is 5 while for aluminum,  $D$  is 6500 and  $q$  is 4 (Jones 1989), which implies mild steel is a rate sensitive



(a)



(b)

Fig. 7.6 Relation between the bugle depth and: (a) peak load; (b) blast duration.

material and aluminum is not. From Eq. (7.28), when the face sheet undergoes dynamic stretching, its yield strength increases and is greater than the quasi-static value, resulting in more energy absorbed during the plastic stretching of the face sheet and consequently a smaller bulge depth. Therefore in the thesis, neglecting the strain rate effect of the face sheet leads to a conservative prediction of the bulge depth. If the strain rate effect is considered or another material is used as face sheet, the relationship between the bulge depth and the face sheet dynamic yield strength is illustrated in Fig. 7.7.

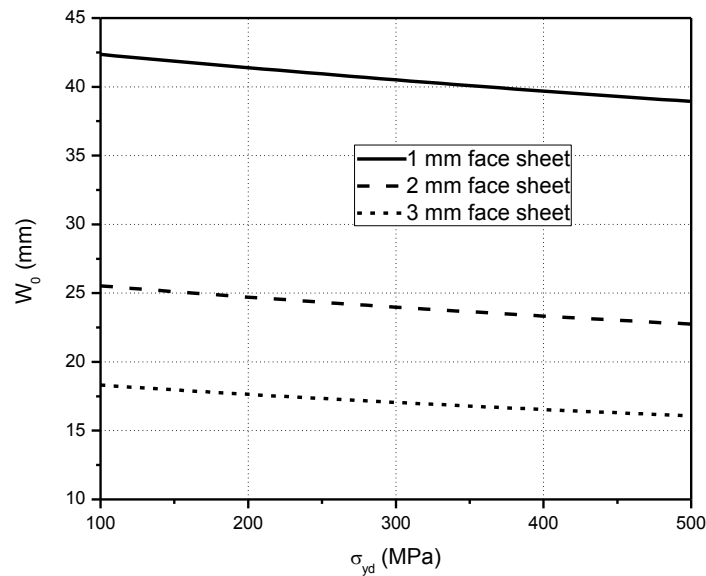
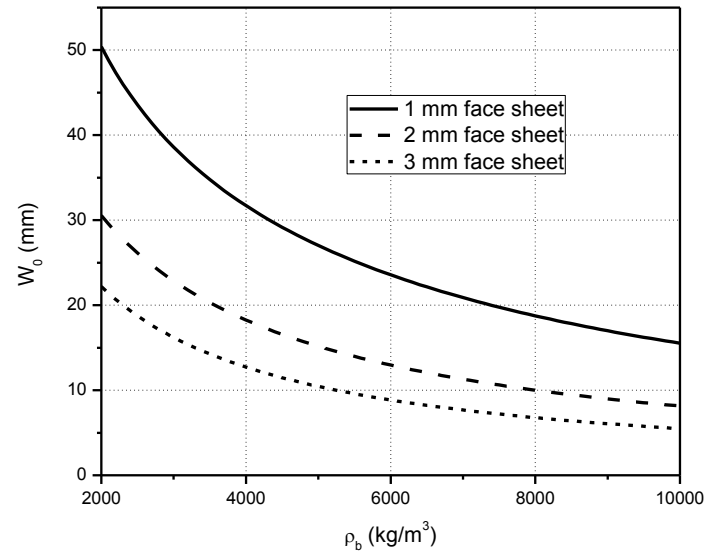


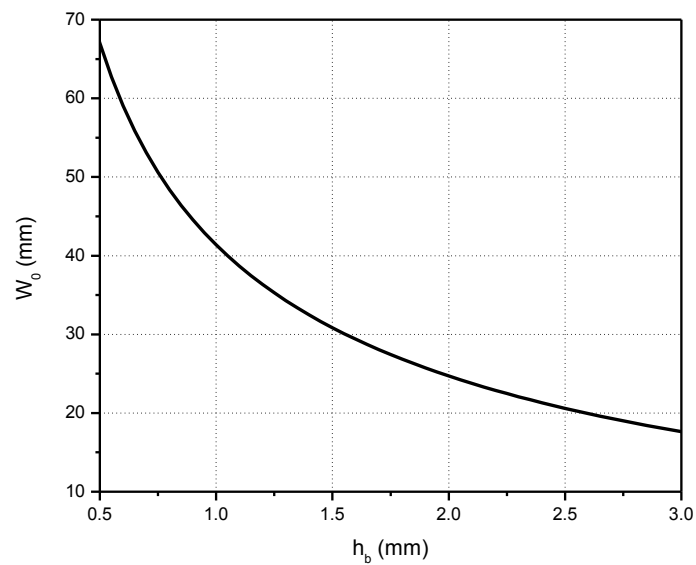
Fig. 7.7 Relation between the bugle depth and face sheet yield strength

Figure 7.8 indicates the bulge depth decreases with the increased face sheet density and thickness. The mechanism is that subjected to the same blast load, the initial velocity imparted by the impulse is inversely proportional to the mass of the face sheet, which is a product of density, thickness and loaded area. Further, the kinetic energy gained, or the energy needed to be dissipated by foam, is proportional to the initial velocity squared. Subsequently, the greater the face sheet density and thickness, the less energy to be dissipated by foam. For this reason, the face sheet should not be too thin,

otherwise a larger amount of energy is imparted. However, a cladding with very heavy face sheet is not practical in terms of mass efficiency. Therefore, the face sheet density and thickness should be optimized to achieve a balance of acceptable protection effect and mass efficiency.



(a)



(b)

Fig. 7.8 Relation between the bugle depth and: (a) face sheet density; (b) face sheet thickness

Now fix the blast load and vary the foam relative density, on which the plateau stress and densification strain are dependent. As expected, the bulge depth decreases with foam relative density, indicated in Fig. 7.9. According to the principle of foam selection discussed previously, the foam relative density cannot be too high, or the protected structure is overloaded. Then the foam relative density should be judiciously selected so that the plateau stress of the chosen foam is slightly smaller than the damage tolerance of the protected structure.

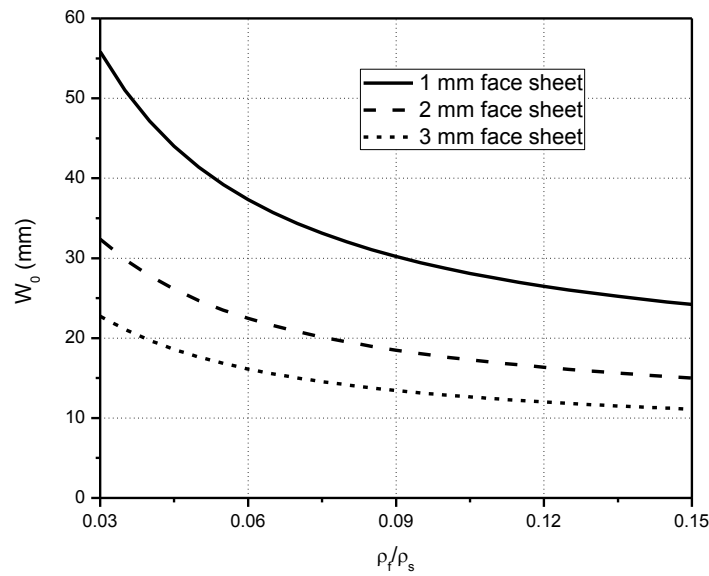


Fig. 7.9 Relation between the bugle depth and foam relative density

The value of  $\beta$  depends on the initial velocity is illustrated in Fig. 7.10. It can be seen that the higher the initial velocity, the smaller the  $\beta$  value and vice versa. With a negligibly small initial velocity,  $\beta$  converges to 0.5. If the initial velocity is less than 250 m/s,  $\beta$  is greater than 0.2. From Fig. 7.11, if the  $\beta$  is greater than 0.2, the influence of  $\beta$  on the bulge depth is limited, especially for claddings with relatively thicker face sheets, which implies the bulge depth in the present study is reasonably conservative and is not seriously over-predicted.

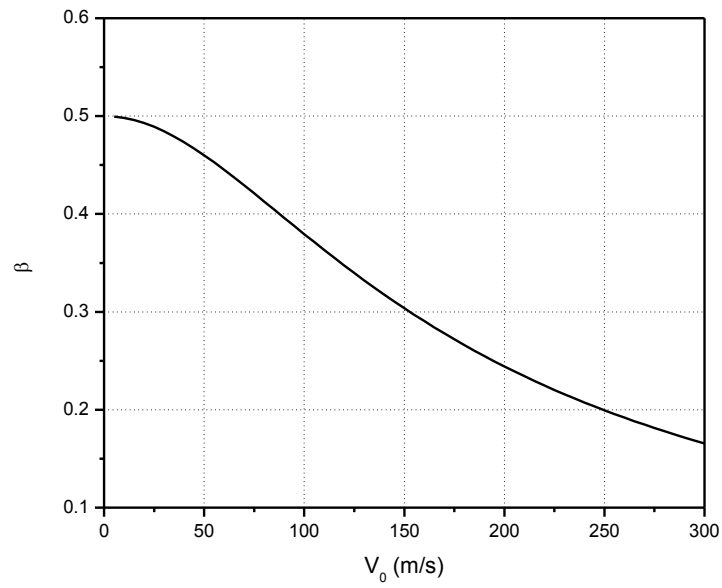


Fig. 7.10 Relation between  $\beta$  and the initial peak velocity

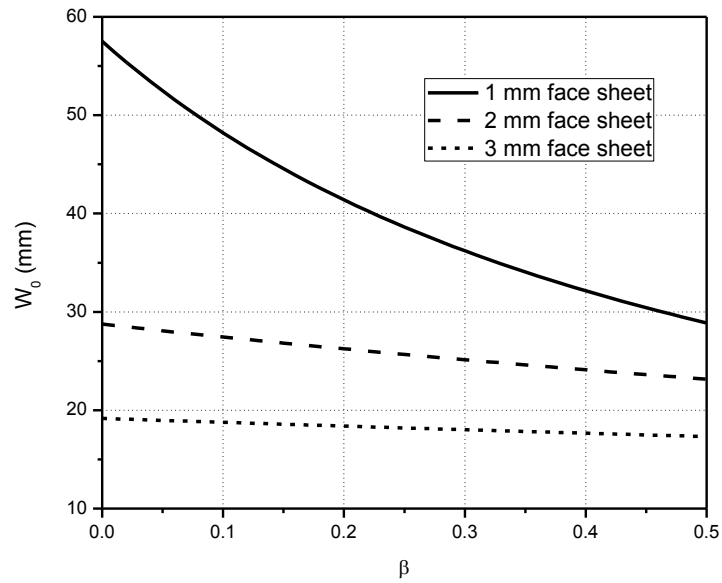


Fig. 7.11 Relation between the bugle depth and  $\beta$



The present study proposed a method to analyze 2-D cladding response under a close range explosion, in which the applied load is simplified as a generalized Gaussian function. The prediction would be more accurate if the load in model is closer to that in the real situation. To achieve a more accurate prediction of the bulge, blast load and face sheet deflection profile with higher accuracy may be used, however the analysis is more expensive. The energy method is generally effective in determining the bulge depth. If the close range explosion has other form, for instance, a cylindrical explosion, the only difference is the load and bulge shape should be re-defined. The response prediction of a blast mitigation cladding with metal foam core subjected to a localized explosion should be experimentally validated.

## **7.4 Analysis of density gradient metal foam for blast mitigation**

Careful examination of the characteristics of the naturally existing cellular materials reveals that some of them have gradient rather than homogeneous. For instance, the foam cell size of the outer layer of certain grass stem is significantly smaller than that of the inner layer (Gibson 2005). The relatively stiffer outer part provides higher resistance to external loads such as bending and buckling while the less dense inner part reduces its total weight and carries out biological functions.

Recently, a few experiments and numerical simulations on multi-layered homogeneous foam subjected to impact were carried out, showing that the layered foam core may have some merits when assembled appropriately (Zeng et al. 2010a, b). However, the underlying mechanism remains to be understood since there has been no theoretical study about the non-homogeneous foam subjected to blast/impact. In the present study, high velocity crushing of foam core with continuous density gradient, induced by a typical blast load, is theoretically investigated and the merits of applying gradient foam

as blast mitigation cladding core is analyzed. It is assumed that in this chapter, the foam crushing velocity is high, in whose major densification process the velocity of the shock front is higher than that of the elastic precursor thus the foam undergoes progressive collapse. Further, a typical metal foam, i.e., open-cell aluminum foam, is investigated as an example and the analysis can be applied to other foams with similar density gradient subjected to high velocity crushing.

#### 7.4.1 Formulation of continuous foam subjected to a blast load

To design and construct a gradient foam core to optimize the performance of a blast mitigation cladding consisting of a face sheet and foam core, the characteristics of the load applied should be taken into consideration. A typical blast load is a pulse with a sharp rise and a rapid exponential decrease, often simplified to a triangular pulse, whose intensity is highest initially and decreases linearly with time:

$$P(t) = \begin{cases} P_0 \left(1 - \frac{t}{T_d}\right) & t \leq T_d \\ 0 & t > T_d \end{cases} \quad (7.29)$$

where  $P_0$  and  $T_d$  are the peak load and duration of the blast on the face sheet, respectively.

Another significant aspect is under high velocity crushing, the foam undergoes progressive collapse while under quasi-static and low velocity crushing, foam densification is in a uniform manner (Ashby *et al.* 2000; Lu and Yu 2003). The crushing velocity threshold for progressive collapse depends on the foam characteristics such as cell thickness, cell size and base material properties. Further, the energy absorbed by progressive collapse is remarkably higher than that of uniform crushing when the same foam is deformed to the same final state (Zou *et al.* 2009). In the present study, the crushing velocity is high due to being loaded by a blast, the foam core is assumed to undergo progressive collapse from the impact end.

According to the characteristics of the blast load with an initial peak and a rapid decay, intuitively, the gradient foam may have advantage over its homogeneous counterpart

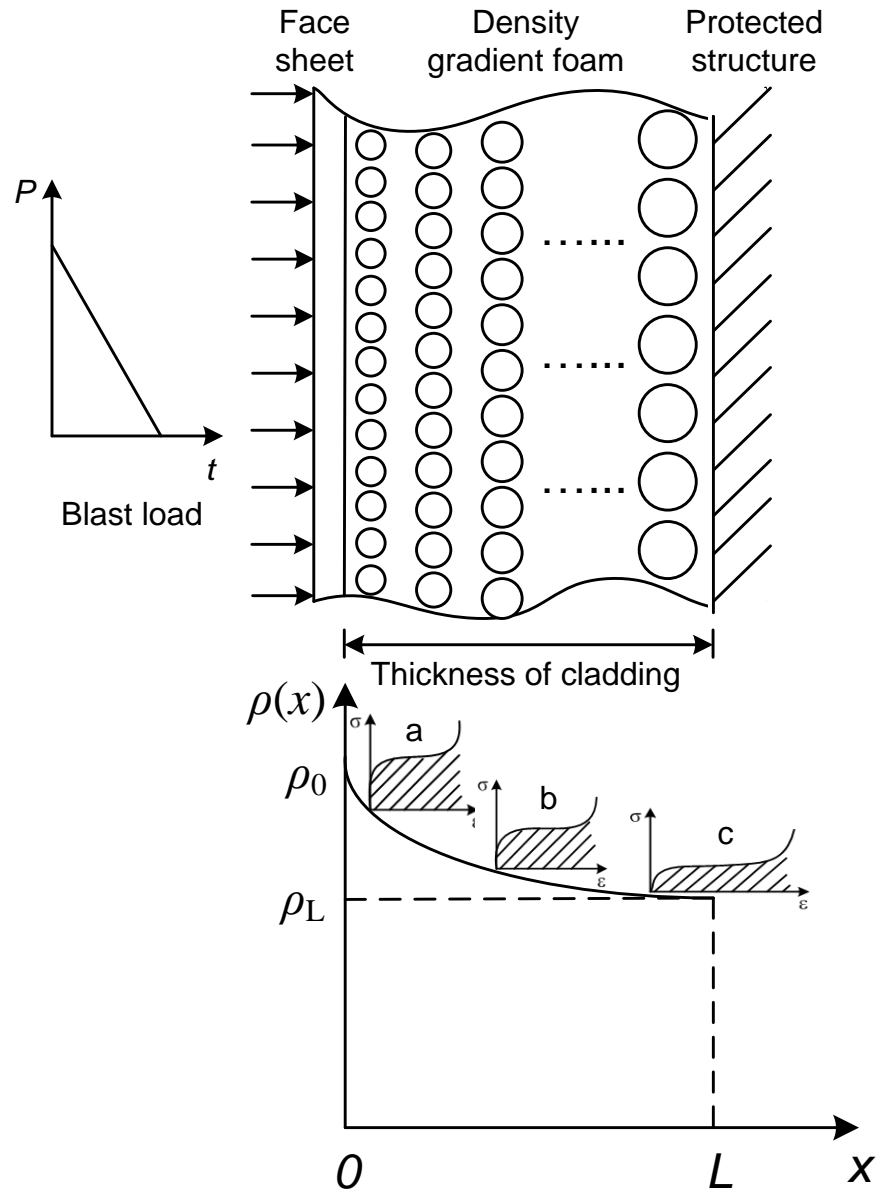


Fig. 7.12 Foam core with density gradient: (a) high relative density, high plateau stress, small densification strain; (b) moderate relative density, moderate plateau stress, moderate densification strain; (c) low relative density, low plateau stress, large densification strain

with the same mass and thickness if the foam part of the highest density is placed in the impact end, indicated in Fig. 7.12. The foam at the impact end has higher relative density, resulting in higher plateau stress and smaller densification strain while the foam at the stationary end has smaller relative density, smaller plateau stress and larger densification strain. The foam in the intermediate layer has moderate properties in between. The merits of this foam density configuration will be discussed in a case study.

To capture the foam behavior under high velocity crushing, shock theory is frequently employed (Reid and Peng 1997; Tan et al. 2005; Harrigan et al. 2010), in which the stress-strain relationship of the foam is idealized with a rigid-perfectly-plastic-lock (RPPL) model, shown in Fig. 7.13. It is also applied to predict the foam crushing process in the present study. Consider a one-dimensional continuously gradient foam attached to a protected structure with a steel face sheet installed at the impact end, shown in Fig. 7.14. The density and density gradient of the foam core are assumed:

$$\rho(x) = \rho_0 e^{-\beta \frac{x}{L}}, \beta = -\ln \frac{\rho_L}{\rho_0} \quad (7.30)$$

where  $\rho_0$  and  $\rho_L$  are the densities at impact and stationary ends of the gradient foam core, respectively, indicated in Fig. 7.12;  $L$  is the foam core thickness; and  $x$  is coordinate starting from the initial location of the interface between the face sheet and foam core.

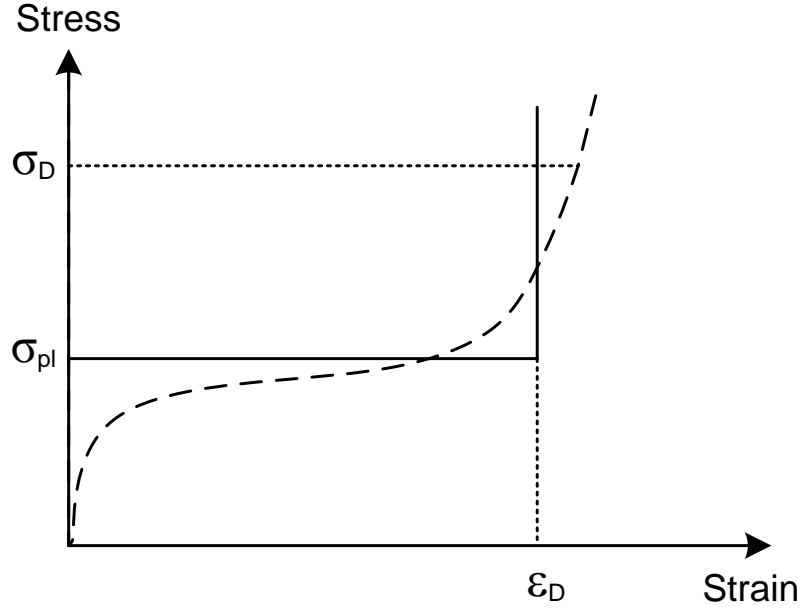


Fig. 7.13 Idealization of the stress-strain relation of metal foam (relative density less than 0.3)

When one end of the metal foam is compressed in a high velocity, a stress wave or stress waves will propagate to further part. If the intensity of the stress wave is higher than the elastic limit of the foam, due to the upward concave stress-strain relationship of the foam, the plastic stress wave will eventually develop into a shock wave, crushing the foam progressively (Lu and Yu 2003). The densification stress at the shock front, a very thin layer between the crushed and uncrushed foam parts, is determined by the plateau stress and the crushing velocity:

$$\sigma_D = \sigma_{pl} + \frac{\rho \dot{u}^2}{\epsilon_D} \quad (7.31)$$

where  $\rho$ ,  $\sigma_{pl}$  are the density and plateau stress of the foam, respectively.  $u$  is the face sheet displacement thus  $\dot{u}$  is the velocity of the face sheet, which is also the velocity of the crushed foam if the densified foam is considered rigid. The densification strain  $\epsilon_D$  and the plateau stress of the foam are (Ashby *et al.* 2000):

$$\varepsilon_D = 1 - \lambda \frac{\rho}{\rho_s} \quad (7.32)$$

$$\sigma_{pl} = C_1 \left( \frac{\rho}{\rho_s} \right)^{\frac{3}{2}} \sigma_y \quad (7.33)$$

$\rho_s$  is the solid bulk material density of the foam, e.g. 2700 kg/m<sup>3</sup> for aluminum.  $\lambda$  is a constant, 1.5 for aluminum foam (Ashby *et al.* 2000); and  $\sigma_y$  is the yield strength of the solid material from which the foam is made, 200 MPa for aluminum, and  $C_1$  is a constant ranging from 0.2 to 0.3 (Ashby *et al.* 2000), taken as 0.3 in the present study. It should be noted that due to the density gradient, the plateau stress and densification strain are functions of location.

When metal foam is crushed, the density after crushing can be calculated (Ashby *et al.* 2000):

$$\rho^* = \frac{\rho}{1 - \varepsilon_D} \quad (7.34)$$

Substituting Eq. (7.32) into Eq. (7.34), the density of the crushed foam is:

$$\rho^* = \frac{\rho_s}{\lambda} \quad (7.35)$$

It is interesting to know although the foam density before crushing is a function of location, it becomes a constant after densification. From Eq. (7.32), when crushed, foam with a lower relative density undergoes a larger densification strain while foam with a higher relative density experiences a smaller densification strain, resulting in the same crushed state and density.

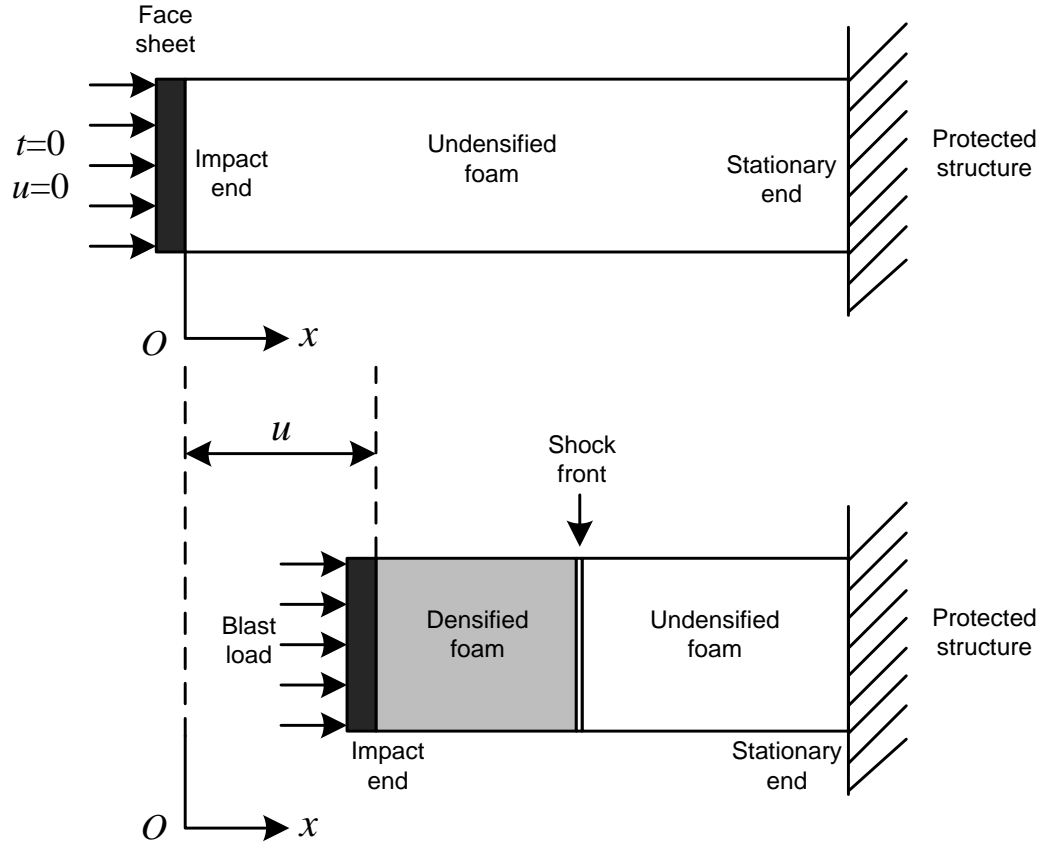


Fig. 7.14 A blast mitigation cladding with metal foam core and a face sheet (within blast duration)

Take the combination of the face sheet and the densified part of the foam to analyze, where the shock front, a very thin layer between the densified and undensified foam, is excluded. Consider an instant when the face sheet moves a distance  $u$  and the shock front propagates a distance  $l$ , the mass per unit area of the densified foam is:

$$\Delta m = \int_u^l \frac{\rho_s}{\lambda} dx = \frac{\rho_s}{\lambda} (l - u) \quad (7.36)$$

The mass of the corresponding part before crushing is:

$$\Delta m = \int_0^l \rho(x) dx = \int_0^l \rho_0 e^{-\beta \frac{x}{L}} dx = \frac{\rho_0 L}{\beta} \left( 1 - e^{-\beta \frac{l}{L}} \right) \quad (7.37)$$

It is evident that the mass should be the same no matter the foam is crushed or not, combination of Eq. (7.36) and Eq. (7.37) yields:

$$u = l - \frac{\lambda \rho_0 L}{\beta \rho_s} \left( 1 - e^{-\beta \frac{l}{L}} \right) \quad (7.38)$$

The relationship between the face sheet displacement and the shock front location is established for the density gradient foam. When the foam density gradient is significantly small and near zero, the gradient foam reduces to the intensively studied homogeneous foam. Let  $\beta \rightarrow 0$ , Eq. (7.38) is recast as:

$$\begin{aligned} u \Big|_{\beta \rightarrow 0} &= l - \frac{\lambda \rho_0 L}{\rho_s} \lim_{\beta \rightarrow 0} \frac{1 - e^{-\beta \frac{l}{L}}}{\beta} \\ &= l - \frac{\lambda \rho_0 L}{\rho_s} \lim_{\beta \rightarrow 0} \frac{l}{L} e^{-\beta \frac{l}{L}} \\ &= l \left( 1 - \lambda \frac{\rho_0}{\rho_s} \right) \end{aligned} \quad (7.39)$$

Note that the foam density at the impact end  $\rho_0$  in Eq. (7.39) in fact is the uniform density for homogeneous foam since the density difference in the foam is negligibly small when  $\beta$  approaches zero. Recall the definition of densification strain of homogeneous foam from Eq. (7.32), Eq. (7.39) is further written as:

$$u \Big|_{\beta \rightarrow 0} = l \varepsilon_D \quad (7.40)$$

which is the relationship between the face sheet displacement and shock front location for homogeneous foam under high velocity crushing, in agreement with the previous studies (Ashby et al. 2000; Lu and Yu 2003). In fact, the relationship expressed in Eq. (7.40) for homogeneous foam is a special case for that of the gradient foam.



In light of the Newton's law, with the free body diagram shown in Fig. 7.15, recall Eq. (7.38), the governing equation for the system consisting of the face sheet and densified foam within the blast duration is:

$$\left[ \rho_b h_b + \frac{\rho_0 L}{\beta} \left( 1 - e^{-\beta \frac{l}{L}} \right) \right] \left[ \left( 1 - \frac{\lambda \rho_0}{\rho_s} e^{-\beta \frac{l}{L}} \right) \ddot{l} + \frac{\lambda \rho_0 \beta}{\rho_s L} e^{-\beta \frac{l}{L}} \dot{l}^2 \right] + \frac{\rho(l)}{1 - \lambda \frac{\rho(l)}{\rho_s}} \left( 1 - \frac{\lambda \rho_0}{\rho_s} e^{-\beta \frac{l}{L}} \right)^2 \dot{l}^2 + C_1 \left( \frac{\rho(l)}{\rho_s} \right)^{\frac{3}{2}} \sigma_{ys} - P_0 \left( 1 - \frac{t}{T_d} \right) = 0 \quad (7.41)$$

where  $\rho_b$  and  $h_b$  are the density and thickness of the face sheet, respectively;  $t$  is time starting at the arrival of the blast load on the face sheet;  $T_d$  is the blast duration. Equation (7.41) is an ordinary differential equation about the shock front location  $l$ . The initial conditions of the concerned part are:

$$l(0) = 0, \quad \dot{l}(0) = 0 \quad (7.42)$$

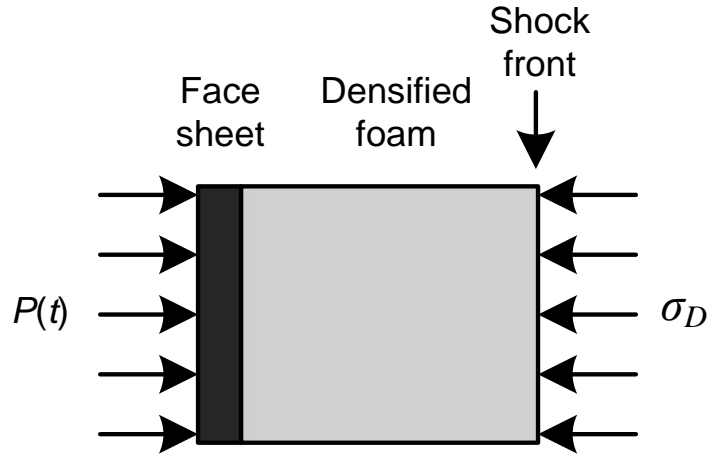


Fig. 7.15 Free body diagram of the system consisting of the face sheet and densified foam (within the blast duration)

Since the blast duration of an airburst is very short, typically the foam densification has blast load phase and post-blast load phase. Crushing of the foam continues in the post-blast load phase before all the energy imparted is dissipated. Without external blast load, the governing equation in the post-blast load phase is:

$$\left[ \rho_b h_b + \frac{\rho_0 L}{\beta} \left( 1 - e^{-\beta \frac{l}{L}} \right) \right] \left[ \left( 1 - \frac{\lambda \rho_0}{\rho_s} e^{-\beta \frac{l}{L}} \right) \ddot{l} + \frac{\lambda \rho_0 \beta}{\rho_s L} e^{-\beta \frac{l}{L}} \dot{l}^2 \right] + \frac{\rho(l)}{1 - \lambda \frac{\rho(l)}{\rho_s}} \left( 1 - \frac{\lambda \rho_0}{\rho_s} e^{-\beta \frac{l}{L}} \right)^2 \dot{l}^2 + C_1 \left( \frac{\rho(l)}{\rho_s} \right)^{\frac{3}{2}} \sigma_{ys} = 0 \quad (7.43)$$

The initial condition for the post-blast phase in fact is the terminal condition of the blast load phase to ensure the continuity of the shock front displacement and velocity:

$$l(t = T_d) = R \quad \dot{l}(t = T_d) = V \quad (7.44)$$

With the initial conditions and governing equations, the shock front location time history can be determined. Subsequently, the time history of the system consisting of the face sheet and densified foam in terms of the face sheet displacement can be obtained by applying Eq. (7.38). From Eq. (7.38), Eqs. (7.41) through (7.44), close form solutions of the crushing time histories governed by these nonlinear differential equations cannot be obtained and Runge-Kutta method is employed to solve them numerically.

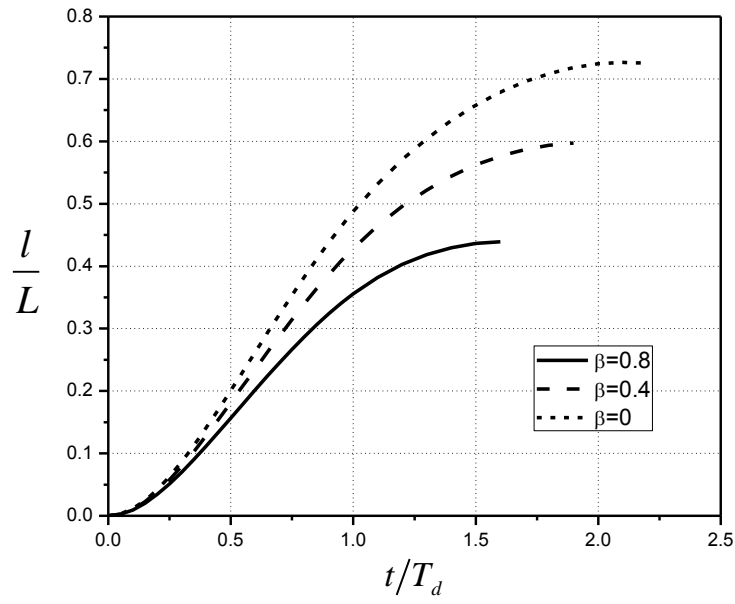
## 7.4.2 Case study and discussions of gradient foam under high velocity crushing

To illustrate the merits of gradient foam in blast alleviation, a case study is conducted. The face sheet, made of steel, is assumed to be rigid, 2 mm. A typical blast load from

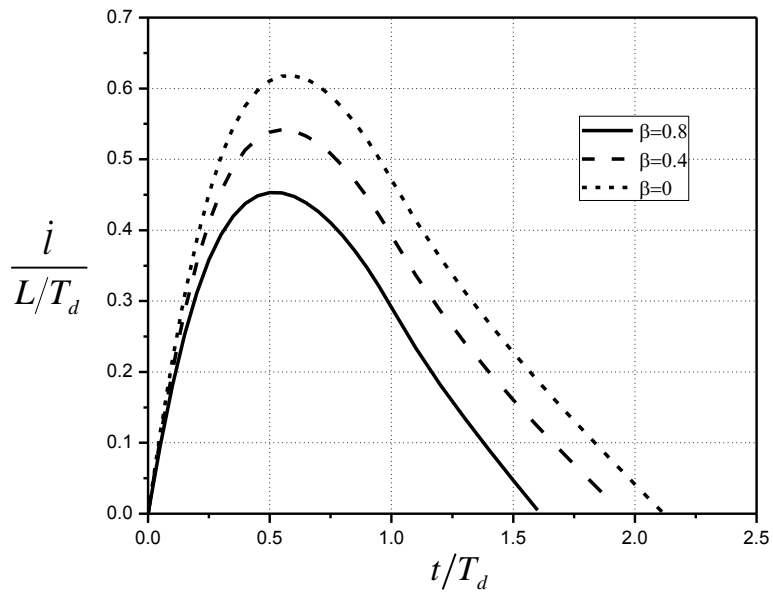
airburst is perpendicularly applied on the face sheet. Two gradient foam cores are investigated and compared to a homogeneous core (relative density 12.33%) with the same weight and thickness (70 mm) for reference. The peak load and duration of the blast are 11 MPa and 0.5 ms, respectively.

It should be noted that by assuming high velocity crushing where in major densification process, the shock front velocity is higher than the elastic precursor speed, the assumption of progressive collapse crushing rigorously holds. In fact, it is obvious that in the very initial stage and the very late stage of the densification, the crushing velocity is small, where the foam may undergo uniform densification. However, with progressive collapse of foam used throughout the entire crushing process in delineating the densification, i.e., from the initial application of the blast load to the retardation of foam crushing to rest, the difference between the theoretical prediction and the numerical simulation is marginal (Hanssen et al. 2002; Ma and Ye 2007b). Therefore the same approach in the present study leads to a reasonable prediction.

From Fig. 7.16(a), for the same blast load, the length of densified foam increases with the decrease of core density gradient. When the gradient is negligibly small, the foam becomes homogeneous and the largest densified length is achieved. It can be imagined that if the density gradient is negative, which means the density of the gradient foam is smallest at the impact end and largest at the stationary end, the total length of the crushed foam should be greater, even larger than that of the homogenous foam. Therefore to mitigate a blast load, provided that the foam core undergoes progressive collapse from the impact end, a smaller thickness suffices for a cladding with larger density gradient core, allowing for larger standoff distance to improve mitigation effect. In addition, it takes a shorter time for the cladding with larger density gradient to dissipate all the energy imparted. From Fig. 7.16(b), the larger the density gradient, the smaller is the shock front velocity. Besides the crushed foam length, another variable of significance is the face sheet displacement. Figure 7.17 indicates that the displacement and velocity of the face sheet is similar to those of the shock front.

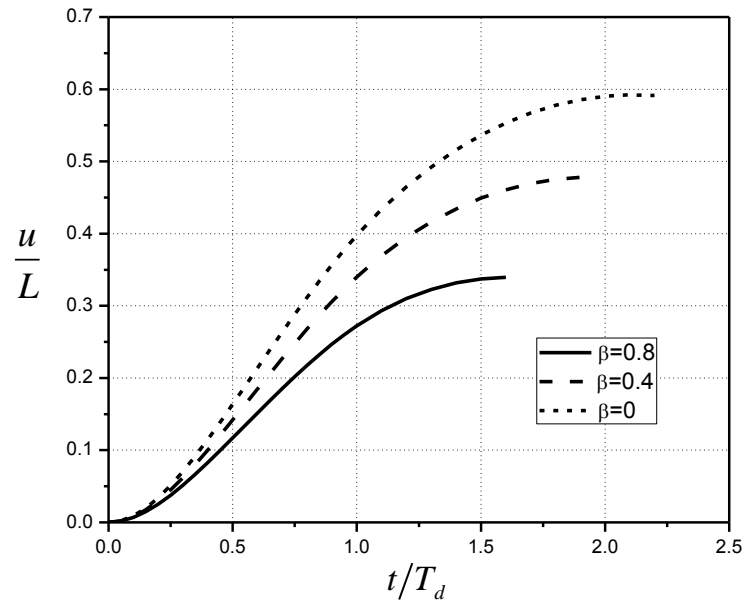


(a)

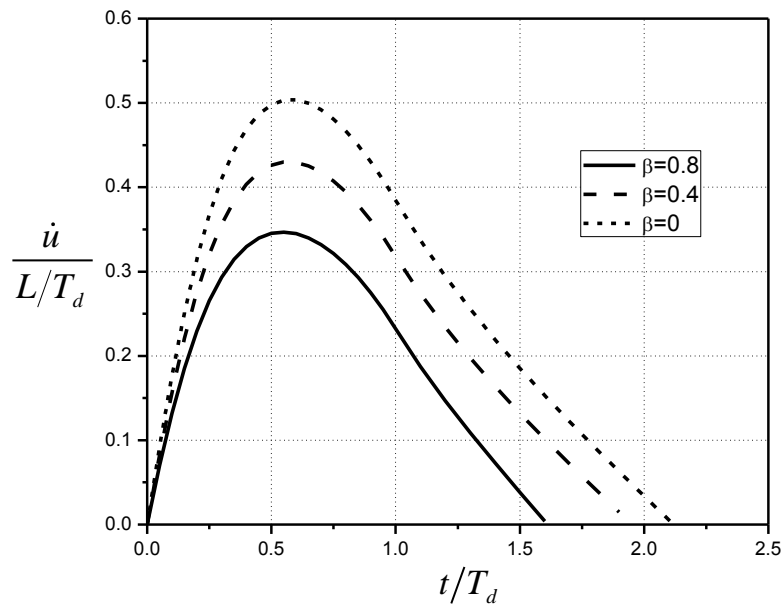


(b)

Fig. 7.16 Time histories of (a) displacement; (b) velocity of the shock front



(a)



(b)

Fig. 7.17 Time histories of (a) displacement; (b) velocity of the system consisting of the face sheet and densified foam

For effective mitigation of a blast load, the energy absorption feature of a cladding is a major concern. The specific energy (energy per unit area) absorbed by foam core is calculated (Zou et al. 2009) as:

$$E = \int_0^l \left[ \sigma_{pl}(\xi) \varepsilon_D(\xi) + \frac{1}{2} \rho(\xi) \dot{u}^2 \right] d\xi \quad (7.45)$$

where  $\dot{u}$  is the crushing velocity of the system consisting of the face sheet and densified foam. Figure 7.18 reveals that for the same blast load, the energy imparted by the pulse to the cladding, which is in fact the energy needed to be dissipated by the foam core before the crushing stops, is related to the core density gradient: the greater the gradient, the smaller is the total input energy. The underlying mechanism is as follows: recall Eq. (7.31) through Eq. (7.33) and the density profile of the foam, resistance for the concerned system consisting of the face sheet and densified foam is the densification stress at the shock front:

$$\sigma_D = C_1 \left( \frac{\rho(x)}{\rho_s} \right)^{\frac{3}{2}} \sigma_{ys} + \frac{\rho(x) \dot{u}^2}{1 - \lambda \frac{\rho(x)}{\rho_s}} \quad (7.46)$$

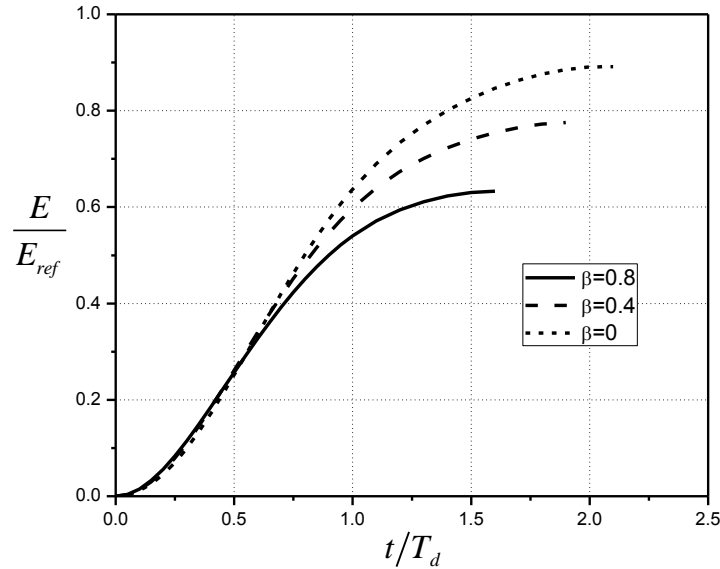


Fig. 7.18 Time histories of energy absorption ( $E_{ref}$  is the total energy absorption when the homogeneous foam core is fully densified quasi-statically)

In the initial stage of the blast load, the displacement of the system of interest is negligibly small, the plateau stress of the gradient foam at the impact end is larger than that of the homogeneous foam. In addition, in this stage the velocity differences between the foams are small, indicated in Fig. 7.17(b). According to Eq. (7.46), the resistance against crushing, consisting of the plateau stress and dynamic enhancement, of the gradient foam at the impact end is higher due to the higher plateau stress and similar dynamic enhancement thus the face sheet and densified foam is more difficult to accelerate. Furthermore, take the same crush stroke for reference, the mass of the densified foam is larger, more difficult to accelerate. These two aspects combined result in a higher resistance for the face sheet and densified foam for the gradient core, thus the velocity of the concerned system is lower than that of the homogeneous foam, subsequently the energy imparted into the cladding is smaller for the gradient foam to dissipate. Further, take the homogeneous foam to analyze. From Fig. 7.16(a), in the case study, 72.7% of the homogeneous foam is densified with energy absorbed per unit area of  $153 \text{ kJ/m}^2$ , while with the same crushed length, only  $108 \text{ kJ/m}^2$  is absorbed by quasi-static crushing, implying the dynamic foam crushing absorbs remarkably more energy than the quasi-static crushing, which is in agreement with the previous research (Lopatnikov et al. 2003).

Further, from Fig. 7.19, the energy absorption rate of foam with a larger density gradient is higher in the initial stage. In fact, the energy absorbed per unit volume is the area under the ‘shock chord’ (Zou et al. 2009), determined by the plateau stress, the densification stress, the densification strain as well as the crushing velocity. For the impact end of the foam core with larger density, the combination of these factors leads to a larger energy absorbing capacity per unit volume. Specifically, according to Eq. (7.46), in the initial stage, the velocity is small and the dynamic enhancement is negligibly small compared to the foam plateau stress. The energy absorbed per unit volume in this stage is dominated by the product of foam plateau stress and densification strain (Ashby et al. 2000):

$$W_s = \sigma_{pl} \varepsilon_D = C_1 \sigma_{ys} \left( \frac{\rho_f}{\rho_s} \right)^{\frac{3}{2}} \left( 1 - \lambda \frac{\rho_f}{\rho_s} \right) \quad (7.47)$$

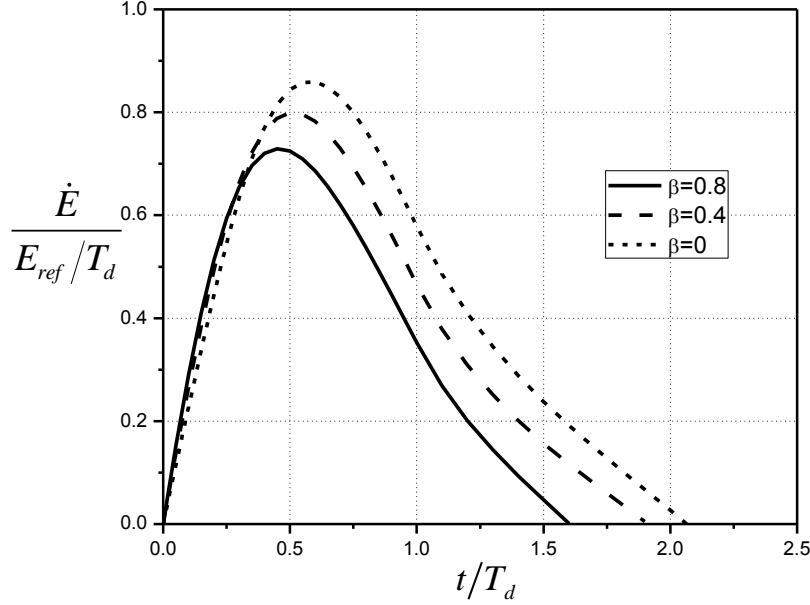


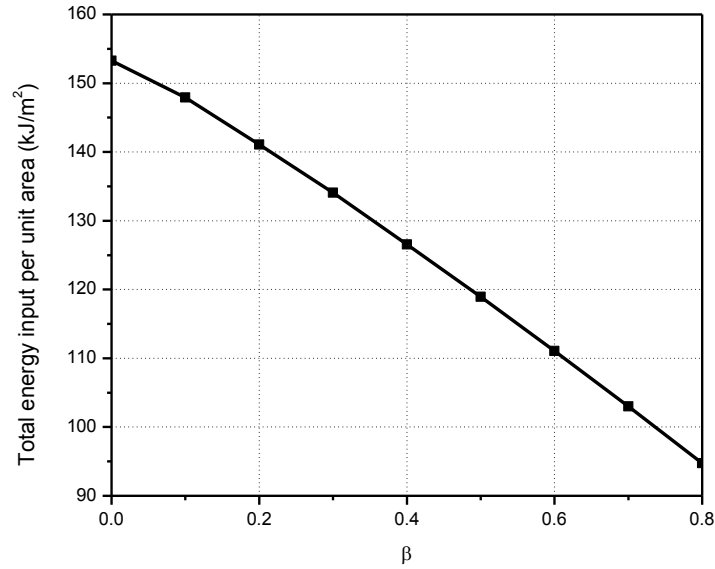
Fig. 7.19 Time histories of energy absorption rate ( $E_{ref}$  is the total energy absorption when the homogeneous foam core is fully densified quasi-statically)

Recall Fig. 7.4, due to the larger energy absorption capacity and small velocity, the energy absorption rate of foam with greater density gradient is higher in the initial stage.

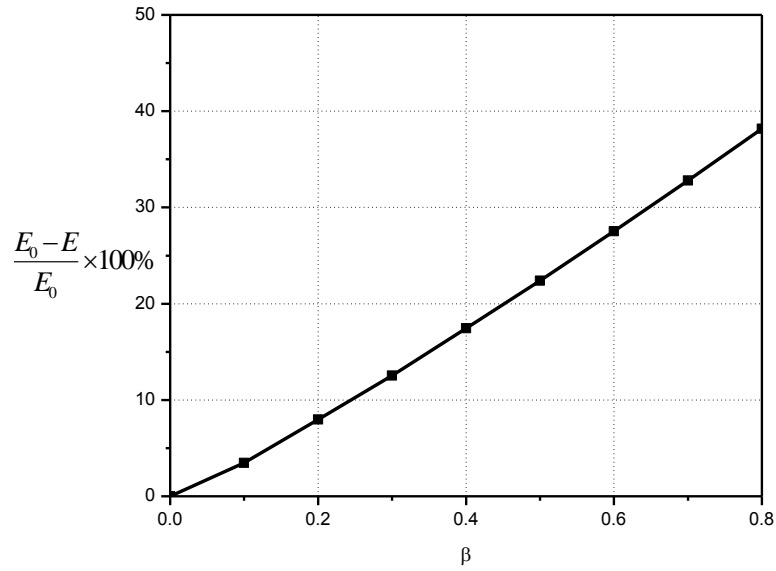
With less total input energy and a higher energy absorption rate in the initial stage, the foam core with larger density gradient makes efficient use of its part at the impact end according to the blast load characteristics in comparison with the homogeneous foam with the same weight and thickness, provided that the gradient foam undergoes progressive collapse from the impact end and other part upstream the shock front is undeformed or slightly deformed.



In addition, energy absorption characteristics of foam cores with various density gradients subjected to the same blast are investigated, indicated in Fig. 7.20. The foam thickness is fixed as 70 mm and the average relative density of the foams are fixed as 12.33%. From Fig. 7.20(a), the total input energy per unit area decreases with the increase of the density gradient. Further, with the homogenous foam as reference, energy reduction rate is defined as the ratio of total energy input difference between the homogeneous and gradient foam to total energy input of homogeneous foam. Figure 7.20(b) indicates that the total energy input reduction rate increases with the increase of foam density gradient.



(a)



(b)

Fig. 7.20 The relationships between (a) total energy input per unit area; (b) total energy input reduction per unit area and  $\beta$  ( $E_0$  is the energy input per unit area for  $\beta=0$ )

Furthermore, with density gradient fixed as  $\beta=0.8$ , the input energy reduction characteristics is examined by varying the peak of the blast load while keeping other parameters fixed. Table 7.1 lists the total energy input per unit area of density gradient foam, as well as that of the corresponding homogeneous foam with the same average relative density and thickness, subjected to varied peak blast loads. Figure 7.21 indicates that the input energy reduction rate decreases with the increase of the peak blast load, which implies for a weaker load, the energy reduction capacity is relatively higher while for a stronger load, the energy reduction capacity is relatively lower. The reason is that under a relatively weak load, only a thin layer of the gradient foam near the impact end is crushed while the rest part of the foam is undeformed or slightly deformed. Due to the characteristics of the density profile, this foam layer has larger relative density and larger specific energy absorption capacity (refer to Fig. 7.4),

leading to a greater resistance to the crushing, subsequently less total energy input, when compared to its homogeneous counterpart.

Table 7.1 Total energy input per unit area: the gradient foam ( $\beta=0.8$ ) and homogeneous foam ( $L=70$  mm;  $T_d=0.5$  ms;  $\rho/\rho_s=12.33\%$ )

$P_0$ (MPa)	Total energy input per unit area (J): $\beta=0$	Total energy input per unit area (J): $\beta=0.8$
8	83368	31224
9	106397	50167
10	130033	71370
11	153274	94754
12	187583	120187

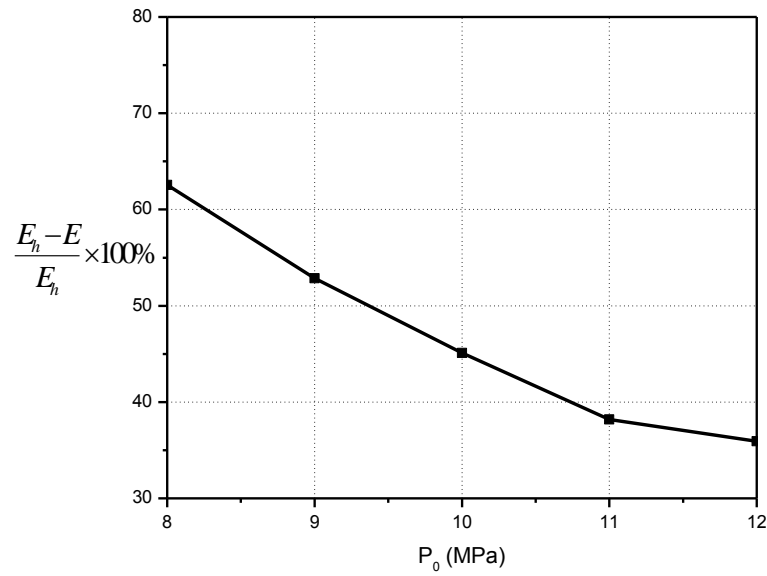


Fig. 7.21 The relationship between total energy input reduction per unit area and peak load ( $E_h$  is the energy input per unit area of the corresponding homogeneous foam for each load)

For homogeneous foam undergoing progressive collapse, the incident pressure to the protected structure is the foam plateau stress (Ashby et al. 2000), where the load experienced by the protected structure are nearly twice of the incident pressure, due to the remarkably difference of the acoustic impedances between the foam and the structure. Subjected to the same blast, with the structure assumed rigid, the average load exerted on the structure from gradient foam is higher than that from the counterpart homogeneous foam, due to the relatively shorter acting time, as shown in Fig. 7.17(b). To accurately predict the load on, and the response of, the protected structure, a model with the structure flexure incorporated is required, which is out of the scope of the thesis.

Prior to application, the foam core gradient should be judiciously selected and experimentally tested so that the core undergoes progressive collapse from the impact end with remaining part undeformed or slightly deformed, and absorbs lower total energy with a higher energy absorption rate in the initial stage. Further, other foam core with specific density profile can be designed according to the characteristics of a certain pulse which crushes the foam at a sufficiently high velocity, not necessarily triangular pulse, to optimize the mitigation effect. Again, these designs must be tested and validated experimentally.

In engineering application, for technical and economical reasons, the continuous gradient foam core may be substituted with several homogeneous foam layers stacked together. Layers with larger density should be installed near the impact end while the layers with smaller density near the protected structure to mitigate a typical airburst. Again, the foam density gradient of the discrete version of the continuous gradient foam should be judiciously selected and experimentally tested to ensure they undergo progressive collapse from the impact end adjacent to the face sheet while other part of the foam undeformed or slightly deformed.

## 7.5 Summary

A blast mitigation cladding with metal foam core subjected to a close range explosion is theoretically investigated. For a specific blast load, first the bulge extent is calculated; with the calculated extent, the bulge depth is determined. The bulge extent increases in a nonlinearly increasing way with peak load. The bulge depth increases with the peak load on the cladding and blast duration while decreases with thickness and density of the face sheet, yield strength of the face sheet and foam relative density. The procedure can be used in preliminary design of blast mitigation claddings.

Subjected to a typical blast load, compared to the homogeneous metal foam, the gradient foam makes efficient use of its density profile with largest density at the impact end of the cladding according to the pulse characteristics, whose intensity is highest at the initial stage and decays with time rapidly, leading to less total energy imparted to the cladding and needed to be dissipated by the foam core; the energy absorption rate in the initial stage of the gradient core is higher. The total energy input reduction rate decreases with increasing blast load intensity. The crush stroke of foam with larger density gradient is smaller, which may improve the mitigation effect. The proposed density gradient metal foam should be experimentally tested and validated prior to application.

## 8 CONCLUSIONS AND FUTURE WORK

### 8.1 Conclusions

In analysis of the response of a structure installed or submerged in certain media subjected to a media-transmitted dynamic load, an interfacial damping is introduced by the presence of the interface between the media and the structure, characterized by geometrical configurations and material properties of the structure and the surrounding media. The effects of the dynamic media-structure interaction effect is investigated qualitatively and quantitatively through analyzing a concrete plate buried in soil subjected to a soil-transmitted dynamic load. The smaller the structural deflection, the smaller is the interfacial damping ratio. The effect of the dynamic soil-structure interaction has a trend to reduce the structural responses.

In-structure shock of underground structures subjected to subsurface detonation is investigated theoretically using a beam model and rigid-body-motion included plate model. The soil-structure interaction is taken into consideration in the dynamic equation by introducing interfacial damping to the system consisting of the structural element and the surrounding soil. The solution of dynamic response of the underground structure is obtained by means of modal superposition. Based on the time histories of the structural response, the shock response spectra are subsequently constructed, and these shock response spectra provide an effective means for the assessment of the working condition of the equipment mounted on the structural member. Shock response spectra are employed to evaluate the shock level within the structure. Comparison of the equipment shock level with the shock tolerance indicates whether the built-in equipment or device is safe or shock isolation is needed. The maximum deformation, velocity and acceleration are greater in soil with larger acoustic impedance and smaller attenuation factor, which results in a higher equipment shock level and, thus, more detrimental. Especially, the maximum acceleration of the structural element is highly

sensitive to soil types, thus the protective structure is better constructed in a site with small acoustic impedance and large attenuation factor for safety purpose. Factors missing in the crude prediction in TM-5-855-1 such as particulars of the underground structure, soil-structure interaction and structural response are considered. Results show that the proposed in-structure shock assessment method is effective and can be used as a supplement to TM-5-855-1 and TM-5-1300.

A simple mitigation method for in-structure shock of underground protective structures is proposed. By adding an isolation slab, the excitation for the equipment at the floor center is altered. The excitation source is changed from combination of floor deflection plus rigid body motion of the whole structure to that of the isolation slab. The excitation pattern for the equipment is altered from a shock with a higher peak acceleration and a shorter duration to an attenuation oscillation with a lower peak acceleration and a longer duration. Case study shows that at the isolation slab center, the vertical in-structure shock level on the equipment is effectively reduced while near the edges the shock intensity on equipment is not high. This design exhibits excellent capacity to reduce the vertical shock level on equipment thus it may provide a supplementary reference for further design and modification of underground structures.

Further, the in-structure shock of underground facilities is theoretically investigated with soil blast rise time taken into consideration. A small scale test is designed and conducted to validate the theoretical prediction. When the scaled model of the underground structure is installed in wet fine sand and subjected to a soil-transmitted blast induced by a small scale subsurface detonation, the predicted acceleration time history favorably compare with the test results. The peak accelerations of the prediction are slightly higher than that of the tests and the acceleration profiles are similar. Further validation of the model is made by comparing the measured strain history of the mid-span to the prediction. With this prediction model as benchmark, the previous used model with zero soil blast rise time is calibrated. It is found that the displacement and velocity are similar but the profile of acceleration time history is significantly different.

In practical range of devices with supports, the shock level on equipment by blast with non-zero rise time is higher.

It is worth noting that from Chapter 3 to Chapter 6, the analyses are valid for linear elastic and small deflection assumptions, which are applicable to typical problems of in-structure shock of underground structures. If the subsurface detonation is close to the buried structure, the structure may undergo plastic and large deformation, even major damage, which cannot be predicted using the theory derived in the thesis. In fact, in the latter scenario, the focus of the analysis is no longer shock or vibration to inside devices; instead, the damage of the structures themselves are of major concern, out of the scope of the thesis.

A blast mitigation cladding with metal foam core subjected to a close range explosion is theoretically investigated. For a specific blast load, first the bulge extent is calculated; with the calculated extent, the bulge depth is determined. The bulge extent increases in a nonlinearly increasing way with peak load. The bulge depth increases with the peak load on the cladding and blast duration while decreases with thickness and density of the face sheet, yield strength of the face sheet and foam relative density. The procedure can be used in preliminary design of blast mitigation claddings.

Finally, bio-inspired, non-homogenous metal foam with a density gradient is proposed to be used as the core of a blast mitigation cladding and its merits are theoretically investigated. Subjected to a typical blast load, compared to the homogeneous foam, the gradient foam makes efficient use of its density profile with largest density at the impact end of the cladding according to the pulse characteristics, whose intensity is highest at the initial stage and decays with time rapidly, leading to less total energy imparted to the cladding and needed to be dissipated by the foam core; the energy absorption rate in the initial stage of the gradient core is higher. The crush stroke of foam with larger density gradient is smaller, which may improve the mitigation effect.



## 8.2 Future work

Future work will focus on the following aspects:

1. In the in-structure shock assessment of underground structures subjected to soil-transmitted blast load, the profiles of ground shocks are taken as triangles, either with a non-zero rise time or a zero rise time. However, due to the long path the soil blast travels before encountering the underground structure and soil non-uniformity, the profile of the blast on structure may be complex. A further study can be carried out to investigate the influence of pulse shape on the in-structure shock prediction.
2. By combining the ideas of metal foam and in-structure shock prediction, a new method to mitigate the in-structure shock of underground structures may be proposed: adding a layer of foam concrete outside the underground structure. The mechanism is that only the very initial part of the soil blast can effectively apply on the concrete foam and structure by guided separation between the soil and the concrete foam/structure.
3. Gradient metal foam under high velocity crushing is studied. If the crushing velocity is moderate, the crushing mode may be analytically predicted and experimentally tested.
4. In the empirical formula for metal foam densification strain,  $\lambda$  is a constant. Based on the analysis in Chapter 2, the candidate believes that  $\lambda$  may not be a constant, especially when the crushing load is high and the foam relative density is not very small. This should be examined experimentally.
5. The prediction of blast mitigation cladding with metal foam core subjected to a close range detonation should be experimentally validated with small scale tests.

6. In the experimental validation of the in-structure shock prediction, due to some limitations, only three small scale tests are conducted. The theoretical prediction of structural response under ground shocks and in-structure shock of underground structures will be further validated and more convincing if more tests with varied parameters are conducted.
7. Density gradient foam subjected to moderate speed crushing, in which the foam densification mode is different from that in the thesis, will be theoretical investigated.

## REFERENCES

- Ajdari, A., Nayeb-Hashemi, H. and Vaziri, A. (2011) "Dynamic crushing and energy absorption of regular, irregular and functionally graded cellular structures" International Journal of Solids and Structures, Vol. 48, pp. 506-516.
- Alwis, W.A.M., and Lam, K.Y. (1994) "Response spectrum of underground protective structures" Finite Elements in Analysis and Design, Vol. 18, pp. 203-209.
- Anand, S. (2002) "Measurement and Modelling of Ground Response due to Dynamic Loading" PhD Thesis, Nanyang Technological University, Singapore.
- Ashby, M.F., Evans, A., Fleck, N.A., Gibson, L.J., Hutchinson, J.W., and Wadley, H.N.G. (2000) Metal foams: a design guide, Butterworth-Heinemann.
- Baylot, J.T. (2000) "Effect of soil flow changes on structure loads" Journal of Structural Engineering-ASCE, Vol. 126, No. 12, pp. 1434-1441.
- Beals, J.T., and Thompson, M.S. (1997) "Density gradient effects on aluminium foam compression behavior" Journal of materials science, Vol. 32, pp. 3595-3600.
- Beppu, M., Okagaki, K., Katayama, M., and Itoh, M. (2011) EURODYN 2011: the 8<sup>th</sup> International Conference on Structural Dynamics, July 4-6, 2011, Leuven, Belgium.
- Biggs, J.M. (1964) Introduction to structural dynamics, McGraw Hill, New York.
- Chen, H.L., and Chen, S.E. (1996) "Dynamic response of shallow-buried flexible plates subjected to impact loading" Journal of Structural Engineering-ASCE, Vol. 122, No. 1, pp. 55-60.
- Chen, Y., and Krauthammer, T. (1989) "A combined Adina-finite difference approach with substructure for solving seismically induced nonlinear soil-structure interaction problems" Computers and Structures, Vol. 32, No. 3-4, pp. 779-785.

Chen, Y., and Krauthammer, T. (1992) “Seismic effects on large reinforced-concrete lifelines. 1. Theory” Computers and Structures, Vol. 42, No. 2, pp. 129-135.

Chen, Y., and Krauthammer, T. (1992) “Seismic effects on large reinforced-concrete lifelines. 2. Implementation” Computers and Structures, Vol. 42, No. 2, pp. 137-144.

Clough, R.W., and Penzien, J. (1993) Dynamics of structures, McGraw-Hill, International edition.

Cui, L., Kiernan, S., and Gilchrist, M.D. (2009) “Designing the energy absorption capacity of functionally graded foam materials” Materials Science and Engineering A, Vol. 507, pp. 215-225.

Dancygier, A.N., and Karinski, Y.S. (1999) “A simple model to assess the effect of soil shear resistance on the response of soil buried structures under dynamic loads” Engineering Structures, Vol. 21, pp. 1055-1065.

Departments of the army, the navy and the air force (1990) Structures to resist the effects of accidental explosions, TM-5-1300.

Deshpande, V.S., and Fleck, N.A. (2005) “One-dimensional response of sandwich plates to underwater shock loading.” Journal of the Mechanics and Physics of Solids, Vol. 53, pp. 2347-2383.

Dowding C.H., (1985) Blast Vibration Monitoring and Control. Prentice-Hall, Hemel Hempstead.

Gibson, L.J., and Ashby, M.F. (1997) Cellular solids: structures and properties, 2nd ed. Cambridge University Press, Cambridge.

Gibson, L.J. (2005) “Biomechanics of cellular solids” Journal of biomechanics, Vol. 38, pp. 377-399.

Gibson, L.J., Ashby, M.F., and Harley, B.A. (2010) Cellular materials in nature and medicine. Cambridge University Press, Cambridge.

Gupta, A.K. Response spectrum method in seismic analysis and design of structures, Blackwell Scientific Publications, 1992.

<sup>a</sup>Guruprasad, S, and Mukherjee, A. (2000) “Layered sacrificial claddings under blast loading Part I: analytical studies” International Journal of Impact Engineering, Vol. 24, pp. 957-973.

<sup>b</sup>Guruprasad, S, and Mukherjee, A. (2000) “Layered sacrificial claddings under blast loading Part II: experimental studies” International Journal of Impact Engineering, Vol. 24, pp. 975-984.

Hanssen, A.G., Enstock, L., Langseth, M. (2002) “Close-range blast loading of aluminium foam panels” International Journal of Impact Engineering, Vol. 27, pp. 593-618.

Hao, H., Ma, G.W., and Lu, Y. (2002) “Damage assessment of masonry infilled RC frames subjected to blasting induced ground excitations” Engineering Structures, Vol. 24, pp. 799-809.

Harrigan, J.J., Reid, S.R., and Yaghoubi, A.S. (2010) “The correct analysis of shocks in a cellular material” International Journal of Impact Engineering, Vol. 37, pp. 918-927.

Henrych, J. (1979) The dynamic of explosion and its use, Elsevier/North-Holland.

Huo, H., Bobet, A., Fernandez, G., and Ramirez, R. (2006) “Analytical solution for deep rectangular structures subjected to far-field shear stresses” Tunnelling and Underground Space Technology, Vol. 21, pp. 613-625.

Jardine, R.J., Potts, D.M., Fourie, A.B., and Burland, J.B. (1986) “Studies of the influence of non-linear stress-strain characteristics in soil-structure interaction” Geotechnique, Vol. 36, No. 3, pp. 377-396.

Jiang, D.Z., and Shu, D.W. (2005) “Prediction of peak acceleration of one degree of freedom structures by scaling law” Journal of Structural Engineering-ASCE, Vol. 131, No. 4, pp. 582-588.

- Jones, N. (1989) Structural impact, Cambridge university press.
- Kennedy, J.B., and Iyengar, K.J. (1981) "Behavior of viscoplastic circular plates under Gaussian impulse" Nuclear Engineering and Design, Vol. 64, pp. 117-128.
- Kiernan, S., Cui, L., and Gilchrist, M.D. (2009) "Propagation of a stress wave through a virtual functionally graded foam" International Journal of Non-Linear Mechanics, Vol. 44, pp. 456-468.
- Kiger, S.A., and Salim, H.A. (1998) "The use and misuse of structural damping in blast response calculations" American concrete institute special publication, 175: Concrete and blast effects, 121-130.
- Kobiela, S., and Krauthammer, T. (2004) "Dynamic response of buried silo caused by underground explosion" Shock and Vibration, Vol. 11, 665-684.
- Kobiela, S., Krauthammer, T., and Walczak, A. (2007) "Ground shock attenuation on a buried cylindrical structure by a barrier" Shock and Vibration, Vol. 14, pp. 305-320.
- Krauthammer, T., and Chen, Y. (1986) "Dynamic soil-structure interaction of rectangular reinforced-concrete lifelines" Engineering Structures, Vol. 3, pp. 181-190.
- Leong, E.C., Anand, S., Cheong, H.K., and Lim, C.H. (2007) "Re-examination of peak stress and scaled distance due to ground shock" International Journal of Impact Engineering, Vol. 34, No. 9, pp. 1487-1499.
- Li, Q.M., and Reid, S.R. (2006) "About one-dimensional shock propagation in a cellular material" International Journal of Impact Engineering, Vol. 32, pp. 1989-1906.
- Li, Q.M., MAGKIRIADIS, I., and Harrigan, J.J. (2006) "Compressive strain at the onset of densification of cellular solids" Journal of cellular plastics, Vol. 42, No. 5, pp. 371-392.

Lopatnikov, S.L., Gama, B.A., Haque, M.J., Krauthauser, C., Gillespie, J.W., Guden, M., and Hall, I.W. (2003) “Dynamics of metal foam deformation during Taylor cylinder-Hopkinson bar impact experiment” Composite structures, Vol. 61, pp. 61-71.

Lu G.X., and Yu T.X. (2003) Energy absorption of structures and materials, CRC Press, Boca Raton.

Lu, Y., Wang, Z.Q., and Chong, K. (2005) “A comparative study of buried structure in soil subjected to blast load using 2D and 3D numerical simulation” Soil Dynamics and Earthquake Engineering, Vol. 25, pp. 275-288.

Lu, Y. (2005) “Underground blast induced ground shock and its modeling using artificial neural network” Computers and Geotechnics, Vol. 32, pp. 164-178.

Ma, G.W., Hao, H., and Zhou, Y.X. (2000) “Assessment of structure damage to blasting induced ground motions” Engineering Structures, Vol. 22, pp. 1378-1389.

<sup>a</sup>Ma, G.W., and Ye, Z.Q. (2007) “Analysis of foam claddings for blast alleviation” International Journal of Impact Engineering, Vol. 34, pp. 60-70.

<sup>b</sup>Ma, G.W., and Ye, Z.Q. (2007) “Energy absorption of double-layer foam cladding for blast alleviation” International Journal of Impact Engineering, Vol. 34, pp. 329-347.

Ma, G.W., and Ye, Z.Q., Shao Z.S. (2009) “Modeling loading rate effect on crushing stress of metallic cellular materials” International Journal of Impact Engineering, Vol. 36, pp. 775-782.

Ma, G.W., Zhou, H.Y., Lu, Y., and Chong, K. (2010) “In-structure shock of underground structures: A theoretical approach” Engineering Structures, Vol. 32, pp. 3836-3844.

Morris, J.P., Rubin, M.B., Blair, S.C., Glenn, L.A. and Heuze, F.E. (2004) “Simulations of underground structures subjected to dynamic loading using the distinct element method” Engineering Computations, Vol. 21, No. 2-4, pp. 384-408.

Neuberger, A., Peles, S., and Rittel, D. (2007) "Scaling the response of circular plates subjected to large and close-range spherical explosions. Part I: Air-blast loading" International Journal of Impact Engineering, Vol. 34, pp. 859-873.

Park, S.W., Rhee, J.W., Song, W.K., and Kim, M.K. (2005) "Dynamic behavior of underground structures in multi-layered media" Key Engineering Materials, Vol. 297-300, pp. 78-83.

Ramu, S.A., and Iyengar, K.J. (1976) "Plastic response of orthotropic circular plates under blast loading" International Journal of Solids and Structures, Vol. 12, pp. 125-133.

Rao, S.S. (2007) Vibration of continuous systems, Wiley.

Reid, S.R., and Peng, C. (1997) "Dynamic uniaxial crushing of wood" International Journal of Impact Engineering, Vol. 19, No. 5-6, pp. 531-570.

Ruan, D., Lu, G., Chen, F.L., and Siores, E. (2002) "Compressive behaviour of aluminium foams at low and medium strain rates" Composite Structures, Vol. 57, pp. 331-336.

Shen, J.H., Lu, G.X., Wang, Z.H., and Zhao, L.M. (2010) "Experiments on curved sandwich panels under blast loading" International Journal of Impact Engineering, Vol. 37, pp. 960-970.

Smith, P.D., and Hetherington, J.G. (1994) Blast and ballistic loading of structures, Butterworth-Heinemann, London.

Stamos, A.A. and Beskos, D.E. (1995) "Dynamic analysis of large 3-D underground structure by the BEM" Earthquake Engineering and Structural Dynamics, Vol. 24, pp. 917-934.

Stevens, D.J., and Krauthammer, T. (1988) "A finite difference/ finite element approach to dynamic soil-structure interaction modeling" Computers and Structures, Vol. 29, No. 2, pp. 199-205.



Sun, G.Y., Li, G.Y., Hou, S.J., Zhou, S.W., Li, W, and Li, Q. (2010) “Crashworthiness design for functionally graded foam-filled thin-walled structures” Materials Science and Engineering A, Vol. 527, pp. 1911-1919.

Talesnick, M., Horany, H., Dancygier, A.N. and Karinski, Y.S. (2008) “Measuring soil pressure on a buried model structure for the validation of quantitative frameworks” Journal of Geotechnical and Geoenvironmental Engineering, Vol. 134, No. 6, 855-865.

Tan, P.J., Reid, S.R., Harrigan, J.J., Zou Z., and Li S. (2005) “Dynamic compressive strength properties of aluminium foams. Part I-experimental data and observations” Journal of the Mechanics and Physics of Solids, Vol. 53, pp. 2174-2205.

Tan, P.J., Reid S.R., Harrigan, J.J., Zou Z., and Li, S. (2005) “Dynamic compressive strength properties of aluminium foams. Part II- ‘shock’ theory and comparison with experimental data and numerical models” Journal of the Mechanics and Physics of Solids, Vol. 53, pp. 2206-2230.

Task committee on updating manual 42 of the committee on dynamic effects of the structural division of the American society of civil engineers. (1985) Design of structures to resist nuclear weapons effects.

Teeling-Smith, R.G., and Nurick, G.N. (1991) “The deformation and tearing of thin circular plates subjected to impulsive loads” International Journal of Impact Engineering, Vol. 11, pp. 77-91.

US Army Engineers Waterways Experimental Station (1986) Fundamental of protective design for conventional weapons, TM-5-855-1, Vicksburg.

Vardoulakis, I.G., Beskos, D.E., Leung, K.L., Dasdupta, B., and Stirling, R.L. (1987) “Computation of vibration levels in underground space” International Journal of Rock Mechanics and Mining Sciences and Geomechanics Abstracts, Vol. 24, No. 5, pp. 291-298.

Wang, M.L., and Tan, L.Z. (1995) “Stochastic techniques for analyzing shallow-buried reinforced concrete box-type structures” Soil Dynamics and Earthquake Engineering, Vol. 14, pp. 279-287.

<sup>a</sup>Wang, Z.L., Wang, J.G., Li, Y.C., and Leung, C.F. (2006) “Attenuation effect of artificial cavity on air-blast waves in an intelligent defense layer” Computers and Geotechnics, Vol. 33, pp. 132-141.

<sup>b</sup>Wang, Z.L., Li, Y.C., and Wang, J.G. (2006) “Numerical analysis of attenuation effect of EPS geofoam on stress-waves in civil defense engineering” Geotextiles and Geomembranes, Vol. 24, pp. 265-273.

Wang, Z.L., Konietzky, H., and Shen, R.F. (2010) “Analytical and numerical study of P-wave attenuation in rock shelter layer” Soil Dynamic and Earthquake Engineering, Vol. 30, pp. 1-7.

Wang, Z.Q., Lu, Y., Hao, H., and Chong, K. (2005) “A full coupled numerical analysis approach for buried structures subjected to subsurface blast” Computers and Structures, Vol. 83, pp. 339-356.

Waymire DR, Current shock-isolation system theory and practice for Sandia instrumentation systems at the Nevada test site. Sandia National Laboratories; 1989.

Weidlinger, P., and Hinman, E. (1988) “Analysis of underground protective structures” Journal of Structural Engineering-ASCE, Vol. 114, No. 7, pp. 1658-1673.

Weidlinger, P., and Hinman, E. (1991) “Cavitation in solid medium” Journal of Engineering Mechanics-ASCE, Vol. 117, No. 1, pp. 166-183.

Westin P.S. (1978) “Ground shock from the detonation of buried explosives” Journal of Terramechanics, Vol. 15, No. 2, pp. 69-79.

Wong, F.S., and Weidlinger, P. (1983) “Design of underground protective structures” Journal of Structural Engineering-ASCE, Vol. 109, No. 8, pp. 1972-1979.

Wright, J.P., and Smilowitz. R. (1986) “Uncoupling approximation for the dynamic analysis of structures embedded in hysteretic media” Computers and Structures, Vol. 24, No. 5, pp. 791-798.

Wu, C.Q., and Hao, H. (2005) “Numerical study of characteristics of underground blast induced surface ground motion and their effect on above-ground structures. Part I. Ground motion characteristics” Soil Dynamics and Earthquake Engineering, Vol. 25, pp. 27-38.

Yang, Z. (1997) “Finite element simulation of response of buried shelters to blast loadings” Finite Elements in Analysis and Design, Vol. 24, pp. 113-132.

Yankelevsky, D.Z., Feldgun, V.R., and Karinski, Y.S. (2008) “Underground explosion of a cylindrical charge near a buried wall” International Journal of Impact Engineering, Vol. 35, pp. 905-919.

Ye, Z.Q., and Ma, G.W. (2007) “Effects of Foam Claddings for structure protection against blast loads” Journal of Engineering Mechanics-ASCE, Vol. 133, No. 1, pp. 41-47.

<sup>a</sup>Zeng, H.B., Pattofatto, S., Zhao H., Girard, Y., and Fascio V., (2010) “Perforation of sandwich plates with graded hollow sphere cores under impact loading” International Journal of Impact Engineering, Vol. 37, pp. 1083-1091.

<sup>b</sup>Zeng, H.B., Pattofatto, S., Zhao, H., Girard, Y. and Fascio, V. (2010) “Impact behaviour of hollow sphere agglomerates with density gradient” International Journal of Mechanical Sciences, Vol. 52, pp. 680-688.

Zhu, F., Wang, Z.H., Lu, G.X., and Zhao, L.M. (2009) “Analytical investigation and optimal design of sandwich panels subjected to shock loading” Materials and Design, Vol. 30, pp. 91-100.

Zou, Z., Reid, S.R., Tan, P.J., Li, S., and Harrigan, J.J. (2009) “Dynamic crushing of honeycombs and features of shock fronts” International Journal of Impact Engineering, Vol. 36, pp. 165-176.

Zukas, J.A., Nicholas, T., Swift, H.F., Greszczuk, L.B., and Curran, D.R.. (1982) Impact Dynamics, John Wiley & Sons, New York.

# APPENDIX A: THE RESPONSE DERIVATION OF A STRUCTURAL MEMBER SUBJECTED TO A SOIL-TRANSMITTED BLAST WITH NON-ZERO RISE TIME

## A.1 Introduction

For a typical underground structure subjected to a soil-transmitted blast load induced by a subsurface detonation, the most critical situation is considered: the explosion is in the extended line of the structure's symmetry axis. With the rise time taken into consideration, the blast pressure is a triangular load, schematically shown in Fig. 6.1.

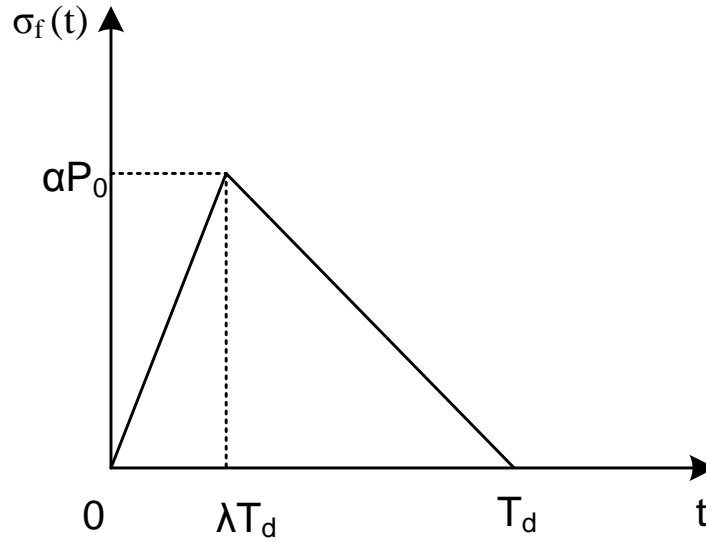


Fig. 6.1 The idealized profile of a soil-transmitted blast

$$\sigma_f(t) = \begin{cases} \frac{P_0 \alpha t}{\lambda T_d} & \text{for } t \leq \lambda T_d \\ \frac{P_0 \alpha (T_d - t)}{(1 - \lambda) T_d} & \text{for } \lambda T_d < t \leq T_d \end{cases} \quad (\text{A.1})$$

where the peak pressure:

$$P_0 = \beta f (\rho_s c_s) \left( \frac{R}{W^{1/3}} \right)^{-r} \quad (\text{A.2})$$

where  $P_0$  is the free-field peak pressure, in psi;  $f$  is a coupling factor of the explosion energy to soil, dimensionless;  $\alpha$  is a reduction factor, defined as ratio of the equivalent uniform pressure on a wall or floor of the structure to the maximum pressure of the actual load distribution;  $\rho_s c_s$  is the acoustic impedance of soil, in psi/fps;  $r$  is an attenuation coefficient, dimensionless;  $W$  is the TNT equivalent charge weight, in lb;  $R$  is the distance measured from the center of explosion to the structure, in ft;  $\beta$  is a factor equal to 160 in the imperial unit system, dimensionless; and  $\lambda$  is a dimensionless number ranging from 0 to 1. It should be noted that the pressure calculated in psi is converted to SI unit system in Pa before being used in the following.

The governing equation for a beam under dynamic load is:

$$EI \frac{\partial^4 w(x,t)}{\partial x^4} + \rho A \frac{\partial^2 w(x,t)}{\partial t^2} = P(x,t) \quad (\text{A.3})$$

Recall the soil-structure interaction, the equation can be re-written as:

$$EI \frac{\partial^4 w(x,t)}{\partial x^4} + \rho A \frac{\partial^2 w(x,t)}{\partial t^2} = 2\sigma(t) - \rho_s c_s \frac{\partial w(x,t)}{\partial t} \quad (\text{A.4})$$

For convenience, the triangular free-field load is divided into two parts, the increasing part and the decreasing part.

## A.2 Phase I: $0 < t < \lambda T_d$

For the duration with linearly increasing load, the governing equation is:

$$EI \frac{\partial^4 w(x,t)}{\partial x^4} + \rho A \frac{\partial^2 w(x,t)}{\partial t^2} + \rho_s c_s \frac{\partial w(x,t)}{\partial t} = 2 \frac{P_0 \alpha}{\lambda T_d} t \quad (\text{A.5})$$

The initial condition is zero displacement and velocity.

Assume the displacement as:

$$w(x,t) = \sum_{n=1}^{\infty} W_n(x) q_n(t) \quad (\text{A.6})$$

$W_n(x)$  is the  $n$ th mode and  $q_n(t)$  is the  $n$ th general coordinate.

The solution is consisted of infinite terms, the displacement corresponding to the  $n$ th mode is:  $w_n(x,t) = W_n(x) q_n(t)$ . The  $n$ th mode natural frequency:

$$\omega_n = \sqrt{\frac{EI}{\rho A}} \left( \frac{n\pi}{l} \right)^2, \quad W_n(x) = \sqrt{\frac{2}{\rho A l}} \sin \frac{n\pi x}{l} \quad (\text{A.7})$$

Combination of Eq. (A.5) and Eq.(A.6) yields:

$$\rho A \sum_{n=1}^{\infty} \omega_n^2 W_n(x) q_n(t) + \rho A \sum_{n=1}^{\infty} W_n(x) \ddot{q}_n(t) + \rho_s c_s \sum_{n=1}^{\infty} W_n(x) \dot{q}_n(t) = 2 \frac{P_0 \alpha}{\lambda T_d} t \quad (\text{A.8})$$

Then the governing equation in the generalized space is:

$$\ddot{q}_n(t) + \frac{\rho_s c_s}{\rho A} \dot{q}_n(t) + \omega_n^2 q_n(t) = 2 \left[ 1 - (-1)^n \right] \frac{l}{n\pi} \sqrt{\frac{2}{\rho A l}} \frac{P_0 \alpha}{\lambda T_d} t \quad (\text{A.9})$$

define

$$\zeta_n = \frac{\frac{\rho_s c_s}{\rho A}}{2\omega_n} \quad (\text{A.10})$$

Eq. (A.9) is re-written as:

$$\ddot{q}_n(t) + 2\zeta_n\omega_n\dot{q}_n(t) + \omega_n^2q_n(t) = 2\left[1 - (-1)^n\right]\frac{l}{n\pi}\sqrt{\frac{2}{\rho Al}}\frac{P_0\alpha}{\lambda T_d}t \quad (\text{A.11})$$

Until now, the governing equation and initial conditions, the structural responses can be determined. The interfacial damping, defined in Eq. (A.10), delineates how the soil interacts with and affects the structural response. Generally, the system consisting of the structural member and the surrounding soil may have three damping ratios, over-damping, under-damping and critical damping, under which the structural responses are as follows:

$$\text{Overly-damping: } \zeta_n = \frac{\frac{\rho_s c_s}{\rho A}}{2\omega_n} > 1$$

The displacement is:

$$w_n(x, t) = \sqrt{\frac{2}{\rho Al}} \sin \frac{n\pi x}{l} \left[ E_n e^{D_{n,2}t} + F_n e^{D_{n,3}t} + \frac{2D_{n,1}}{\omega_n^2 \lambda T_d} \left( t - \frac{2\zeta_n}{\omega_n} \right) \right] \quad (\text{A.12})$$

where

$$E_n = -\frac{D_{n,1}(2\zeta D_{n,3} + \omega_n)}{\omega_n^4 \lambda T_d \sqrt{\zeta_n^2 - 1}}, \quad F_n = \frac{D_{n,1}(2\zeta D_{n,2} + \omega_n)}{\omega_n^4 \lambda T_d \sqrt{\zeta_n^2 - 1}}$$

$$D_{n,1} = \left[1 - (-1)^n\right] \frac{l}{n\pi} \sqrt{\frac{2}{\rho Al}} P_0 \alpha, \quad D_{n,2} = \left(-\zeta_n + \sqrt{\zeta_n^2 - 1}\right) \omega_n, \quad D_{n,3} = \left(-\zeta_n - \sqrt{\zeta_n^2 - 1}\right) \omega_n$$

The velocity and the acceleration are:

$$\dot{w}_n(x, t) = \sqrt{\frac{2}{\rho Al}} \sin \frac{n\pi x}{l} \left( E_n D_{n,2} e^{D_{n,2}t} + F_n D_{n,3} e^{D_{n,3}t} + \frac{2D_{n,1}}{\omega_n^2 \lambda T_d} \right) \quad (\text{A.13})$$



$$\ddot{w}_n(x, t) = \sqrt{\frac{2}{\rho A l}} \sin \frac{n\pi x}{l} \left( E_n D_{n,2}^2 e^{D_{n,2}t} + F_n D_{n,3}^2 e^{D_{n,3}t} \right) \quad (\text{A.14})$$

$$\text{Under-damped: } \zeta_n = \frac{\frac{\rho_s c_s}{\rho A}}{2\omega_n} < 1$$

The displacement time history of the idealized beam is:

$$w_n(x, t) = \sqrt{\frac{2}{\rho A l}} \sin \frac{n\pi x}{l} \left\{ e^{-\zeta_n \omega_n t} \left[ E_n \sin(D_{n,4}t) + F_n \cos(D_{n,4}t) \right] + \frac{2D_{n,1}}{\omega_n^2 \lambda T_d} \left( t - \frac{2\zeta_n}{\omega_n} \right) \right\} \quad (\text{A.15})$$

where

$$E_n = \frac{2(2\zeta_n^2 - 1)D_{n,1}}{\omega_n^2 \lambda T_d D_{n,4}}, \quad F_n = \frac{4\zeta_n D_{n,1}}{\omega_n^3 \lambda T_d}, \quad D_{n,4} = \sqrt{1 - \zeta_n^2} \omega_n$$

The velocity and acceleration are:

$$\dot{w}_n(x, t) = \sqrt{\frac{2}{\rho A l}} \sin \frac{n\pi x}{l} \left\{ e^{-\zeta_n \omega_n t} \left[ -(\zeta_n \omega_n E_n + D_{n,4} F_n) \sin(D_{n,4}t) + (D_{n,4} E_n - \zeta_n \omega_n F_n) \cos(D_{n,4}t) \right] + \frac{2D_{n,1}}{\omega_n^2 \lambda T_d} \right\} \quad (\text{A.16})$$

$$\ddot{w}_n(x, t) = \sqrt{\frac{2}{\rho A l}} \sin \frac{n\pi x}{l} e^{-\zeta_n \omega_n t} \left\{ \left[ \omega_n^2 E_n (2\zeta_n^2 - 1) + 2\omega_n \zeta_n F_n D_{n,4} \right] \sin(D_{n,4}t) + \left[ -2\omega_n \zeta_n D_{n,4} E_n + \omega_n^2 F_n (2\zeta_n^2 - 1) \right] \cos(D_{n,4}t) \right\} \quad (\text{A.17})$$

The total displacement, velocity, and acceleration of the structural element should be the summation of contributions from different modes, i.e.,

$$w(x, t) = \sum_{n=1}^{\infty} W_n(x) q_n(t) \quad (\text{A.18a})$$

$$\dot{w}(x, t) = \sum_{n=1}^{\infty} W_n(x) \dot{q}_n(t) \quad (\text{A.18b})$$

$$\ddot{w}(x, t) = \sum_{n=1}^{\infty} W_n(x) \ddot{q}_n(t) \quad (\text{A.18c})$$

### A.3 Phase II: $\lambda T_d < t < T_d$

In fact, the initial condition of this phase is the terminal condition of the first phase. For convenience, offset the time axis by  $\lambda T_d$  with the new time axis  $t_1 = t - \lambda T_d$ .

The load time history in the new time axis is:

$$\sigma_f(t_1) = P_0 \alpha \left[ 1 - \frac{t_1}{(1-\lambda)T_d} \right] \quad (\text{A.19})$$

The governing equation is:

$$EI \frac{\partial^4 w(x, t_1)}{\partial x^4} + \rho A \frac{\partial^2 w(x, t_1)}{\partial t_1^2} + \rho_s c_s \frac{\partial w(x, t_1)}{\partial t_1} = 2P_0 \alpha \left[ 1 - \frac{t_1}{(1-\lambda)T_d} \right] \quad (\text{A.20})$$

and the initial conditions in this phase:

$$G_n = q_n(t = \lambda T_d), \quad H_n = \dot{q}_n(t = \lambda T_d) \quad (\text{A.21})$$

Introducing the interfacial damping, the governing equation in the generalized space is:

$$\ddot{q}_n(t_1) + 2\zeta_n \omega_n \dot{q}_n(t_1) + \omega_n^2 q_n(t_1) = 2 \left[ 1 - (-1)^n \right] \frac{l}{n\pi} \sqrt{\frac{2}{\rho A l}} P_0 \alpha \left[ 1 - \frac{t_1}{(1-\lambda)T_d} \right] \quad (\text{A.22})$$

Similarly, the responses of the structure member are obtained as follows:

$$\text{Overly-damped: } \zeta_n = \frac{\rho_s c_s}{2\omega_n} > 1$$

The displacement is:

$$w_n(x, t_1) = \sqrt{\frac{2}{\rho A l}} \sin \frac{n\pi x}{l} \left\{ E_n e^{D_{n,2}t_1} + F_n e^{D_{n,3}t_1} + 2 \frac{D_{n,1}}{\omega_n^2} \left[ 1 - \frac{t_1}{(1-\lambda)T_d} + \frac{2\zeta_n}{(1-\lambda)\omega_n T_d} \right] \right\} \quad (\text{A.23})$$

where

$$E_n = \frac{1}{2\omega_n \sqrt{\zeta_n^2 - 1}} \left\{ H_n + \frac{2D_{n,1}}{(1-\lambda)\omega_n^2 T_d} - D_{n,3} \left\{ G_n - 2 \frac{D_{n,1}}{\omega_n^2} \left[ 1 + \frac{2\zeta_n}{(1-\lambda)\omega_n T_d} \right] \right\} \right\}$$

$$F_n = -\frac{1}{2\omega_n \sqrt{\zeta_n^2 - 1}} \left\{ H_n + \frac{2D_{n,1}}{(1-\lambda)\omega_n^2 T_d} - D_{n,2} \left\{ G_n - 2 \frac{D_{n,1}}{\omega_n^2} \left[ 1 + \frac{2\zeta_n}{(1-\lambda)\omega_n T_d} \right] \right\} \right\}$$

The velocity and acceleration are:

$$\dot{w}_n(x, t) = \sqrt{\frac{2}{\rho A l}} \sin \frac{n\pi x}{l} \left[ E_n D_{n,2} e^{D_{n,2}t} + F_n D_{n,3} e^{D_{n,3}t} - \frac{2D_{n,1}}{(1-\lambda)\omega_n^2 T_d} \right] \quad (\text{A.24})$$

$$\ddot{w}_n(x, t) = \sqrt{\frac{2}{\rho A l}} \sin \frac{n\pi x}{l} (E_n D_{n,2}^2 e^{D_{n,2}t} + F_n D_{n,3}^2 e^{D_{n,3}t}) \quad (\text{A.25})$$

Under-damped:  $\zeta_n = \frac{\frac{\rho_s c_s}{2\omega_n}}{\frac{\rho A}{2\omega_n}} < 1$

the displacement is:

$$w_n(x, t_1) = \sqrt{\frac{2}{\rho A l}} \sin \frac{n\pi x}{l} \left\{ e^{-\zeta_n \omega_n t_1} \left[ E_n \sin(D_{n,4} t_1) + F_n \cos(D_{n,4} t_1) \right] + 2 \frac{D_{n,1}}{\omega_n^2} \left[ 1 - \frac{t_1}{(1-\lambda) T_d} + \frac{2\zeta_n}{(1-\lambda) \omega_n T_d} \right] \right\} \quad (\text{A.26})$$

where

$$E_n = \frac{1}{D_{n,4}} \left\{ H_n + \zeta_n \omega_n \left[ G_n - 2 \frac{D_{1,n}}{\omega_n^2} \left( 1 + \frac{2\zeta_n}{(1-\lambda) \omega_n T_d} \right) \right] + 2 \frac{D_{n,1}}{(1-\lambda) \omega_n^2 T_d} \right\}$$

$$F_n = G_n - 2 \frac{D_{1,n}}{\omega_n^2} \left[ 1 + \frac{2\zeta_n}{(1-\lambda) \omega_n T_d} \right]$$

And the velocity and acceleration are:

$$\dot{w}_n(x, t) = \sqrt{\frac{2}{\rho A l}} \sin \frac{n\pi x}{l} \left\{ e^{-\zeta_n \omega_n t} \left[ -(\zeta_n \omega_n E_n + D_{n,4} F_n) \sin(D_{n,4} t) + (D_{n,4} E_n - \zeta_n \omega_n F_n) \cos(D_{n,4} t) \right] - 2 \frac{D_{n,1}}{(1-\lambda) \omega_n^2 T_d} \right\} \quad (\text{A.27})$$

$$\ddot{w}_n(x, t) = \sqrt{\frac{2}{\rho A l}} \sin \frac{n\pi x}{l} e^{-\zeta_n \omega_n t} \left\{ \left[ \omega_n^2 E_n (2\zeta_n^2 - 1) + 2\omega_n \zeta_n F_n D_{n,4} \right] \sin(D_{n,4} t) + \left[ -2\omega_n \zeta_n D_{n,4} E_n + \omega_n^2 F_n (2\zeta_n^2 - 1) \right] \cos(D_{n,4} t) \right\} \quad (\text{A.28})$$

The total displacement, velocity and acceleration of the structural member in the phase:

$$w(x, t_1) = \sum_{n=1}^{\infty} W_n(x) q_n(t_1) \quad (\text{A.29a})$$

$$\dot{w}(x, t_1) = \sum_{n=1}^{\infty} W_n(x) \dot{q}_n(t_1) \quad (\text{A.29b})$$

$$\ddot{w}(x, t_1) = \sum_{n=1}^{\infty} W_n(x) \ddot{q}_n(t_1) \quad (\text{A.29c})$$

Until now, the structural responses within the blast duration are fully explicitly derived. Typically, the acceleration time history which mainly contributes to the in-structure shock is always less than the blast time duration (Ma et al. 2010).

## APPENDIX B: PUBLICATIONS

### Journal papers

Ma, G.W., Zhou, H.Y., Lu, Y., and Chong, K. (2010) “In-structure shock of underground structures: A theoretical approach.” Engineering Structures, Vol. 32, pp. 3836-3844.

Ma, G.W., Zhou, H.Y., and Chong, K. (2011) “In-structure shock assessment of underground structures with consideration of rigid body motion.” Journal of Engineering Mechanics-ASCE, Vol. 137, pp. 797-806.

Zhou, H.Y., and Ma, G.W. (2012) “Double-layer floor to mitigate in-structure shock of underground structures: a conceptual design.” Engineering Structures, Vol. 35, pp. 314-321.

Zhou, H.Y., and Ma, G.W. (2010) “Stress amplification effect of lung.” Medical Hypotheses, Vol. 74, pp. 37-38.

Li, Q.M., Ye, Z.Q., Ma, G.W., Jones, N., and Zhou, H.Y. (2009) “The influence of elastic shear deformation on the transverse shear failure of a fully clamped beam subjected to idealized blast loading.” International Journal of Mechanical Sciences, Vol. 51, pp. 413-423.

Li, J.D., Ma, G.W., Zhou, H.Y., and Du, X.L. “Energy absorption analysis of density graded aluminum foam.” International Journal of Protective Structures. Vol. 2, pp. 333-350.

Li, J.D., Zhou, H.Y., Ma, G.W. (2011) “Numerical simulation of blast mitigation cladding with gradient foam core.” Applied Mechanics and Materials, Vol. 82, pp. 461-466. (doi: 10.4028/www.scientific.net/AMM.82.461)

Zhou, H.Y., and Ma, G.W., Li, J.D., and Zhao, Z.Y. “Analysis of density gradient metal foam for blast mitigation.” Submitted to Journal of Engineering Mechanics-ASCE and under review for the third time.

Zhou, H.Y., Zhao, Z.Y., and Ma, G.W. “Mitigating ground shocks with cellular solids.” Submitted to Journal of Engineering Mechanics-ASCE and under review for the first time.

Zhou, H.Y., and Ma, G.W. “Effect of the Dynamic Media-Structure Interaction: A Revisit.” Ready for submission.

Zhou, H.Y., and Ma, G.W., Li, J.D., and Zhao, Z.Y. “Metal foam cladding subjected to a localized blast: a theoretical approach.” Ready for submission.

Zhou, H.Y., Beppu, M., Ma, G.W. “In-structure shock of underground structures: practical consideration and experiment validation.” Ready for submission.

## **Proceedings papers**

Ma, G.W., Zhou, H.Y., and Chong, K. (2009) “Shock environment assessment of underground structures subjected to subsurface blast.” Second international workshop on performance, protection and strengthening of structures under extreme loading, Hayama, Japan.

Zhou, H.Y., Ma, G.W., Li, J.D., Zhao, Z.Y. (2011) “Metal foam cladding subjected to a localized blast: a theoretical approach.” 9th international conference on shock & impact loads on structures, Fukuoka, Japan.